ABSTRACT

Title of Document: ON MAPPING ELECTRON CLOUDS WITH FORCE MICROSCOPY

C. Alan Wright,
Doctor of Philosophy, 2012

Directed By: Assistant Professor Santiago D. Solares,
Department of Mechanical Engineering

At its core, this is a story about electrons. Electrons drive the interactions of matter at the nanoscale, so an understanding of electron behavior offers significant insight into the behavior of nanoscale materials.

Atomic force microscopy (AFM) has demonstrated great success as a tool for probing matter at the nanoscale, and recent reports suggest that it may even be capable of mapping electron clouds on atomic surfaces. The most recent of these claims came in 2004, when Hembacher *et al*. [*Science* **305**] observed subatomic features while imaging a graphite surface with a tungsten tip using higher-harmonics frequency modulation AFM (FM-AFM). The authors' interpretation of these features as the footprint of the electron density at the tungsten tip's apex atom has been met with much skepticism. But despite the potential significance of the results, a detailed theoretical study has not been performed.

In this work, a computational method based in density functional theory (DFT) is developed in order to simulate the imaging process and draw fundamental conclusions regarding the feasibility of subatomic imaging with higher harmonics FM-AFM. The application of this method to the tungsten/graphite system reveals that the bonding lobes of increased charge density are in fact present at the tungsten tip's apex atom and that the corresponding higher harmonics images can exhibit subatomic features similar to those observed experimentally.

We further show that the filtering process used to experimentally measure the harmonics does not introduce imaging artifacts but that harmonics averaging is not an appropriate method for enhancing contrast. We then suggest an alternate approach: the individual mapping of the first two harmonics, which are expected to dominate the contrast under the experimental conditions studied.

Finally, we demonstrate the important role played by the surface atom used to probe the AFM tip. We find that a small, non-reactive atom is necessary for resolving subatomic features. Most importantly, we show that the observed features are *not a direct reflection* of the electron density at the AFM tip's front atom. Instead, they represent a measure of the bonding stiffness between the tip's front atom and the atoms in the layer above.

On Mapping Electron Clouds with Force Microscopy

By

C. Alan Wright

Dissertation submitted to the Faculty of the Graduate School of the
University of Maryland, College Park, in partial fulfillment
of the requirements for the degree of
Doctor of Philosophy
2012

Advisory Committee:
Assistant Professor Santiago Solares, Chair/Advisor
Distinguished Professor Millard Alexander
Professor Amr Baz
Assistant Professor Sarah Bergbreiter
Associate Professor Miao Yu

Acknowledgments

I offer my sincerest thanks to my advisor, Santiago Solares, for his willingness to bring me into his research group and for his constant guidance throughout my graduate studies. His insights into all aspects of this difficult research problem were always welcomed and appreciated. He is a scholar and a gentleman of the highest distinction, and I consider myself lucky to have gotten to work with him.

I would also like to thank my parents, Beverly and David, my sister Dianne, and my brother-in-law Stephen for their constant support through the ups and downs of these past five years (and all years prior). I owe a special debt of gratitude to both my mom and my Aunt Leslie, who, aside from offering moral support, were always willing to proofread my long scientific papers! I'm extremely fortunate to have such a loving family, and my thanks go out to all the rest of them for their unwavering support.

Thanks are due to Millard Alexander, Amr Baz, Sarah Bergbreiter, and Miao Yu for agreeing to serve on my dissertation committee and for taking the time to review this manuscript. I would also like to thank Hugh Bruck and Abhijit Dasgupta for their comments and suggestions early on in my research work, and Bala Balachandran for his advice and support throughout.

I thank all of my past and present group members: Hussein, Gaurav, Lynn, Adam, Jeff, Daniel, Ben, Steve, and Dave for being awesome guys to work with. I owe a special debt of gratitude to Hussein and Gaurav for their constant willingness to drop everything and help me whenever I had a seemingly unsolvable problem.

Thanks to all of my friends for their steadfast support and for keeping my social life alive. I owe special thanks to Nick Boehm, Steve Mayer, Heath Pollock, and Dave Jaffe.

I would also like to thank Amarildo DaMata, Fitz Walker, Lita Brown, Melvin Fields, Dan Wysling, and the rest of the Staff of the Mechanical Engineering Dept. here at the University of Maryland. They are the unsung heroes that keep this department running smoothly.

Finally, I would like to acknowledge the financial support from the US National Science Foundation, award No. CMMI-0841840.

To

Mom, Dad, Di, and G'ma

Supposing is good, but finding out is better.

- Mark Twain

Table of Contents

Acknowledgments ii

Table of Contents vi

List of Figures ix

1. Introduction 1

    1.1. – A Note to the Reader 1

    1.2. – Motivation 3

    1.3. – Background 5

2. Dissertation Objectives 14

3. Literature Review 16

    3.1. – Scanning Tunneling Microscopy (STM) 16

    3.2. – Atomic Force Microscopy (AFM) 20

        3.2.1. Modes of Operation and Relevant Forces 20

        3.2.2. Force Recovery 25

        3.2.3. Higher Harmonics Imaging 31

    3.3. – qPlus Sensors 33

    3.4. – Elliptic Filters 37

    3.5. – Density Functional Theory (DFT) 37

        3.5.1. Overview 38

        3.5.2. Basics of DFT 39

        3.5.3. Electronic Structure of Tungsten 44

        3.5.4. DFT for AFM 45

    3.6. – Importance of Curve Fitting 46

    3.7. – Numerical AFM Simulation 47

4. Simulation Method Development 48
4.1. – SeqQuest Implementation 49
4.2. – Atomistic Models 51
4.3. – Tip Electron Density 53
4.4. – Simulating Higher Harmonics AFM: Initial Results and Challenges 59
4.4.1. The NPTH System 59
4.4.2. A More Fundamental Approach 75
5. Demonstrating the Feasibility of Observing Subatomic Features 77
5.1. – Introduction 77
5.2. – Tip and Surface Models 79
5.3. – Force Curve Calculation 82
5.3.1. Two-Stage Curve Fitting 84
5.3.2. Verifying Force Reconstruction 88
5.4. – Simulated Images 90
5.5. – Conclusions 96
5.6. – Additional Force Reconstructions 97
5.7. – Additional Simulated Images 99
6. The Effects of Signal Processing 105
6.1. – Introduction 105
6.2. – Relevant Experimental Background 110
6.3. – Root-Mean-Square Harmonics Collection 114
6.4. – Simulated Images 118
6.5. – Filtering 125
6.6. – Conclusions 130
7. Identifying the Source of Subatomic Contrast 133

7.1. – Introduction 133
7.2. – Tip-Sample Systems 137
7.3. – Simulation Results and Discussion 142
7.4. – Conclusions 153
8. Conclusions and Outlook 154
8.1. – Intellectual Contributions 154
8.2. – Outlook 156
References 158

List of Figures

Figure 1.1 – Tunneling current in STM vs. tip-sample forces in AFM. 6

Figure 1.2 – The simultaneously recorded tunneling current (left) and higher harmonics (right) images from Hembacher *et al*. (see Figure 2 in Ref. [1]). Each row represents a separate experiment, with gentle tip-surface contacts between each. While the tunneling current images show a single maximum within the diameter of a tungsten atom, the higher harmonics images display multiple maxima within the same diameter. The authors interpret these subatomic features as the footprint of bonding lobes of increased charge density at the foremost tungsten tip atom. 11

Figure 1.3 – Wigner-Seitz cell of BCC tungsten. View parallel to (A) [001] exhibiting four-fold symmetry, (B) [111] exhibiting three-fold symmetry, and (C) [110] exhibiting two-fold symmetry. 12

Figure 3.1 – The 7x7 reconstruction of Si(111) observed by Binnig *et al*. with the STM [43]. 17

Figure 3.2 – A cartoon illustration of the tip-sample interaction in STM. A bias voltage applied between the tip and sample causes a current to flow when the distance between the two is reduced to the range of a nanometer. In one mode of STM operation, the tip follows the contour, z(x,y), in order to keep the tunneling current constant (Figure 2 of Ref. [12]). 18

Figure 3.3 – A harmonic oscillator under the influence of attractive or repulsive forces experiences either an increase or decrease in amplitude (depending on the frequency setpoint), which can be inferred from the translational shift of its resonance curve. Adapted from Ref. [13]. 22

Figure 3.4 – The first atomic resolution image of Si(111)-(7x7) obtained using FM-AFM (Figure 2 from Ref. [16]; the labels A-E are discussed therein). 24

Figure 3.5 – The first seven Chebyshev polynomials of the first kind. 30

Figure 3.6 – Quartz tuning fork in the qPlus configuration. The oscillation symmetry between the prongs is broken with the addition of the large tip mass, but fixing one of the prongs to a substrate keeps the remaining prong's high *Q* factor intact (Figure 11 from Ref. [12]). 34

Figure 3.7 – Schematic of the separate electrodes of a quartz tuning fork which makes simultaneous STM/AFM possible. The electrode on the free prong (blue) is connected to the tip bias voltage. The fixed prong electrode (red) allows piezoelectric detection of the cantilever oscillation [54]. 35

Figure 3.8 – Si(111)-(7x7) reconstruction imaged using a qPlus sensor in UHV. The image was taken with a constant frequency shift of -160 Hz and an 8 Å oscillation amplitude (Figure 2B from Ref. [7])..... 36

Figure 3.9 – Enlarged view of an adatom from Figure 3.8 displaying two crescents within the diameter of a silicon atom, interpreted as lobes of increased electron density. 36

Figure 3.10 – An illustration of the essence of Kohn-Sham DFT (Figure 1 in Ref. [58]).43

Figure 3.11 – Contour plot of the total valence charge density for the W(001) surface as calculated by Posternak *et al*. (Figure 3 from Ref. [38]). Contours are separated by 0.8 electrons per bulk unit cell. 44

Figure 3.12 – Contour plots of tungsten valence charge densities from (a) slab and (b) bulk calculations done by Mattheiss and Hamann (Figure 3 from Ref. [39]). Again, contours are separated by 0.8 electrons per bulk unit cell. 45

Figure 4.1 – The three W(001) tip structures studied in this work. (A) 3L tip, (B) S2 tip, (C) Blunt3L tip..... 51

Figure 4.2 – The surface structures studied in this work. (A) The two carbon-ring naphthalene (NPTH) surface, (B) the nine carbon-ring (9R) surface (the four carbon ring second layer has been excluded from this figure for clarity). The hydrogen (white) and oxygen atoms (red) saturate the bonds of the edge carbon atoms in order to maintain the sp^2 resonance of each surface. 53

Figure 4.3 – The plot of Final Relaxed Energy [Ry] vs. Spin Polarization for the S2 tip. The SP = 0 value produced the minimum final relaxed energy and so was used in subsequent simulations. 54

Figure 4.4 – (A) A single isosurface of the change in electron density, $d\rho$, for the 3L tip alone (left) and (B) 2.50 Å directly above a carbon atom in the NPTH surface model (indicated by a red circle in Figure 4.8). The isovalue shown is $d\rho = 0.17\ e^-/Å^3$. 55

Figure 4.5 – A single isosurface of the change in electron density, $d\rho$, for the S2 tip alone (A) and during an interaction with the NPTH model surface (B). The isovalue in both images is $d\rho = 0.17\ e^-/Å^3$. 56

Figure 4.6 – The same $d\rho = 0.17\ e^-/Å^3$ isosurface for the Blunt3L tip alone (A) and 2.50 Å above the solid red surface grid position of Figure 5.1B. (DFT calculations for the Blunt3L tip above the NPTH surface were not performed.)..... 57

Figure 4.7 – A comparison of the total density (ρ) to the change in density ($d\rho$) after a self-consistent field calculation for the S2 tip. The $\rho = 1.7\ e^-/Å^3$ isosurface of the total density is shown in gray, along with the $d\rho = +0.17\ e^-/Å^3$ isosurface shown in orange... 58

Figure 4.8 – The two carbon-ring NPTH surface used for method development. A 6x6 grid of relaxed energy curves was developed using SeqQuest. The solid red circle corresponds to the tip positions shown in Figures 4.4B, 4.5B, and 4.9. 60

Figure 4.9 – The S2 tip structure (A) 6 Å above the surface (the grid position indicated by the solid red point in Figure 4.8), and (B) 1.25 Å above the same position. 61

Figure 4.10 – Better fits can be achieved by giving $\beta(z)$ a linear or quadratic form in the standard Morse potential (Eqn. 4.1), but doing so may result in force curves with ill-behaved slopes in regions away from the 20 relaxed energy data points (see Figure 4.11). 63

Figure 4.11 – The force curves resulting from the energy curve fits of Figure 4.10, illustrating the potential problems with linear and quadratic Morse potential. 63

Figure 4.12 – An example of relaxed DFT energy data (black dots) for the NPTH-S2 system with the corresponding Morse (dashed red line) and Levine (solid green line) fits. The latter was used in the simulation data presented in this section. 64

Figure 4.13 – Illustration of the vdW radius for the macroscale tip with the atomistic S2 cluster that is simulated with DFT. 65

Figure 4.14 – The frequency of each cantilever oscillation of the continuum simulation is tracked. The fact that the oscillation amplitude is not controlled means that the frequency shift takes time to stabilize in the presence of each force curve. Here the dotted black line is at the 18 kHz fundamental frequency. The dotted red line marks the stabilized effective resonance. The frequency shift is then the difference between the two. 67

Figure 4.15 – Example FFT of a filtered tip trajectory revealing small but measurable higher harmonics. The horizontal dotted green lines indicate the amplitude of each harmonic. The peak corresponding to the second eigenmode at ~113 kHz is also visible. 69

Figure 4.16 – Simulated constant height Δf (top) and V_{hh} (bottom) images for the NPTH system. The distance of closest approach z_c = 1.50 Å and two vdW offset layers are used (i.e., OS = 2). 71

Figure 4.17 – Simulated constant height Δf (top) and V_{hh} (bottom) images for the NPTH system. The distance of closest approach z_c = 1.50 Å and five vdW offset layers are used (i.e., OS = 5). 71

Figure 4.18 – Hembacher experimental V_{hh} image for comparison..... 72

Figure 4.19 – The five-layer offset V_{hh} image of Figure 4.17 (bottom) displayed with the circumference of a tungsten atom (dotted red circle) and carbon atom (white circle). The white cross marks the center of the carbon atom on the surface. 72

Figure 4.20 – The five-layer offset V_{hh} image of Figure 4.17 (bottom) with the circles illustrating atom size shifted to the center of the four maxima..... 73

Figure 4.21 – The effect of the vdW offset (OS) on the tip-sample force curve. As the number of layers between the micro- and macroscopic parts of the tip is increased, the force curve becomes dominated by the short-range component..... 74

Figure 4.22 – The effect of the vdW tip radius on the tip-sample force curve..... 75

Figure 5.1 – The three-layer W(001) tip structure (A) and graphite top layer (B) studied in this work. The model surface of graphite consisted of a 9-carbon-ring top layer edge-terminated with either oxygen or hydrogen depending on which was needed to maintain the sp^2 hybridization of the carbon atoms. This model also contains a 4-carbon-ring second layer that has been excluded in this figure for clarity. The second layer is included in order to reproduce the difference in electronic states between α- and β-surface carbon atoms. The red circles indicate the grid points for which tip-sample force curves were calculated. 80

Figure 5.2 – (A) A single isosurface (isovalue = +0.2 $e^-/Å^3$) of the change in electron density for the model tip structure used. The view is at an angle from below. The apex atom is indicated by a red square. Four lobes of increased charge density are visible. (B) Comparison of the total density (ρ) to the change in density ($d\rho$) after a self-consistent field calculation for the tip. The ρ = 2.0 $e^-/Å^3$ isosurface of the total density is shown in gray, along with the $d\rho$ = +0.2 $e^-/Å^3$ isosurface shown in orange. 81

Figure 5.3 – (A) Side view of the change in electron density ($d\rho$) for the model tip structure, indicating the location of horizontal cross sections taken directly below the topmost tip layer (B) and directly below the apex atom (C). Horizontal cross section B reveals four bonding lobes below the top layer's center atom and horizontal cross section C reveals four smaller lobes below the apex tip atom, with all isovalues of $d\rho$ included. 82

Figure 5.4 – The ability of the tip and surface atoms to relax meant that attractive and repulsive interactions caused large deformations in the surface geometry. From left to right, the tip is 6 Å, 3 Å, and 1 Å above the solid red surface grid position of Figure 5.1B. 84

Figure 5.5 – Final Relaxed Energy (FRE) DFT data for the tip-sample interaction (over the solid grid point of Figure 5.1B) illustrating the poor fits of both the Morse and Levine potentials. All of the energy curves exhibited a similar broadening of the interaction potential well with respect to these standard fits, necessitating a different curve fitting strategy..... 85

Figure 5.6 – The FRE data of Figure 5.5 fit to a 9^{th} order polynomial..... 86

Figure 5.7 – A larger-range view of Figure 5.6 demonstrating the shortcoming of a 9^{th}-order polynomial fit for developing a tip-sample force curve. 86

Figure 5.8 – Tip-sample force curve analytically calculated from the Poly9 curve fit. The blue points indicate the force data points that are subsequently used to fit to a Levine-based force function. 87

Figure 5.9 – A force function based on the Levine potential was used to fit the interaction well of the Poly9 tip-sample force. 88

Figure 5.10 – (A) Example Final Relaxed Energy (FRE) [aJ] versus distance curve. Such curves were collected on all locations (red circles) shown in Figure 5.1B. Each point on the graph is the result of a separate simulation. (B) Example force curve developed through DFT and curve fitting (red trace) and the reconstruction of the force curve using 6 harmonics in Dürig's equations (blue dotted trace). These curves correspond to the location marked with the solid red circle in Figure 5.1B (directly above one of the carbon atoms)..... 89

Figure 5.11 – Simulated frequency shift (A) and higher harmonics, V_{hh} (B), images calculated using Dürig's equations. The grid of Figure 5.1B has been repeated multiple times in both the x- and y-directions and then cropped to produce rectangular images. Here the distance of closest approach is 1.88 Å. A red hexagon has been overlaid to indicate the positions of the surface carbon atoms. While the graphite lattice is clearly visible in the frequency shift image, four-fold symmetry features similar to those observed experimentally appear in the simulated higher harmonics image. (C) and (D) show a close-up side-by-side comparison of the experimental (C) and simulated (D) V_{hh} images revealing four-fold symmetry features. 91

Figure 5.12 – Force cross sections taken relative to (A) the frequency shift and (B) the higher harmonics images of Figure 5.11. The force corrugations through the carbon ring centers (C) reveal both hole sites (white cross and dotted line) and bonds (blue cross and dotted line), with the hole sites exhibiting the maximum attractive force. The force cross section through the surface β atoms (D) shows corrugations consistent with the two lobes above each atom..... 94

Figure 5.13 – The force curve used for the reconstruction exercise using Dürig's equations. The base position of the cantilever is 5 Å and the fundamental oscillation is 3 Å..... 98

Figure 5.14 – The amplitudes of the higher harmonics for a cantilever oscillating in the tip-sample forces of Figure 5.13, as calculated by Eqn. 5.2. Recall that a_1 is the fundamental amplitude (not shown), so a_2 is the amplitude of the first harmonic, a_3 the second, and so on. 98

Figure 5.15 – Reconstructing the force curve of Figure 5.13 using (A) 3, (B) 6, and (C) 9 harmonics in the expansion of Eqn. 5.3. The accuracy of the reconstruction is already quite high when 6 harmonics are used. 99

Figure 5.16 – Δf (left) and V_{hh} (right) images as calculated from Dürig's equations for the 9R-S2 system. 101

Figure 5.17 – Δf (left) and V_{hh} (right) images calculated from Dürig's theory for the 9R-Blunt3L system. 103

Figure 5.18 – A side-by-side comparison of the higher harmonics images produced by the S2 tip (A) and the Blunt3L tip (B) at a closest approach distance of 1.88 Å. 104

Figure 6.1 – Simultaneously acquired tunneling current (A) and higher harmonics voltage (B) from the experiment of Hembacher *et al*. (adapted from Figure 1.2). The features of subatomic size in the higher harmonics image (B) were interpreted as the signature of bonding lobes of increased charge density at the apex atom of a [001] oriented tungsten tip. The Wigner-Seitz cell (C) for body-centered cubic W(001) exhibits the same four-fold symmetry observed in the features in (B)..... 106

Figure 6.2 – Density functional theory (DFT) calculations form the initial step in simulating the higher harmonics images of Hembacher *et al*. (A) The top layer of the surface model used to approximate graphite and (B) the three-layer W(001) tip model used in the DFT simulations. A tip-sample approach was performed over each of the circles in (A). The filled green, red, blue, and black circles mark the locations where harmonics amplitude ratios were calculated for the construction of Figure 6.5, as well as the locations of the force curves shown in Figure 6.10. Details of the DFT simulations can be found in Chapters 4 and 5..... 109

Figure 6.3 – Sensitivity [mV/pm] of the qPlus sensor to harmonic n (n=1 corresponds to the fundamental oscillation frequency). The sensitivity drops off and plateaus by approximately the 9th harmonic (n=10). 113

Figure 6.4 – Amplitudes (a_n) and voltages (a_n*S_n) directly above a β atom of the model surface (indicated by a solid blue circle in Figure 6.2)..... 114

Figure 6.5 – Amplitude ratios 1:2, 1:3, and 2:3 of the theoretical harmonics (note that harmonic 1 is the first harmonic above the fundamental, i.e., has frequency $2f_0$) over a surface α atom, β atom, hole site, and bond for the model tip-sample system shown in Figure 6.2 for a closest tip-sample approach distance of 1.90 Å and an oscillation amplitude of 3 Å, demonstrating how the ratios change for different surface sites. 117

Figure 6.6 – Experimental 3rd, 5th, and 8th harmonics of a 4-nm-thick platinum-carbon test structure on a fused silica coverslip. The contrast inversion between individual harmonics means that the contrast in an rms sum image would be greatly diminished. (Adapted from Figure 2 in Ref. [94]). 118

Figure 6.7 – Simulated V_{hh} images for the model system of Figure 6.2 created from the (A) 1st harmonic, (B) 2nd harmonic, (C) 3rd harmonic, (D) 4th harmonic, and (E) rms sum of the 1st – 4th harmonics. The closest tip-sample approach distance is 1.90 Å. The positions of the surface carbon atoms are indicated in each image by a red hexagon. Notice that the contour scaling is different in each image and that the voltage values in the 4th harmonic image have dropped by nearly an order of magnitude relative to the 1st and 2nd harmonic images. Consequently, the features in the rms sum image are dominated by the first two harmonics..... 120

Figure 6.8 – Simulated V_{hh} images created using the (A) 5th, (B) 6th, and (C) 7th harmonics, as well as (D) the rms sum of harmonics 1-7. 121

Figure 6.9 – Cross sections (viewed from above) of the DFT-calculated change in electron density directly below the apex atom of the tungsten tip, demonstrating that the four bonding lobes of increased electron density are affected by the lateral position of the tip relative to the surface. The tip-sample distance for all cases is 2 Å, and the (x, y) position of the apex atom relative to a β carbon atom of the surface is indicated with a red X in the inset of each panel. The X is approximately located at the border of the C atom in all cases. The direction of each of the three carbon-carbon bonds is also shown. 123

Figure 6.10 – Representative tip-sample force curves for the four surface sites indicated in Figure 6.2A. Clearly they do not exhibit ~$1/z^2$ behavior over the range of oscillation, which is indicated by the dashed vertical lines. 124

Figure 6.11 – (Next page) Simulated unfiltered (left column) and filtered (right column) images created using the individual harmonics indicated, demonstrating that filtering has a negligible effect on the qualitative nature of the images. A slight change in the contour scaling occurs due to the gain of the filter. 125

Figure 6.12 – Higher harmonics images for a closest tip-sample approach of 1.90 Å, created from the rms sum of the first four harmonics before (A) and after (B) filtering (these images were simulated using the experimental filter specifications: 8th order elliptic high pass with a 20 kHz cutoff). The qualitative difference between the two is minimal, although the filtered image does eliminate the contrast occurring between each set of four-fold features. (C) Difference image constructed as (A) minus (B). The quantitative differences in (C) are on the order of 5% of the maximum value of V_{hh} in (A) and (B). 128

Figure 6.13 – Magnitude responses of an elliptic high-pass filter of various orders and cutoff frequencies. (B) is a magnified view of the rectangle shown in (A). 130

Figure 7.1 – Three crystallographic orientations of a tungsten tip apex were investigated in the work of this chapter. Shown above are side and bottom-up views of (a) W(110), (b) W(111), and (c) W(001) tip models, exhibiting, 2-, 3-, and 4-fold symmetry, respectively. For each, the bonding symmetry of the front atom is indicated by its orange-highlighted bonding partners in the layer above. 137

Figure 7.2 – For each simulation system, the symmetry of the tip structure was exploited in order to reduce computational cost. Shown here are the grids for the (a) W(110), (b) W(111), and (c) W(001) tips used to produce the simulated images of Figure 7.6. The black circles in each panel indicate the relative size and position of the first two layers of the tungsten tip atoms. 139

Figure 7.3 – The $d\rho = 0.08$ $e^-/Å^3$ isosurface of the change in electron density for the (a) He-W(110), (b) He-W(111), and (c) He-W(001) systems. In each case, the helium atom is directly below the front atom of the tip, with the tip-sample distance z_{ts} = 4.00 Å for the He-W(110) system and z_{ts} = 3.50 Å for both the He-W(111) and He-W(001) systems. (d-

e) Constant height slices through the density corresponding to the systems above. In each density slice, the relative sizes and positions of the first two layers of the tips' tungsten atoms are drawn as black circles (dashed lines across the images). For the W(110) and W(001) tips, increased density (dark red) is seen between the front tip atom and the atoms to which it is bonded. These areas of increased density reveal the two- and four-fold symmetry representative of each tip's crystallographic orientation. For the W(111) tip, the areas of increased density do not reveal the three-fold symmetry that one would expect, although such symmetry does appear in the density decreases between the atoms (dark blue). 144

Figure 7.4 – A bottom-up view of the W(111) tip reveals that there is a three-fold nature to the increased density (0.08 $e^-/Å^3$ isosurface shown), but it does not occur at the forefront of the atom, a result likely attributable to the low planar density of a (111) BCC crystal. 145

Figure 7.5 – All short-range force curves for the five tip-sample systems. The vertical dotted line through each set of curves indicates the tip-sample distance (z_{ts}) that corresponds to the simulated constant-height images of Figure 7.6. This distance is z_{ts} = 3.60 Å for all systems except He-W(110), where images were simulated for z_{ts} = 3.90 Å. Note the larger attractive and repulsive forces exerted by the argon atom relative to the helium systems, as well as the fact that the forces for the H-W(001) system remain attractive over the range studied here, with the maximum attractive force approximately two orders of magnitude higher than the He-W(001) system. 146

Figure 7.6 – Constant height slices through the force (1st row), frequency shift (2nd row), and amplitude of the first harmonic (3rd row) for each tip-sample system, where the height in each case is illustrated by the dotted vertical line in the corresponding panel of Figure 7.5. This distance is z_{ts} = 3.60 Å for all systems except W(110), for which the distance examined is 3.90 Å. For the frequency shift and first harmonics images, z_{ts} refers to the closest approach between the tip and the sample during cantilever oscillation. Note that we have plotted the *amplitude* of the first harmonic, which is a departure from the original method of simulating the higher harmonics images as rms voltage maps. 148

Figure 7.7 – (a) He-W(001) and (b) Ar-W(001) interactions for the same tip-sample distance of 3.50 Å, where the atoms have been plotted as solid vdW spheres in order to compare their relative sizes. Also shown are the corresponding constant-height frequency shift images. For the He-W(001) system, this is the image of Figure 7.6h with the relative size of helium indicated by a dotted white circle. For Ar-W(001), the contour scaling has been reduced to cover a frequency shift range comparable to that of He-W(001), and the relative size of argon indicated by a dotted pink circle. 151

Figure 7.8 – Isosurfaces of both total (ρ; shown in gray) and change-in ($d\rho$; shown in yellow) electron density for both the (a) He-W(001) and (b) H-W(001) systems (isovalue $\rho = d\rho$ = 0.04 $e^-/Å^3$). In each, the "surface" atom is in the same position below the front atom of the tungsten tip at a distance z_{ts} = 3.50 Å. In the case of hydrogen, we see the onset of bond formation, which is apparent in all grid positions in the vicinity of the front

tungsten atom (see Figure 7.9) and is responsible for the spherical symmetry observed in the simulated experimental images. 152

Figure 7.9 – Clear evidence of the onset of bond formation shown in Figure 7.8 is apparent at all simulation grid positions in the vicinity of the front tungsten atom. 153

1. Introduction

1.1. – A Note to the Reader

The effective communication of scientific work is no simple task. All research has an underlying story, but the sheer magnitude of information that a PhD dissertation encompasses can make it easy for the broader context of the work to get lost in the fray. With this in mind, I've attempted to craft a narrative that illustrates how this research problem was approached, the issues that arose, and how those issues influenced the direction of the work over the course of my graduate studies. Additionally, each chapter of this work is essentially self-contained, making a cover-to-cover reading unnecessary for understanding the major research results and how each relates to the scope of the overall problem.

The work in this dissertation is theory-based and was inspired by the 2004 experimental report of *subatomic* features resolved via higher harmonics AFM [1]. These features were explained as maps of a single tungsten atom's electron density. This interpretation was met with a great deal of skepticism, but until now it has not been verified or refuted with theoretical simulation.

Before outlining the objectives of this dissertation in Chapter 2, the remaining sections in this chapter provide a succinct overview of the experiment and the relevant

work that led to it. This information is sufficient for understanding the simulation development and results presented in Chapters 4-7; however, detailed background information (and the details of each element of the experiment) can be found in the Chapter 3 Literature Review.

The inherent complexity of this work unveiled itself gradually: Chapter 4 presents the initial development of the simulation method, the issues that arose, and how those issues shaped the work that followed.

The first of the published results is presented in Chapter 5. In this chapter, the feasibility of imaging subatomic features with higher harmonics AFM is demonstrated; however, no claims are made regarding the physical source of this subatomic contrast. This chapter is an adaptation of our 2011 Nano Letters publication [2].

Chapter 6 contains a detailed look at the effects of the signal processing used by Hembacher *et al*. We discuss both i) filtering the cantilever trajectory signal, and ii) the rms detection of higher harmonics as they pertain to the contrast observed in experimental images. We show that filtering does not generate artifacts in the observed images but that the rms detection of higher harmonics is not an appropriate measurement technique for increased image contrast. Nonetheless, the latter result does not negate the feasibility demonstrated in Chapter 5, because we find that the rms images are dominated by the first and second harmonics such that the same subatomic features are observable in their individual maps. The work in this chapter is an adaptation of our 2012 Applied Physics Letters publication [3].

In Chapter 7, we take the first steps toward identifying the physical source of the subatomic contrast. In other words, we wish to determine if the subatomic features are

truly connected to the electron density of the AFM tip. New simulation systems are presented that allow us to draw fundamental conclusions in this regard. We find that while the subatomic features are not direct maps of the foremost tip atom's electron density, the features do represent the spatial dependence of the bonding stiffness between the tip's front atom and the layer of atoms above. As such, the subatomic features reveal the symmetry that one would expect for each crystallographic orientation of the AFM tip apex. We also find that the size and electronic structure of the atom (or molecule) used to probe the tip have a significant impact on the atom's ability to resolve these symmetry features. At time of writing, this work is being prepared for publication.

Finally, in Chapter 8, the intellectual contributions of this dissertation are discussed, beginning with a summary of the main conclusions and followed by the future outlook for this work.

1.2. – Motivation

It has been nearly three decades since the scanning tunneling microscope (STM) and atomic force microscope (AFM) revolutionized the field of surface science [4, 5]. Each instrument is now capable of routinely resolving individual surface atoms, but as with any microscopy technique, one wishes to push the achievable resolution to its highest possible limit.

The first report of subatomic features in an AFM experiment emerged a decade ago from the group of Franz Giessibl in Germany. The authors performed simultaneous STM/AFM of the Si(111)-(7x7) reconstruction with a tungsten tip attached to a qPlus

sensor [6]. In the constant frequency shift image, each surface adatom displayed a substructure composed of two crescents (shown in Figure 3.9). Because gentle contacts between the tungsten tip and the silicon surface were performed in order to achieve stable STM imaging, the authors interpreted these subatomic features as the signature of two dangling bonds at the apex atom of a silicon cluster picked up by the tip during contact [7]. This interpretation was met with skepticism and remains a subject of debate within the AFM community today. Although it has been supported by subsequent density functional theory (DFT) simulations from two separate groups [8, 9], another group has suggested that the subatomic features may have been feedback artifacts [10], and recent DFT calculations indicate that the features could have been the result of a multi-atom tip termination [11]. Nonetheless, if the interpretation *is* correct, the experimental findings have profound implications for scanning probe microscopy and the insight it can provide for atomic-scale matter interactions.

The next publication claiming the resolution of electron density came from the same group a few years later when, in 2004, Hembacher and coworkers published the results of a simultaneous STM/AFM experiment for a tungsten tip imaging a graphite surface. Again, the tungsten tip was attached to a qPlus sensor, and imaging was done in ultra-high vacuum at 4 K. Remarkably, the image created by the higher harmonics of the cantilever trajectory revealed features within the diameter of a single tungsten atom, which the authors interpreted as bonding lobes of increased charge density at the apex atom of the tip (see Figure 1.2) [1].

Again, the analysis of the subatomic features as the footprint of electron bonding lobes has been met with much doubt within the AFM community. But despite the debate

over the accuracy of the interpretation – as well as the potential significance of the results – an in-depth theoretical feasibility study of the 2004 experiment has yet to be completed. This dissertation aims to fill that gap.

To do so, a computational method based in DFT is developed to simulate the higher harmonics imaging process. Aside from answering the question of feasibility, the method *development* itself has provided much insight into why a theoretical study has not yet been attempted, as well as why the experimental results have not been reproduced in the eight years since their publication.

The details of the 2004 experiment performed by Hembacher *et al*. are crucial to comprehending the scope of the theoretical study herein, but the details themselves must be prefaced with a small amount of background information (which will be expanded upon in the literature review). In the next section, we paint a broad picture of the path leading up to the 2004 experiment of Hembacher *et al*. before presenting its details and the part they play in the simulation development.

1.3. – Background

The steep distance-dependence and short interaction range of tunneling current between probe and sample (see Figure 1.1) make scanning tunneling microscopy ideal for achieving atomic resolution on nanoscale surfaces imaged in vacuum environments [12]. The relative ease of measuring tunneling current also makes it an attractive choice for imaging feedback, but this choice inherently limits the applicability of STM to conductive samples.

Atomic force microscopy is not hindered by this limitation since it is a force-based method, but detection of the relevant forces is not as straightforward as current measurement in STM, and therefore achieving atomic resolution with AFM is not as simple [12]. The force between tip and sample (F_{ts}) in AFM is comprised of multiple components that are generally categorized as either short-range or long-range (see Figure 1.1). In ultra-high vacuum (UHV), the short-range (SR) component is predominantly the chemical bonding force (acting on the range of angstroms) while the long-range (LR) component consists of van der Waals (vdW), electrostatic, and magnetic forces (acting up to ~100 nm) [12-14], with vdW typically the dominant LR contribution. For atomic resolution imaging in AFM, one should ideally isolate the short-range chemical forces, but the different force contributions are not easily separable [12, 13, 15].

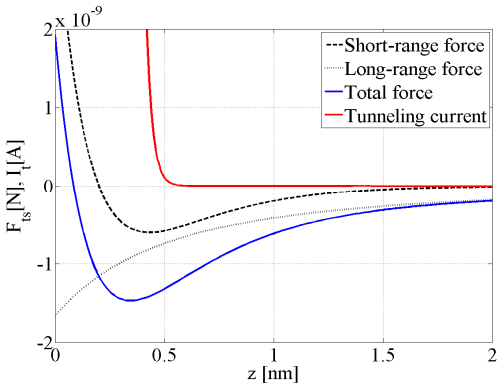

Figure 1.1 – Tunneling current in STM vs. tip-sample forces in AFM.

Nevertheless, the challenge of atomic resolution by AFM in UHV was overcome in 1995 when Giessibl atomically resolved the Si(111)-(7x7) surface reconstruction [16] using the frequency modulation (FM-AFM) detection method [17]. In the FM-AFM mode of imaging (also called noncontact, or nc-AFM), a cantilever is excited with a

sinusoidal driving force such that its oscillation remains at resonance and generally at a fixed amplitude. As the cantilever approaches the sample surface, tip-sample interaction forces alter its effective resonance frequency, and the drive frequency is continuously updated to match this new effective resonance. (This can be achieved through either a phase-locked-loop (PLL) controller [18] or using the self-excitation method [19].) There are two possible choices for topographical mapping in the FM-AFM mode. In constant height FM-AFM, the base position of the cantilever remains fixed during the scan, so the image of the surface is a map of the frequency shift as a function of x and y. Alternatively, one can use the frequency shift as a feedback parameter during the scan. The z-piezo is then moved up and down to maintain a constant frequency setpoint, so that the surface image is a map of the z-piezo position as a function of x and y.

To atomically resolve the Si(111)-(7x7) surface in 1995, Giessibl used the latter approach (known as constant frequency shift FM-AFM) with a cantilever oscillation amplitude of 340 Å. It has since been determined theoretically that much smaller oscillation amplitudes are optimal for FM-AFM imaging [20], which in turn requires stiffer cantilevers to avoid jump-to-contact [21]. To this end, quartz tuning forks (stiffness, k ~ 1-3 kN/m) have been implemented in various forms as AFM cantilevers by soldering a probe tip to one of the prongs [6, 22-24]. The mass of the added tip breaks the oscillation symmetry of the tuning fork prongs which can drastically lower the tuning fork's Q factor. However, in the qPlus configuration one of the prongs is fixed to a substrate such that a single quartz "cantilever" remains, with its high Q factor intact [24].

Regardless of the type of cantilever used, neither FM-AFM mode measures F_{ts} directly but instead does so *indirectly* through the cantilever's frequency shift (or z-

position at constant frequency shift). To recover quantitative values for F_{ts}, an inversion must be applied *post hoc* [25-29]. Because this additional step is not ideal from an experimentalist's standpoint, various methods have been proposed to recover F_{ts} in real time [29-32]. One such method, pioneered by Urs Dürig, is critical to the current investigation.

In 2000, using a first-order perturbative approach, Dürig demonstrated that for cantilever oscillations on the order of the short-range interaction, F_{ts} can be reconstructed by tracking the amplitudes and phases of the higher harmonics of the tip trajectory [32]. This relationship is given as

$$a_n = \frac{2}{\pi k}\frac{1}{1-n^2}\int_{-1}^{1} F_{ts}\left(z_0 + a_1 u\right)\frac{T_n(u)}{\sqrt{1-u^2}}\,du \tag{1.1}$$

for $n \neq 1$, where a_n is the amplitude of the n^{th} harmonic, k is the cantilever stiffness, and $T_n(u)$ is the n^{th} Chebychev polynomial of the first kind [32, 33]. By integrating Eqn. 1.1 by parts n times Hembacher, Giessibl, and Mannhart showed that

$$a_n = \frac{2}{\pi k}\frac{1}{1-n^2}\frac{A^n}{1\cdot 3\cdot 5\cdot \ldots \cdot (2n-1)}\times\int_{-1}^{1}\frac{d^n F_{ts}\left(z_0 + a_1 u\right)}{dz^n}\left(1-u^2\right)^{n-1/2}du \tag{1.2}$$

demonstrating that a_n correlates to a convolution of $d^n/dz^n\left[F_{ts}\left(z_0 + a_1 u\right)\right]$ with a bell-shaped weight function $\left(1-u^2\right)^{n-1/2}$ [1, 33].

The authors argue that the advantage of this result lies in the fact that, for attractive forces in noncontact AFM, higher gradients of F_{ts} have a stronger dependence

on tip-sample distance. If one considers a force that varies as $1/z^p$, doubling the distance reduces the force by $1/2^p$, but the n^{th} derivative of the force with respect to z will be $1/2^{p+n}$ times as small [1]. Thus, contributions to the higher force derivatives will come primarily from the front-most tip atom. The coupling of the higher harmonic amplitudes to higher gradients of F_{ts} makes the latter experimentally accessible, and thus implies that mapping the harmonics should provide increased spatial resolution with respect to conventional FM-AFM [1, 33, 34]. (Note that while this is valid for attractive forces, it is not true in general. We revisit this point in Chapter 6.)

In their 2004 experiment, Hembacher *et al*. implemented this higher harmonics technique using simultaneous, constant height STM/FM-AFM to image a graphite surface with a tungsten tip attached to a qPlus sensor, with separate electrodes for measuring tunneling current and cantilever deflection. The deflection signal was sent to a programmable Stanford Research Systems SR650, which is an 8-pole elliptic-type high-pass filter with 0.1 dB of pass-band ripple and 80 dB of stop-band attenuation [35]. A cutoff frequency of 20 kHz was used in order to eliminate the cantilever's fundamental frequency of ~18 kHz. The combined higher harmonics signal is the root-mean-square (rms) voltage output from the filter, given by

$$V_{hh} = \left(\sum_{2}^{\infty} \left(S_n a_n \right)^2 \right)^{1/2} \tag{1.3}$$

where S_n is the sensitivity of the deflection sensor for the n^{th} harmonic [1],

$$S_n \approx \frac{n}{\left(1+0.0767n^2\right)^{1/2}} \text{ x } 0.1 \text{ mV/pm} \tag{1.4}$$

This processing step has been one of the largest points of contention. The justification for collecting the harmonics this way is given in Ref. [33], as well as note 22 in Ref. [1]. The crux of the argument is that (simulated) images produced by *individual* higher harmonics are similar; therefore, collecting an rms of *all* higher harmonics will not change the nature of the image. Further, collecting all harmonics offers ease of implementation and increases the signal-to-noise ratio (see Chapter 6 for further discussion).

In Hembacher *et al.*'s work, imaging was conducted in cryogenic UHV to minimize atomic vibrations, and graphite was chosen as the surface material in order to exploit the small size of carbon as a probe atom (in these experiments, the roles of tip and sample are viewed as reversed, i.e., the sample atoms are imaging the tip; the authors cite the reciprocity principle posited by Chen in ref. [36]).

The simultaneously recorded tunneling current and higher harmonics images are shown in Figure 1.2 (Fig. 2 from Ref. [1]) with each row of images corresponding to a separate experiment (gentle tip-sample contacts were made between each). The tunneling current images (Figure 1.2A, C, and E) for each experiment exhibit a single maximum within the diameter of a tungsten atom (274 pm), while the higher harmonics images (Figure 1.2B, D, and F) show multiple maxima within the same diameter. The authors interpret these subatomic features as the footprint of bonding lobes of increased charge density at the foremost tungsten tip atom. They further note that while both tunneling current and the higher harmonics should exhibit steep distance-dependence, only the most loosely bound electrons will tunnel (i.e., those at the Fermi level, E_F); therefore, the STM

images cannot resolve the spatial variations in the total charge density [1, 37]. In fact, STM can image only one of the two inequivalent carbon atoms that make up the graphite lattice, because only one of the two has a sufficiently high local density of states (LDOS) at E_F [37].

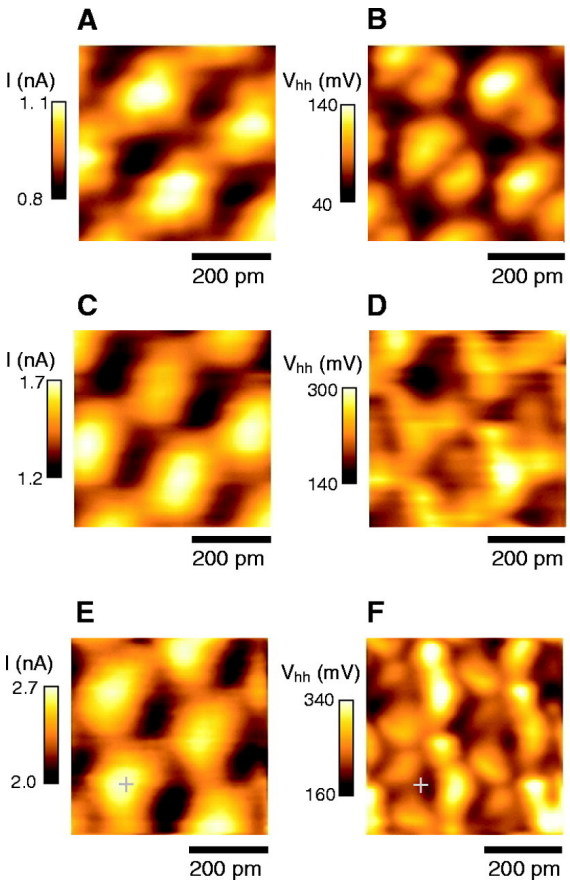

Figure 1.2 – The simultaneously recorded tunneling current (left) and higher harmonics (right) images from Hembacher *et al.* (see Figure 2 in Ref. [1]). Each row represents a separate experiment, with gentle tip-surface contacts between each. While the tunneling current images show a single maximum within the diameter of a tungsten atom, the higher harmonics images display multiple maxima within the same diameter. The authors interpret these subatomic features as the footprint of bonding lobes of increased charge density at the foremost tungsten tip atom.

The different symmetries of the subatomic features found in each experiment (see Figure 1.2B, D, and F) are attributed to the crystallographic orientation of the tungsten atoms at the tip apex. Wigner-Seitz cells of BCC tungsten indicate that two-fold symmetry corresponds to the [110] direction, three-fold to the [111], and four-fold to the [001], as illustrated in Figure 1.3. For the case of [001], the existence of four lobes of increased charge density has previously been demonstrated in *bulk systems* by plane-wave quantum mechanics calculations of the W(001) surface [38, 39]. These lobes are thought to be the result of covalent-like bonding in the bulk, which is a common feature of transition metals with partially occupied d-shells [1, 40].

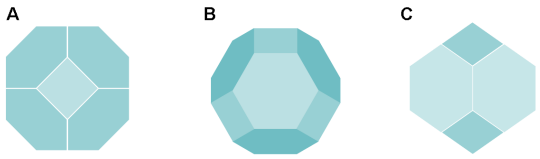

Figure 1.3 – Wigner-Seitz cell of BCC tungsten. View parallel to (A) [001] exhibiting four-fold symmetry, (B) [111] exhibiting three-fold symmetry, and (C) [110] exhibiting two-fold symmetry.

Thus the important features of the 2004 experiment that must be considered in a full theoretical treatment can be summarized as:

1. The crystallographic plane of W responsible for contrast, and the presence of bulk surface states in a non-bulk system such as an AFM tip.
2. The effect of simultaneous STM/AFM on the electronic states of the system.
3. The cantilever dynamics.
4. The sensitivity of qPlus sensors to higher harmonics.

5. The effect of filtering the cantilever trajectory.

In this dissertation, items 2 and 3 are not covered for reasons that will become apparent in Chapter 4. However, they are obvious next steps in the future of this research work.

2. Dissertation Objectives

Broadly speaking, this dissertation will investigate the feasibility of imaging electron density with higher harmonics atomic force microscopy. Originally, the goal was to develop a multi-scale simulation method – ranging from density functional theory (DFT) to continuum dynamics – in order to consider all five of the important features of the 2004 experiment as outlined at the end of the previous chapter. However, as we will see in Chapter 4, the development of such a method uncovered many challenges that made it necessary to take a more fundamental approach first, and then slowly build up to a full theoretical treatment of the problem (which is beyond the scope of the current work).

The objectives for our fundamental approach are as follows:

1. Develop a simulation method based in DFT in order to simulate higher harmonics FM-AFM UHV experiments.
2. Implement the developed method as a means to test the *fundamental* feasibility of subatomic imaging via higher harmonics AFM.
3. Test the effects of signal processing on the qualitative nature of higher harmonics images.

4. Draw fundamental conclusions regarding the physical source of observed subatomic contrast.

The next chapter will present the relevant literature in a manner that builds the foundation of these dissertation objectives in the context of subatomic AFM.

3. Literature Review

3.1. – Scanning Tunneling Microscopy (STM)

The story of subatomic imaging begins in 1982, when Binnig *et al*. demonstrated that electron tunneling could be achieved through a controllable vacuum gap [41]. The theory of electron tunneling had been known since the late 1920's, and the understanding of tunneling through a potential barrier from a surface into vacuum had already been demonstrated [42]. The real breakthrough was the use of piezoelectric materials to achieve mechanical actuation with picometer precision. If one can maintain two metals at a sub-nanometer distance, then a bias voltage between the two metals will cause a measurable current to flow.

This work was the foundation of the scanning tunneling microscope, which Binnig *et al*. introduced the same year [4]. To be successful as a microscope, precise vibration isolation was (and still is) required. But in less than a year, Binnig and coworkers were able to achieve true atomic resolution with the STM by resolving the Si(111)-(7x7) surface reconstruction (see Figure 3.1) [43] – solving one of the most perplexing surface science problems of the time, and completely revolutionizing the field. For this work, Binnig and Rohrer received the Nobel prize [44].

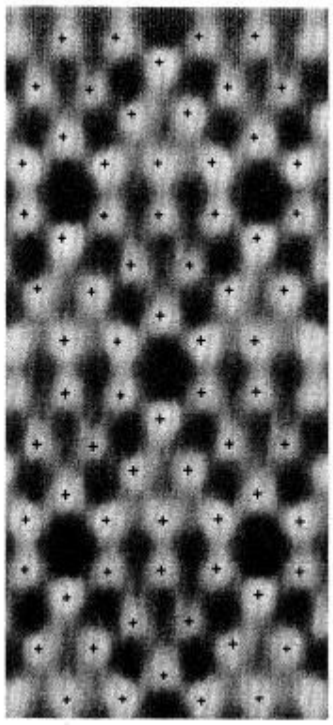

Figure 3.1 – The 7x7 reconstruction of Si(111) observed by Binnig *et al*. with the STM [43].

An understanding of the scanning tunneling microscope is important not only because it was utilized in the Hembacher experiment, but also because it sheds light on the unique challenges faced in AFM. An understanding of STM also reveals its shortcomings, and hence demonstrates the importance of AFM as – at the very least – a supplementary technique.

Scanning tunneling microscopy involves imaging a metal or semiconductor surface with a sharp metal tip, usually made of etched W or Pt/Ir wire (see Figure 3.2). A bias voltage applied between the tip and sample causes a current to flow when the distance between the two is on the order of a nanometer.

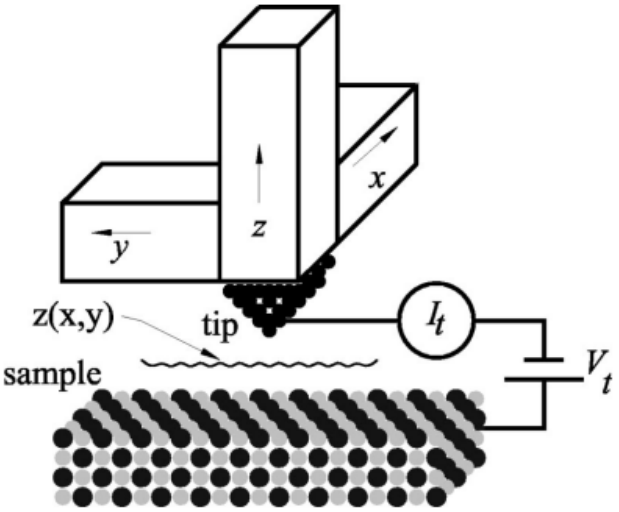

Figure 3.2 – A cartoon illustration of the tip-sample interaction in STM. A bias voltage applied between the tip and sample causes a current to flow when the distance between the two is reduced to the range of a nanometer. In one mode of STM operation, the tip follows the contour, z(x,y), in order to keep the tunneling current constant (Figure 2 of Ref. [12]).

The tunneling current is proportional to the voltage applied as well as the local density of states (LDOS) of the tip-sample system at or above the Fermi level, E_F [45]. This is an important point. The Fermi level is defined as the highest occupied energy level of an electron in a material at 0K, thus electrons at the Fermi level are the most loosely bound and will carry the tunneling current in STM [45].

Tunneling current in STM also has an exponential dependence on the gap distance, given by

$$I(z) \sim e^{-2\alpha z} \tag{3.1}$$

where z is the gap distance and $\alpha = \sqrt{2m\Phi}/\hbar$, with Φ the work function of the tip or sample (depending on the bias voltage), m the mass of an electron, and $\hbar$ the reduced Planck's constant. A typical work function for metals is ~4 eV, meaning α ~ 1 $Å^{-1}$; therefore, when the gap distance z is increased by merely an angstrom, the current drops by an order of magnitude. The consequence is that all of the tunneling current is spatially confined to the apex atom of the tip and its nearest sample atom [12].

A typical plot of tunneling current versus distance was shown in Figure 1.1. Its monotonic nature with tip-sample distance also makes it ideal for use as feedback. In the constant tunneling current mode of operation, the tip-sample distance is increased or decreased as the tunneling current goes up or down, respectively. An alternative mode of operation is to keep the tip-sample distance constant and measure the varying current; both modes produce a topographic map of the sample surface.

Although STM completely transformed the field of surface science, it suffers from a major limitation: both the tip and sample must be electrically conductive. Fortunately, this limitation was overcome with the invention of the atomic force microscope by Binnig *et al.* in 1986 [5]. While the AFM presented the possibility of achieving atomic resolution on insulators (as well as conducting materials), it also brought with it a set of experimental difficulties that would take nearly a decade to overcome.

3.2. – Atomic Force Microscopy (AFM)

3.2.1. Modes of Operation and Relevant Forces

During the initial experiments with the STM, small forces acting on the probe tip were observed [46, 47]. This ultimately led to the invention of the atomic force microscope in 1986 by Binnig, *et al*. [5], in which these forces were utilized for imaging feedback, removing the need for conducting tip-sample systems.

3.2.1.1. Contact Mode (CM-AFM)

The first AFM operated in what is now referred to as contact mode, where the tip probes the sample with small repulsive forces. Here the tip-sample forces (F_{ts}) can be measured directly from the deflection of a cantilever of known stiffness, k, via Hooke's law. This force is then implemented as a feedback signal for imaging by maintaining a set-point cantilever deflection during imaging. Aside from the change in the feedback parameter, the control electronics are essentially the same as STM.

It was initially thought that the AFM could achieve atomic scale resolution as easily as its predecessor. Indeed, early AFM images demonstrated proper lattice periodicity [48, 49], but single atom defects and step edges were not visible, which led to the realization that a cluster of atoms – as opposed to a single atom – must be in contact with the surface [34]. Additionally, the repulsive normal forces between tip and sample could damage the sample if the stiffness of the cantilever probe exceeded the stiffness of

the atom-atom interactions on the surface [50], and the lateral force of the tip dragging along the surface could result in a similar fate.

3.2.1.2. Amplitude Modulation (AM-AFM)

The introduction of the first dynamic AFM mode – amplitude modulation AFM, or AM-AFM – sought to alleviate the problem of sample damage [51]. Also known as "tapping mode" AFM, AM-AFM involves oscillating a cantilever above a sample surface such that it makes only intermittent contact. The oscillation frequency chosen is close to the resonance frequency of the cantilever, and tip-sample forces are measured indirectly through their effects on the cantilever's oscillation amplitude, which is then used as the feedback parameter. More specifically, the gradient of the tip-sample force alters the cantilever's effective resonance,

$$\omega_{eff} = \sqrt{\frac{k}{m} - \nabla F_{ts}} \tag{3.2}$$

where ω_{eff} is the cantilever's effective resonance, k its stiffness, and m its effective mass. The resonance shift results in either an increase or decrease in the oscillation amplitude, which can be seen in Figure 3.3 [13].

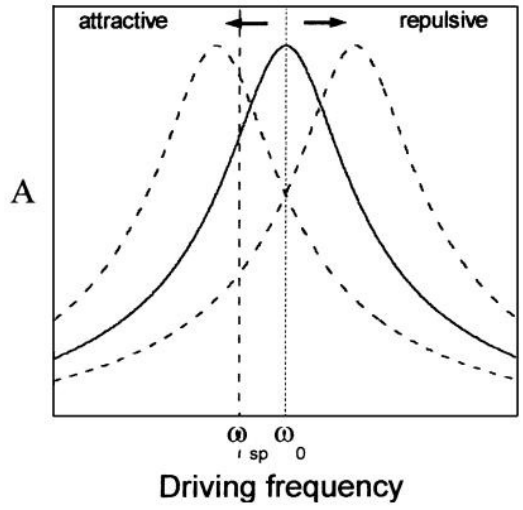

Figure 3.3 – A harmonic oscillator under the influence of attractive or repulsive forces experiences either an increase or decrease in amplitude (depending on the frequency setpoint), which can be inferred from the translational shift of its resonance curve. Adapted from Ref. [13].

While AM-AFM has had great success imaging a broad range of materials in both air and liquid [13], it is not without shortcomings of its own. The nonlinear nature of the tip-sample forces (recall Figure 1.1) results in the existence of two stable oscillation amplitude states, which creates a feedback issue (called "bistability" in the literature) if care is not taken when choosing the setpoint amplitude for a given experiment. Further, as mentioned above, vibrating the cantilever means that the tip-sample forces are no longer being measured directly, but rather through their effect on the cantilever's oscillation. This will be discussed in more detail in Section 3.2.1.3.

Finally, achieving atomic resolution on most surfaces requires an ultra-high vacuum (UHV) environment, which is fundamentally problematic for AM-AFM. The reason lies in the use of amplitude as the feedback parameter. The solution to a damped harmonic oscillator subject to an external force contains a transient term that takes a time

$\tau = 2Q/\omega_0$ in order to be reduced by a factor of $1/e$, where Q is the quality factor of the cantilever. In liquid and air, Q is dominated by environmental damping, and generally falls in the range of ~1 (liquid) to ~100 (air). However, in UHV environmental damping is negligible, and the Q factor is typically on the order of 10^4-10^5 [12, 13]. As a consequence, the feedback response of AM-AFM is too slow to be practical for imaging. The introduction of frequency modulation AFM solves this problem.

3.2.1.3. Frequency Modulation (FM-AFM)

As discussed in the Introduction (Section 1.3), in the FM-AFM mode of imaging [17], a cantilever is excited with a sinusoidal driving force such that its oscillation remains at resonance and (usually) at fixed amplitude. Though this mode is still dynamic, it is generally used in the noncontact regime, where tip deformation and friction effects can be eliminated (for this reason FM-AFM is also called noncontact AFM). As the cantilever approaches the sample surface, tip-sample interaction forces alter its effective resonance frequency (see Eqn. 3.2), and the drive frequency is continuously updated to match this new effective resonance. This can be achieved through using either a phase-locked-loop (PLL) controller [18] or the self-excitation method [19].

There are two possible choices for topographical imaging in the FM-AFM mode. In constant height FM-AFM, the base position of the cantilever remains fixed during the scan, so the image of the surface is a map of the frequency shift as a function of x and y. Alternatively, one can use the frequency shift as the feedback parameter during the scan. The z-piezo is then moved up and down to maintain a constant frequency setpoint so that

the surface image is a map of the z-piezo position as a function of x and y. Giessibl used the latter approach with a cantilever oscillation amplitude of 340 Å to atomically resolve the Si(111)-(7x7) surface in UHV in 1995 [16]. The image he acquired is shown in Figure 3.4.

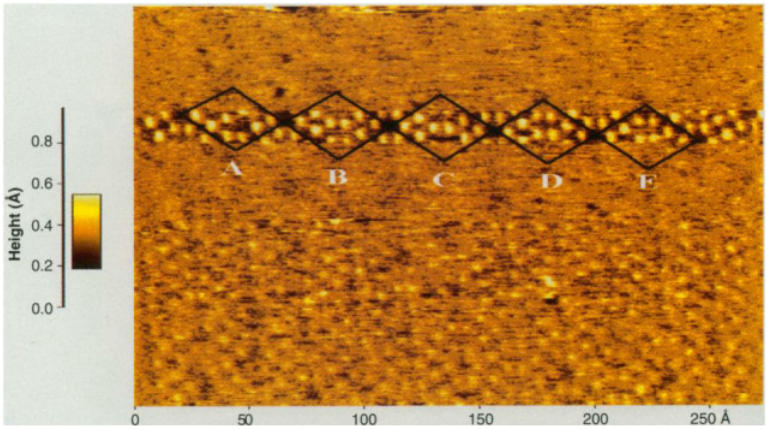

Figure 3.4 – The first atomic resolution image of Si(111)-(7x7) obtained using FM-AFM (Figure 2 from Ref. [16]; the labels A-E are discussed therein).

Regardless of which method is used, the feedback for imaging is much faster because the change in effective resonance frequency occurs within a single oscillation cycle: $\tau \approx 1/f_0$ [12]. Additionally, its being independent of the Q factor makes it suitable for UHV imaging.

Though FM-AFM can be used in UHV, it is still not a direct measure of the tip-sample interaction forces. The short-range (SR) force component in UHV is predominantly the chemical bonding force (acting on the range of angstroms), while the long-range (LR) component consists of van der Waals (vdW), electrostatic, and magnetic forces (acting up to ~100 nm) [12-14], with vdW typically the dominant LR contribution.

For atomic resolution imaging in AFM, one should ideally isolate the short-range chemical forces, but the different force contributions are not easily separable [12, 13, 15]. In the next section, we will explore how the methods of force reconstruction eventually lead to the experimental mapping of higher harmonics of the cantilever oscillation as a means to isolate the SR force contributions.

3.2.2. Force Recovery

Post-hoc methods of force reconstruction from experimentally observed frequency shifts in FM-AFM are largely based on perturbation theory and variational methods [12, 13, 25, 28, 29, 32]. One such method – developed by Dürig in 1999 and 2000 – is of particular interest, as it provides the mathematical foundation for higher harmonics imaging [28, 32].

In ref. [28], Dürig uses variational methods and a Fourier cosine expansion of the cantilever trajectory to relate experimentally measured frequency shifts to tip-sample interaction forces. He builds upon this result in Ref. [32] and shows that the interaction force between an oscillating AFM cantilever and a sample surface can be reconstructed (over the range of oscillation) from the amplitudes and phases of the first few higher harmonics in the cantilever response, as long as the oscillation amplitude is small, i.e., on the order of the interaction range.

For small vibration amplitudes – over which the tip-sample force gradient is approximately constant – the dynamics of the cantilever can be described in terms of a simple harmonic oscillator with effective resonance frequency

$$\omega_{eff} = \omega_0 \sqrt{1 + k_{ts}/k} \,, \tag{3.3}$$

where ω_0 is the free resonance of the cantilever of stiffness k, oscillating in a region of local interaction stiffness k_{ts}. (This equation is equivalent to Eqn. 3.2.) However, in noncontact force microscopy, the interaction stiffness is typically not constant over the range of oscillation (even for small oscillation amplitudes), so no simple relation between frequency shift and interaction force can be established.

For the large amplitude case of variable k_{ts}, Dürig begins with the system's action integral

$$S = \frac{-1}{m} \int_0^T \left[\frac{1}{2} {\omega_0}^2 \psi(t)^2 - \frac{1}{2} \dot{\psi}(t)^2 + \frac{{\omega_0}^2}{k} U_{ts} \left(\psi_0 + \psi(t) \right) \right] dt \tag{3.4}$$

Here $\psi(t)$ is the tip position as a function of time, and $U_{ts}(\psi_0 + \psi(t))$ is the tip-sample interaction potential, where ψ_0 is the base position of the cantilever. According to Hamilton's Principle, the correct tip trajectory $\psi(t)$ will be that for which S is stationary.

$$\partial S = \frac{-1}{m} \int_0^T \left[{\omega_0}^2 \psi(t) + \ddot{\psi}(t) - \frac{{\omega_0}^2}{k} F_{ts} \left(\psi_0 + \psi(t) \right) \right] \partial \psi(t) \; dt \equiv 0 \tag{3.5}$$

where

$$F_{ts} = \frac{-\partial U_{ts}}{\partial \psi(t)} \tag{3.6}$$

Dürig then makes the periodic Ansatz

$$\psi(t) = \sum_{n=1}^{\infty} a_n \cos(n\omega t)\,, \tag{3.7}$$

so that $\{a_n\}$ defines the set of variational parameters. Inserting this into Eqn. 3.5, gives

$$\partial S = \frac{-1}{m}\left[\sum_{n=1}^{\infty} a_n(\omega_0{}^2 - n^2\omega^2)\partial a_n \overbrace{\int_0^T \cos^2(n\omega t)dt}^{=\pi/\omega \text{ for } n \in \text{ integers}} \underbrace{-\frac{\omega_0{}^2}{k}\sum_{n=1}^{\infty}\partial a_n \int_0^T F_{ts}\left(\psi_0 + \sum_{p=1}^{\infty} a_p \cos(p\omega t)\right)\cos(n\omega t)dt}_{\equiv \partial S_{ts}} \right] \tag{3.8}$$

which simplifies to

$$\partial S = \frac{-1}{m}\left[\frac{\pi}{\omega}\sum_{n=1}^{\infty} a_n(\omega_0{}^2 - n^2\omega^2)\partial a_n + \partial S_{ts} \right] \tag{3.9}$$

We know from variational calculus that ∂S must vanish with the variation of each a_n independently. Dürig then proceeds by restricting all $a_n = 0$ for $n \geq 2$, leaving

$$\frac{\partial S}{\partial a_1} = \frac{-1}{m}\left[\frac{\pi}{\omega} a_1(\omega_0{}^2 - \omega^2) - \frac{\omega_0{}^2}{k}\int_0^T F_{ts}\left(\psi_0 + a_1\cos(\omega t)\right)\cos(\omega t)dt \right] = 0 \tag{3.10}$$

or

$$(\omega_0{}^2 - \omega^2) = \frac{\omega\omega_0{}^2}{a_1\pi k}\int_0^T F_{ts}\left(\psi_0 + a_1\cos(\omega t)\right)\cos(\omega t)dt \tag{3.11}$$

Substituting $u = \cos(\omega t)$ and rearranging yields

$$\omega = \omega_0 \sqrt{1 - \frac{1}{k}\frac{2}{a_1 \pi}\int_{-1}^{1} F_{ts}\left(z + a_1(1+u)\right)\frac{u}{\sqrt{1-u^2}}\,du} \tag{3.12}$$

Because for a full cycle $t = 0..T$, the range of the *u* integral would be $u = 1..1$, we instead take a half-cycle and multiply by 2. The replacement $\psi_0 = z_0 + a_1$ has also been made, where z_0 is the distance of closest approach and a_1 is the fundamental oscillation amplitude. Recalling the form of Eqn. 3.3, we obtain effective tip-sample stiffness from Eqn. 3.12 as

$$\boxed{k_{ts}^{\text{eff}} = \frac{-2}{a_1 \pi}\int_{-1}^{1} F_{ts}\left(z_0 + a_1(1+u)\right)\frac{u}{\sqrt{1-u^2}}\,du} \tag{3.13}$$

This equation holds *independently of the oscillation amplitude* [28]. One can easily verify that for a harmonic spring force $F_{ts} = -k_{\text{int}} x$, $k_{ts}^{\text{eff}} = k_{\text{int}}$, because

$$\int_{-1}^{1} \frac{u}{\sqrt{1-u^2}}\,du = 0$$

and

$$\int_{-1}^{1} \frac{(1+u)u}{\sqrt{1-u^2}}\,du = \frac{\pi}{2}$$

Because Eqn. 3.13 is not invertible in closed form, i.e., F_{ts} cannot be calculated from k_{ts}^{eff} (and hence from Δf), Dürig uses a large-amplitude approximation to expand the kernel $-u/\sqrt{1-u^2}$ about $u=-1$ (which is the position of closest tip-sample approach). He then keeps only the leading term in the approximation, which leads to an invertible relation between F_{ts} and k_{ts}^{eff} [28, 32]. However, this approximation is only valid in the large amplitude case and so is not of further interest here. We instead turn our attention to Dürig's work in Ref. [32], where he looks at the variations in S with respect to the higher harmonics a_n.

Beginning from Eqn. 3.8, and lifting the restriction that $a_n=0$ for $n\geq 2$, one obtains the following set of coupled equations for the Fourier coefficients $\{a_n\}$,

$$a_n\left(1+\delta_{n,0}\right)\pi\left(\omega_0^2-n^2\omega^2\right)-\frac{\omega_0^2}{k}\int_0^T F_{ts}\left(z_0+\sum_{j=0}^{\infty}a_j\cos\left(k\omega t\right)\right)\cos\left(n\omega t\right)\omega\,dt=0 \qquad (3.14)$$

Note also that the periodic ansatz for the tip orbital now begins from $j=0$. Dürig then assumes that the tip-sample interaction is weak in the sense that all Fourier coefficients with $n\neq 1$ are small compared to a_1 (this justifies the use of perturbative methods), such that $a_j=0$ for all $j\neq 1$ in the orbital function of the integrand [32],

$$\boxed{a_n=\frac{2}{\left(1+\delta_{n,0}\right)\pi}\frac{\omega_0^2}{k\left(\omega_0^2-n^2\omega^2\right)}\int_{-1}^{1}F_{ts}\left(z_0+a_1u\right)T_n\left(u\right)\frac{du}{\sqrt{1-u^2}}} \qquad (3.15)$$

where $T_n(u) = \cos\left(n \cos^{-1}(u)\right)$ is the n^{th}-order Chebyshev polynomial of the first kind (see Figure 3.5). The substitution $u = \cos(\omega t)$ for the $n = 1$ case leads directly to the Chebyshev polynomials when $n > 1$ via the multiple-angle formula for $\cos(n\omega t)$. Clearly we recover the effective tip-sample stiffness (and hence the frequency shift) of Eqn. 3.13 from Eqn. 3.15 with $n = 1$.

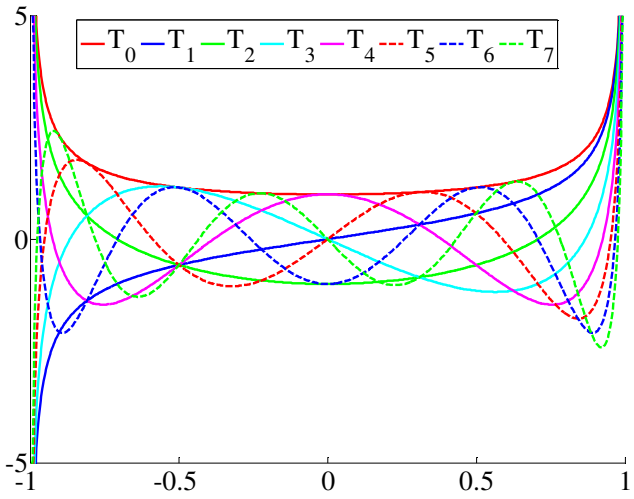

Figure 3.5 – The first seven Chebyshev polynomials of the first kind.

Dürig continues by expressing a *general* tip-sample force in terms of a Chebyshev series

$$F_{ts}\left(z_0 + a_1 u\right) = \sum_{n=0}^{\infty} f_n\left(z_0, a_1\right) T_n\left(u\right) \tag{3.16}$$

with

$$f_n(z_0, a_1) = \frac{2}{(1+\delta_{n,0})\pi} \int_{-1}^{1} F_{ts}(z_0 + a_1 u) T_n(u) \frac{du}{\sqrt{1-u^2}} \tag{3.17}$$

Combining Eqns. 3.15 and 3.17 produces the following relationship between the expansion coefficients, f_n, of the general F_{ts} (Eqn. 3.16) and the Fourier amplitudes, $\{a_n\}$, of the tip orbital

$$\begin{aligned} f_n(z_0, a_1) &= a_n(z_0, a_1) k \left(1 - \frac{n^2 \omega^2}{\omega_0^2}\right) \\ &= a_n(z_0, a_1) \left(k - n^2 \left(k + k_{ts}^{eff}\right)\right) \end{aligned} \tag{3.18}$$

The experimentalist has access to the cantilever stiffness, k, as well as the effective tip-sample stiffness, k_{ts}^{eff}, via the experimental frequency shift. Thus, collecting the Fourier components, i.e., the amplitudes of the higher harmonics, allows one to reconstruct F_{ts} in real time through Eqns. 3.16 and 3.18 as long as the oscillation amplitude is on the order of the tip-sample interaction range [28, 32]. Dürig verifies this result for an example Morse-type force function. The verification of the result for force curves developed with DFT in this work is presented in Section 5.6.

3.2.3. Higher Harmonics Imaging

Giessibl expands on Dürig's work to show that the higher harmonics amplitudes are related to higher gradients of the tip-sample force, which – when attractive in nature – have progressively steeper distance-dependence and therefore should provide higher

spatial resolution (because contributions should come primarily from the front-most tip atom) [1, 33].

Giessibl does this by integrating Eqn. 3.15 by parts n-times and utilizing Rodrigues' formula for $T_n(u)$ [52]:

$$T_n(u) = \frac{(-1)^n 2^n n!}{(2n)!}\left(1-u^2\right)^{1/2} \frac{d^n}{du^n}\left[1-u^2\right]^{n-1/2} \tag{3.19}$$

resulting in

$$\boxed{a_n = \frac{2}{\pi k}\frac{1}{1-n^2}\frac{A^n}{1\cdot 3\cdot 5\cdot \ldots \cdot (2n-1)} \times \int_{-1}^{1} \frac{d^n F_{ts}\left(z_0 + a_1 u\right)}{dz^n}\left(1-u^2\right)^{n-1/2} du} \tag{3.20}$$

and demonstrating that a_n correlates to a convolution of $d^n/dz^n\left[F_{ts}\left(z_0 + a_1 u\right)\right]$ with a bell-shaped weight function $\left(1-u^2\right)^{n-1/2}$ [1, 33].

This result is the basis for the decision of Hembacher *et al*. to collect the higher harmonics of the cantilever oscillation [1], for as long as the cantilever's oscillation amplitude is on the order of the tip-sample interaction distance, the harmonics contain useful information. With regard to using harmonics to characterize a surface, a wonderful analogy to the timbre of musical instruments is given by de Lozanne [53], who observes that the same note played by both a violin and a trumpet sounds different, even though the fundamental frequency played is the same. The difference lies in the harmonic content of the two signals.

While the theoretical usefulness of the higher harmonics is clear, there remains the practical question of whether or not their amplitudes are large enough to be measured. Again, the above derivation is only useful when the oscillation amplitude is on the order of the interaction range (i.e., angstroms), and Giessibl has demonstrated that such small oscillation amplitudes result in the best signal-to-noise ratio [20]. But achieving stable angstrom-scale cantilever oscillation requires extremely stiff cantilevers, and the harmonics of such an oscillation will typically have amplitudes on the picometer scale, which makes them difficult to measure. Fortunately, the use of qPlus sensors offers solutions to both of these problems.

3.3. – qPlus Sensors

Because the restoring force of an oscillating cantilever is given by kA_{osc}, achieving stable oscillation (i.e., avoiding jump-to-contact) with subnanometer amplitudes requires extremely stiff cantilevers [25]. Quartz tuning forks satisfy this requirement, but the addition of a large tip mass to one of the prongs breaks the oscillation symmetry resulting in a ringing mode with low Q [54]. The oscillation symmetry of the prongs is also broken by tip-sample interactions, which alter the effective resonance of only one of them. However, in the qPlus configuration [6, 24, 54] one of the tuning fork prongs is fixed to a substrate, as shown in Figure 3.6.

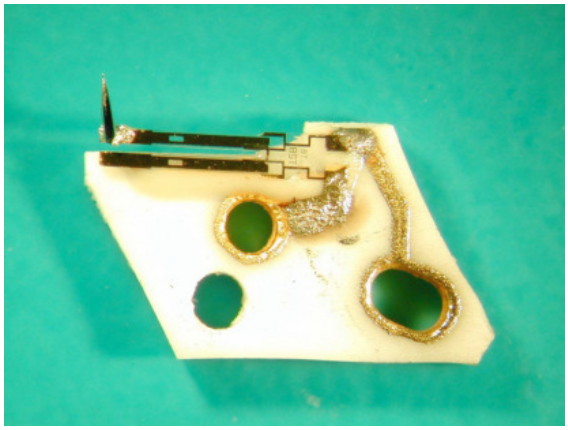

Figure 3.6 – Quartz tuning fork in the qPlus configuration. The oscillation symmetry between the prongs is broken with the addition of the large tip mass, but fixing one of the prongs to a substrate keeps the remaining prong's high *Q* factor intact (Figure 11 from Ref. [12]).

The advantage of fixing one prong is that changes in the eigenfrequency of the remaining quartz "cantilever" due to (conservative) tip-sample interactions do not affect its *Q* factor [6, 54].

The other advantage offered by the qPlus sensor is the most important for the purposes of this discussion: the piezoelectricity of quartz can be utilized for detection of the cantilever oscillation. Traditional silicon cantilevers rely on optical detection of their displacement, and thus require additional hardware for implementation. Optical deflection sensors produce a signal that is proportional to the cantilever deflection. On the other hand, the bending of a quartz tuning fork prong causes a strain, which in turn causes surface charges to accumulate at the corresponding electrode. This charge is proportional to the deflection. When the sensor oscillates, however, a current is generated that is proportional to the deflection multiplied by the frequency of oscillation. As a consequence, higher frequencies (e.g., higher harmonics) generate greater signal strength [33]: this is reflected in the equation for sensitivity (Eqn. 1.4).

Finally, the fact that quartz tuning forks have two separate electrodes (see Figure 3.7) enables simultaneous STM/AFM operation, as it is possible to collect tunneling current *and* cantilever deflection. Referring to Figure 3.7, the electrode on the free prong (blue) is connected to the tip bias voltage. The fixed prong electrode (red) is connected to a current-to-voltage converter for measuring the cantilever deflection [6]. When operated in constant height mode, a direct comparison of simultaneous tunneling current and tip-sample forces can provide added insight to the interaction of materials.

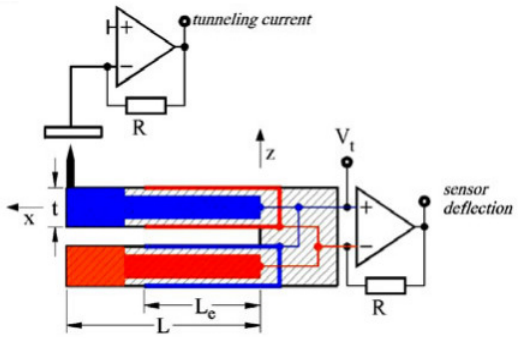

Figure 3.7 – Schematic of the separate electrodes of a quartz tuning fork which makes simultaneous STM/AFM possible. The electrode on the free prong (blue) is connected to the tip bias voltage. The fixed prong electrode (red) allows piezoelectric detection of the cantilever oscillation [54].

The benefits of imaging with small amplitudes using a qPlus sensor in UHV were demonstrated in 2000 for the hallmark Si(111)-(7x7) surface. Figure 3.8 shows the constant frequency shift (Δf = -160 Hz) data obtained by Giessibl *et al*. using an 8 Å oscillation amplitude [7]. The resolution is far superior to the original FM-AFM Si(111)-(7x7) image (see Figure 3.4) obtained with a 340 Å oscillation amplitude. In fact, Figure 3.8 is the basis for the first claim of subatomic resolution as mentioned in Section 1.2. Figure 3.9 is an enlarged view of one of the adatoms from Figure 3.8. The two crescents

that appear within the diameter of a silicon atom are interpreted as lobes on increased electron density [7].

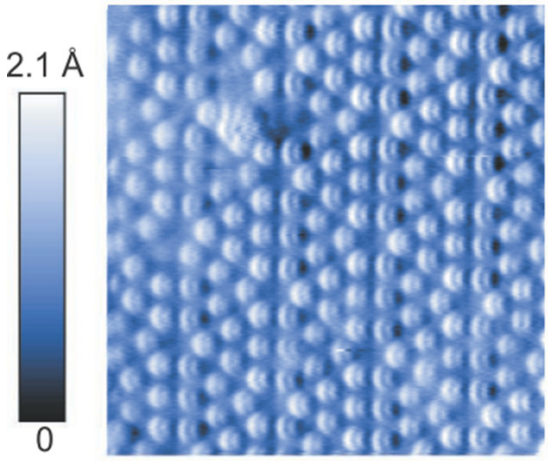

Figure 3.8 – Si(111)-(7x7) reconstruction imaged using a qPlus sensor in UHV. The image was taken with a constant frequency shift of -160 Hz and an 8 Å oscillation amplitude (Figure 2B from Ref. [7]).

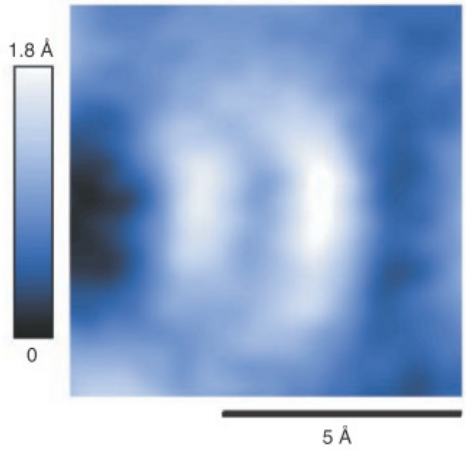

Figure 3.9 – Enlarged view of an adatom from Figure 3.8 displaying two crescents within the diameter of a silicon atom, interpreted as lobes of increased electron density.

3.4. – Elliptic Filters

As mentioned in the Introduction, Hembacher *et al*. filtered out the fundamental frequency of the cantilever as a first step in measuring the higher harmonics amplitudes. For this they use an elliptic-type high-pass filter. The steep cutoff between the pass- and stop-bands is a desirable property of elliptic filters, but this low roll-off causes ripple in both bands. No real filter looks like a step function in its magnitude vs. frequency response, and ripple in the pass-band means that the magnitude of each higher harmonic (particularly those near the "step" corner) is attenuated by a different level. Though the SR650 [35] has only 0.1 dB of pass-band ripple, the picometer scale of the harmonic amplitudes means that even *slight variations* in their measured amplitudes can have a significant effect on the voltage they produce as per Eqn. 1.3. The non-vertical cutoff also means that changes in the cutoff frequency can potentially change the measured amplitude of the harmonics and hence the resultant V_{hh} image. The full effects of filtering for the purposes of higher harmonics imaging are discussed in Chapter 6.

3.5. – Density Functional Theory (DFT)

With the relevant background for the experiment laid out, we now turn our attention to the topics important for simulation development, beginning with DFT.

3.5.1. Overview

The origin of the forces in AFM and the length scales over which they act necessitate the use of quantum mechanics to make theoretical predictions of tip-sample interactions. The (relatively) large number of atoms required for such a theoretical prediction makes density functional theory (DFT) an attractive method for simulating AFM experiments, particularly those in vacuum. Simulated AFM images produced from DFT calculations have been used by many researchers and began to appear in the literature soon after the AFM's invention [55-57].

Today, the most common procedure is to simulate a model AFM tip (usually only a few atoms of the apex are used) above the sample surface in a grid of points. The calculated energies (or forces) at each of these grid points are fit to analytical functions, and those functions are then used to derive the tip-sample force curves necessary to simulate an image. If the DFT forces are used, then of course the analytical function itself becomes the tip-sample force curve.

This approach has been quite successful in qualitatively explaining experimental AFM images, in particular the mechanisms responsible for image contrast. It has also successfully explained what the structure of the tip apex atoms must have been in order to produce a given experimental image. The small scale of the interaction and the inability to know the exact surface and tip structure during a given experiment mean that simulation methods are necessary for interpreting AFM images. DFT simulations for AFM have become more prevalent as computers have become faster, codes more efficient, and exchange-correlation functionals more accurate.

In this section the basics of DFT are outlined, a review of relevant literature regarding DFT for AFM is given, and a discussion of the code used in this work is presented.

3.5.2. Basics of DFT

The interactions of materials on small scales (microns and below) are ultimately determined by the interactions of electrons and nuclei, and the fundamental description of those interactions requires quantum mechanics [58].

All of the properties of a quantum mechanical system are contained within the system's wavefunction, Ψ, which for a system containing N electrons is a function of $3N$ spatial coordinates: $\Psi = \Psi(\vec{r}_1, \vec{r}_2, ..., \vec{r}_N)$. Here, the dependence on electron spin has been excluded. To *determine* the wavefunction, one must solve the Schrödinger equation (SE):

$$\frac{-\hbar^2}{2m}\nabla^2\Psi(\vec{r},t) + V(\vec{r})\Psi(\vec{r},t) = i\hbar\frac{\partial\Psi(\vec{r},t)}{\delta t} \tag{3.21}$$

where $\hbar$ is the reduced Planck's constant, ∇^2 is the Laplacian operator, and $V(\vec{r})$ is the potential energy expression (operator) for the system.

For the case of multiple interacting atoms, the potential energy operator becomes

$$V(\vec{r}_{1,2,...}) = -\sum_{j,l}\frac{Z_l e^2}{\left|\vec{r}_j - \vec{R}_l\right|} + \frac{1}{2}\sum_{j\neq j'}\frac{e^2}{\left|\vec{r}_j - \vec{r}_{j'}\right|} \tag{3.22}$$

where $\vec{r}_j$ are the positions of the electrons and $\vec{R}_l$ and Z_l are the positions and atomic numbers of the nuclei, respectively. This expression reflects the Born-Oppenheimer approximation, which exploits the large difference in the masses of electrons and nuclei [59]. Thus when concerned with the dynamics of electrons, one may consider the nuclei as fixed in space.

Even under the Born-Oppenheimer approximation, the complex nature of the potential energy expression means that the SE is solvable in closed-form for only a few simple systems. When the number of interacting particles exceeds as few as three (e.g., for calculating the energy states of the electrons in a Li atom) we must resort to numerical methods to approximate the solution. Nevertheless, these methods produce excellent agreement with experimentally measured properties and have had great success calculating the energy states of individual atoms and small molecules [58, 60].

One such popular method is Hartree-Fock [59], which approximates the *N*-electron *system* wavefunction using *N* single-electron wavefunctions via the Slater determinant. The problem is that for real systems consisting of multiple interacting *atoms*, the computational requirements of methods such as Hartree-Fock – whose goal is to calculate a multiparticle wavefunction – become astronomically large. Further, in his Nobel lecture, Kohn notes that even if computational power were not an issue, one still could not calculate an accurate approximation of the true wavefunction using traditional wavefunction methods, because the error grows exponentially with the number of interacting particles [60].

The shortcoming of wavefunction methods was not overcome until the mid-1960s with the publication of two papers, the first by Hohenberg and Kohn in 1964 [61] and the

second by Kohn and Sham in 1965 [62]. In the first, Hohenberg and Kohn demonstrated that the *N*-electron wavefunction – with a dependence on 3*N* spatial coordinates – could be reformulated as an equation of the electron density, $\rho(\vec{r})$, a function of only three spatial coordinates [58, 61]. The key to this development was demonstrating that – like the wavefunction – $\rho(\vec{r})$ completely characterizes the system.

In the second paper, Kohn and Sham derived what are referred to as the Kohn-Sham (KS) equations from the Hohenberg-Kohn theorem [62]. The KS equations recast the SE, which describes electrons moving in an external ion potential, into a description of non-interacting electrons moving in an effective potential [63] that produces the same unique, physical electron density. Thus, we are now interested in the density of an *N* particle system, given by

$$\rho(\vec{r}) = \sum_{i}^{N} \left| \varphi_i(\vec{r}) \right|^2 \tag{3.23}$$

where the single-particle Kohn-Sham orbitals, $\varphi_i(\vec{r})$, are solutions to

$$\left(\frac{-\hbar^2}{2m} \nabla^2 + v_{eff}(\vec{r}) \right) \varphi_i(\vec{r}) = \varepsilon_i \varphi_i(\vec{r}) \tag{3.24}$$

where ε_i is the orbital energy corresponding to $\varphi_i(\vec{r})$ and $v_{eff}(\vec{r})$ is the effective potential,

$$v_{eff}(\vec{r}) = v(\vec{r}) + \int \frac{\rho(\vec{r}\,')}{\left| \vec{r} - \vec{r}\,' \right|} dr' + v_{xc}(\vec{r}) \tag{3.25}$$

Here, $v(\vec{r})$ is the physical, external (SE) potential and $v_{xc}(\vec{r})$ is the local exchange-correlation potential,

$$v_{xc}(\vec{r}) \equiv \frac{\delta E_{xc}\left[\rho(\vec{r})\right]}{\delta\rho(\vec{r})} \tag{3.26}$$

where $E_{xc}\left[\rho(\vec{r})\right]$ is the exchange-correlation energy functional. The ground state energy of the system is then calculated as

$$E = \sum_j \varepsilon_j + E_{xc}\left[\rho(\vec{r})\right] - \int v_{xc}(\vec{r})\rho(\vec{r})dr - \frac{1}{2}\int \frac{\rho(\vec{r})\rho(\vec{r}\,')}{\left|\vec{r}-\vec{r}\,'\right|}dr' \tag{3.27}$$

As Kohn noted in his Nobel lecture [60], the *exact* effective single-particle potential $v_{\mathit{eff}}(\vec{r})$ is the unique, fictitious potential which leads to the same physical density of non-interacting electrons as that of the interacting electrons in the physical potential $v(\vec{r})$. In her review, Mattsson provides an instructive illustration of the essence of Kohn-Sham DFT, reprinted in Figure 3.10. Note that the KS wavefunctions and energies, $\varphi_i(\vec{r})$ and ε_i, respectively, have no physically observable meaning, only a connection to the true physical density of the system [60].

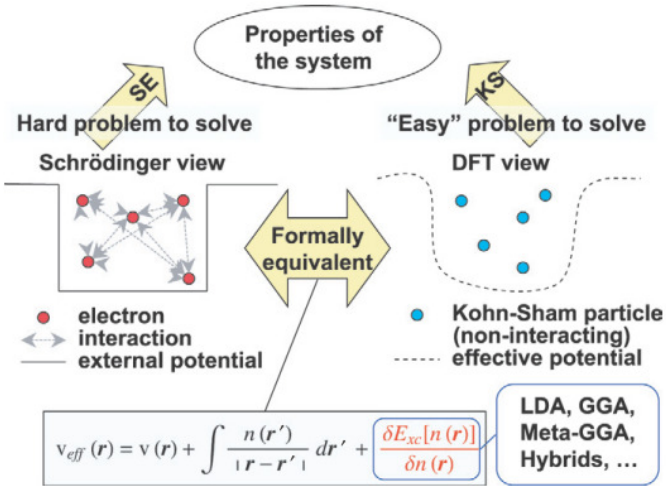

Figure 3.10 – An illustration of the essence of Kohn-Sham DFT (Figure 1 in Ref. [58]).

While the KS equations are mathematically equivalent to the SE, the exact exchange-correlation functional $E_{xc}\left[\rho(\vec{r})\right]$ is not known, so the usefulness of DFT relies entirely on whether an accurate approximation can be found [63]. The simplest approximation that still provides sufficient accuracy is the local density approximation (LDA), which uses only the electron density at a point in space for determining the point's contribution to the total exchange-correlation energy [58]. In this work, we use a slightly more complex (and typically more accurate, though it depends on the system being studied) generalized gradient approximation (GGA), where the gradient of the density at a point in space, $\left|\nabla\rho(\vec{r})\right|$, is also taken into account when calculating the point's contribution to the total exchange-correlation energy. The specific functional we use is that of Perdew, Burke, and Ernzerhof [64], or simply PBE.

3.5.3. Electronic Structure of Tungsten

The extreme usefulness of DFT has made it a commonplace simulation method in many branches of science, such as chemistry, physics, and materials science.

As noted by Hembacher and coworkers [1], in the early 1980s, Posternak *et al.* [38] and Mattheiss and Hamann [39] used DFT in the local density approximation (LDA) to calculate the electronic structure of the W(001) surface. Both papers determined that each tungsten atom has lobes of increased charge density pointed in the direction of its nearest neighbors, as shown in Figure 3.11 (Figure 3 of Ref. [38]) and Figure 3.12 (Figure 3 of Ref. [39]). It is these lobes that Hembacher and coworkers believed were being imaged (refer to Figure 1.2F).

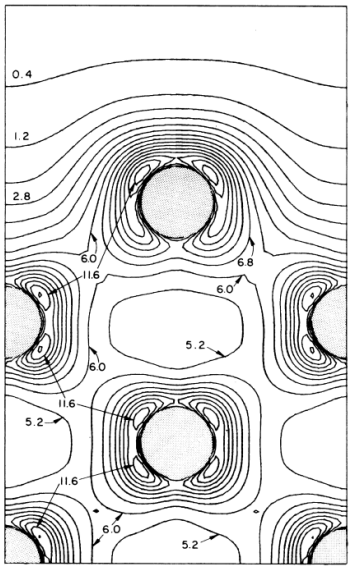

Figure 3.11 – Contour plot of the total valence charge density for the W(001) surface as calculated by Posternak *et al*. (Figure 3 from Ref. [38]). Contours are separated by 0.8 electrons per bulk unit cell.

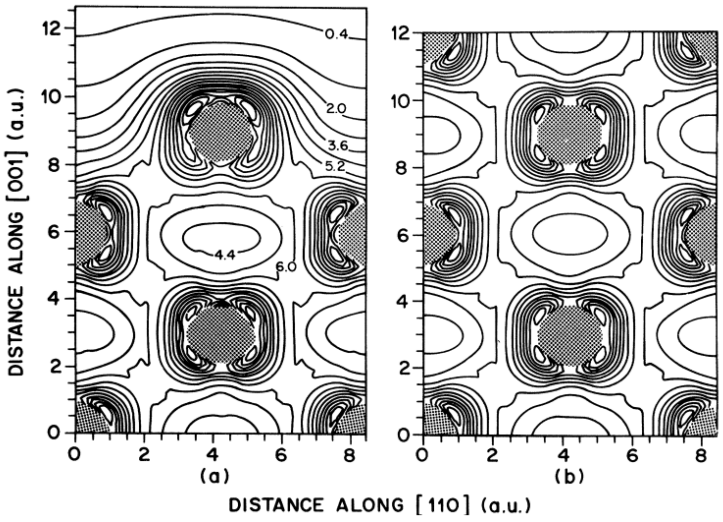

Figure 3.12 – Contour plots of tungsten valence charge densities from (a) slab and (b) bulk calculations done by Mattheiss and Hamann (Figure 3 from Ref. [39]). Again, contours are separated by 0.8 electrons per bulk unit cell.

It is important to note that these calculations were done for bulk systems, so a relevant question arises in the context of AFM: Are similar lobes present in *non-bulk* systems such as AFM tips? As a first step in the method development (see Section 4.3), the electron density of a model W(001) tip will be calculated via GGA DFT.

3.5.4. DFT for AFM

After Giessibl successfully resolved the Si(111)-(7x7) surface reconstruction using FM-AFM [16] in 1995, Pérez and Payne used DFT to study the image formation mechanism [15], attributing the atomic contrast to the interaction between a dangling bond at the tip apex and the dangling bonds localized at the adatoms on the surface. They also found that the saturation of edge electrons on the tip model was essential for

obtaining the desired image contrast, as it created the proper sp^3 hybridization in the tip – resulting in a dangling bond directed toward the surface.

After the first report of subatomic contrast in 2000 [7], Huang *et al*. used DFT to verify that such features are experimentally feasible, though they made no attempt to connect the subatomic features to the lobes of increased electron density at the tip apex atom [8].

Aside from Si(111)-(7x7), Dieška *et al*. have used DFT to study the contrast mechanisms in FM-AFM experiments on metallic surfaces [65, 66], while Caciuc *et al*. have performed DFT studies for imaging InAs(110) [67, 68] and Ag(110) [69, 70]. The structure and stability of silicon tip apexes has also been studied extensively using DFT [71, 72]. However, no attempt has been made to study higher harmonics FM-AFM imaging with DFT methods.

3.6. – Importance of Curve Fitting

As mentioned in Section 3.5.1, DFT produces a point grid of energies or forces. The nature of the curve fit to this DFT data is of utmost importance. First, an ill-fitting function undermines the precision of the DFT simulations, which are at the core of this method. Second, unlike previous DFT studies of AFM experiments, this work is concerned with the higher harmonics in the cantilever trajectory, which couple to the higher gradients of the force. As such, the higher gradients of the curve fit must be continuous and exhibit well-behaved slopes in order to provide accurate calculations of the higher harmonics in the tip motion.

3.7. – Numerical AFM Simulation

To study the effect of the cantilever dynamics and control systems on the imaging process, continuum simulation is necessary. The Verlet algorithm [73, 74] for numerical integration of the cantilever equations of motion has been used with great success in the simulation of AFM experiments (see, for example, [75, 76]). The AFM simulator used for part of this work was written in the C programming language and integrates the first three eigenmodes of the quartz tuning fork, which oscillates in the presence of the DFT-developed force curves. This is discussed in greater detail in Section 4.4.1.3. Ultimately, however, the use of continuum simulation to study the effect of the cantilever dynamics must be revisited in future work.

With the dissertation objectives having been stated and the necessary background information expounded upon, the next chapter presents the simulation method development along with a discussion of the results and challenges that paved the way for the final direction of this work.

4. Simulation Method Development

This chapter provides an overview of the simulation method development – with the initial results and challenges that steered the direction of the work. Because this research is the first to tackle higher harmonics simulation for AFM (and perhaps the only work to deal with tungsten tip models) we tried to make the simulation approach as fundamental as possible and then build upward in complexity. Even with this in mind, we found that it was necessary to backtrack and rework certain aspects of the method in order to lay the foundation on which to build. Our *initial* simulation approach can be summarized as follows:

1. DFT to calculate energy vs. distance curves for a dense grid above the sample surface and to provide us with the electron density of the system
2. Accurate curve fitting of the energy data, followed by differentiation to produce force curves for each (x, y) grid point
3. Correcting these short-range force curves with a long-range van der Waals component
4. Numerical AFM simulation to calculate the trajectory of the oscillating cantilever in the presence of each force curve

5. Filtering the trajectory (incorporating the experimental rms technique) followed by Fourier analysis of each trajectory to calculate the amplitudes of the higher harmonics in the tip-sample interaction

What follows are in-depth discussions of each step as they pertain to the first tip-sample system that we simulated, beginning with the implementation details of the DFT code and how the first tip model was chosen.

4.1. – SeqQuest Implementation

As stated in Section 3.2, the short-range force component is responsible for the highest resolution. The challenge posed to the experimentalist is to extract the short-range component from the many forces acting on the tip [77]. In simulation, however, one can develop the theoretical short-range force curve with quantum mechanics, specifically DFT.

For this the SeqQuest DFT code developed by Peter Schultz at Sandia National Labs [78] was used. The source code was obtained directly from Dr. Schultz, as it is not commercially available. The code itself ships with both serial and parallel utility files, so that it can be compiled to run in either mode. The code was built on both the campus-wide "deepthought" cluster, which runs the Portable Batch System (PBS) for job scheduling, as well as the Mechanical Engineering Department's "aston" cluster, which runs Platform's Load Sharing Facility (LSF). While this may seem like a straightforward task, building the code required a detailed understanding of UNIX systems and bash shell

scripting, and SeqQuest technical support is virtually non-existent. As a result, we were able to build the code only in serial, meaning an executed job runs on a single core. While we were able to compile the code in parallel, successful execution of the mpirun program, which implements the Message Passing Interface (MPI) needed for multithreaded jobs, has not been realized. (Establishing SeqQuest's parallel processing capabilities would be a good first step in the continuation of this project.)

Though SeqQuest is a very robust, accurate DFT code [79], the fact that it is not commercially available also means that there are very few post-processing tools. We were given a primitive code, "QGRIDS," for extracting the electronic density of the system from the binary files generated by the code. Unfortunately, QGRIDS did not work as shipped, but we were able to debug the source code. QGRIDS allows one to generate a txt file of the form

$$[x \qquad y \qquad z \qquad \rho_0 / d\rho / V_{es}]$$

where the fourth column contains either the initial electron density, the change in electron density, or the electrostatic potential of the system. In order to make this volumetric data useful, a C program was written to convert the four-column format into the Gaussian Cube file format, which can be read by the Visual Molecular Dynamics (VMD) software developed at the University of Illinois Urbana-Champaign [80, 81]. In this work, all three-dimensional renderings of electron density were created with VMD.

4.2. – Atomistic Models

To simulate a tungsten tip above a graphite surface, atomistic tip and surface models were built using Accelrys Materials Studio [82]. Our initial focus was the four-fold features attributed to a W(001) tip structure, so the first tip apex models investigated were all oriented in the [001] direction, as shown in Figure 4.1. Figure 4.1A shows a three-layer W(001) tip, hereafter called the 3L tip. The tip model in Figure 4.1B has a "stronger" second layer – eight additional tungsten atoms – and is therefore referred to as the S2 tip. (The motivation for using the S2 tip will be discussed in the next section on tip electron density.) The blunt three-layer tip in Figure 4.1C is simply called the Blunt3L tip. Though tip-sample interactions with the Blunt3L tip were simulated, Hembacher and coworkers note that the tip responsible for subatomic contrast in their experiments is almost certain to have been terminated in a single apex atom because of the nature of the simultaneously acquired STM images [1, 37]. The simulation results for the Blunt3L tip presented in Chapter 5 support this claim. The strong tip-sample interactions caused by the four apex atoms lower the resolution of the simulated images.

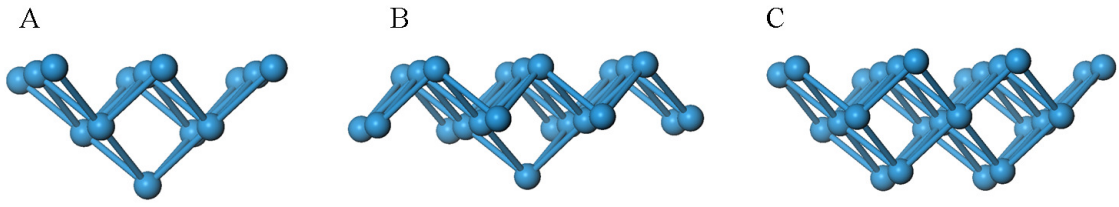

Figure 4.1 – The three W(001) tip structures studied in this work. (A) 3L tip, (B) S2 tip, (C) Blunt3L tip.

The surface models of graphite studied are illustrated in Figure 4.2 The carbon ring surfaces were terminated with either hydrogen or oxygen atoms to saturate free electrons and thus mimic the sp^2 hybridization of the surface carbon atoms. Though these structures maintain full resonance, the two carbon ring surface is likely to be too small to adequately represent graphite. Note that this surface is technically a molecule of naphthalene, which will be abbreviated NPTH. As such, it contains no second layer, which is responsible for the distinction between the α and β atoms of graphite – each α atom of the graphite surface is directly above an α atom in the layer below, while β atoms are above hollow sites. However, the NPTH surface was used purely in the context of method development and thus served merely as a first approximation to reduce computational cost. The NPTH simulations were good for carrying out parametric studies and revealing simulation challenges, but the feasibility of Hembacher *et al.*'s experimental work was gauged by the more realistic nine carbon ring (9R) surface of Figure 4.2B (feasibility is addressed in Chapter 5). The 9R model, aside from being larger, contained a second layer of four carbon rings (also edge terminated with hydrogen and oxygen atoms) that provided the proper distinction between α and β atoms on the surface. The second layer has been excluded from Figure 4.2B for clarity.

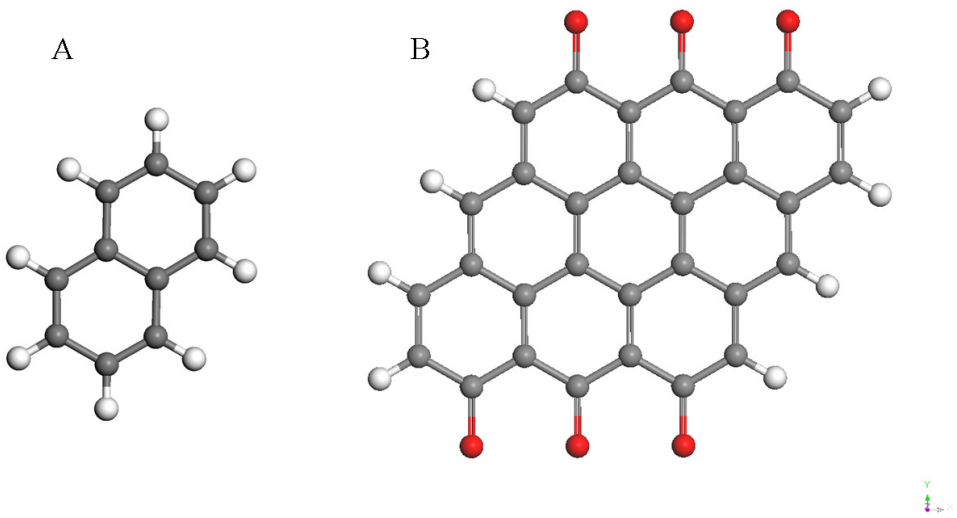

Figure 4.2 – The surface structures studied in this work. (A) The two carbon-ring naphthalene (NPTH) surface, (B) the nine carbon-ring (9R) surface (the four carbon ring second layer has been excluded from this figure for clarity). The hydrogen (white) and oxygen atoms (red) saturate the bonds of the edge carbon atoms in order to maintain the sp^2 resonance of each surface.

4.3. – Tip Electron Density

All DFT simulations used a spin-polarized PBE functional [64], semi-local norm-conserving pseudopotentials [83], and a local-orbital basis of contracted Gaussians in a linear combination of atomic orbitals (LCAO) to solve the KS equations fully self-consistently. The double-zeta plus polarization basis for tungsten that shipped with the code had been refined in a five layer W(001) system [84]. The different tip and surface structures were relaxed independently before being combined as a full system. In the case of the tip structures, the lowest energy spin polarization (excess spin-up electrons) was also determined prior to any surface interaction. In practice, this is done by relaxing the structure for varying spin polarizations and finding the minimum in the plot of relaxed

energy vs. spin polarization [79], an example of which is shown in Figure 4.3 for the S2 tip. In this case, the lowest energy spin polarization is found to be 0 (i.e., no unpaired electrons), which is the value used for the subsequent simulations of the S2 tip-surface interactions.

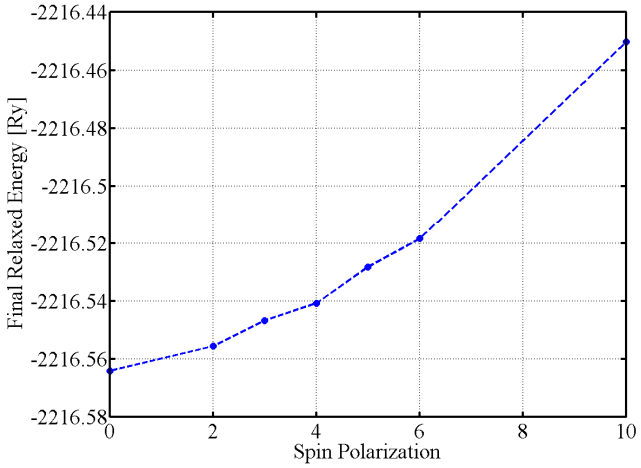

Figure 4.3 – The plot of Final Relaxed Energy [Ry] vs. Spin Polarization for the S2 tip. The SP = 0 value produced the minimum final relaxed energy and so was used in subsequent simulations.

Recalling from Section 3.5.3 that DFT calculations of bulk W(001) reveal four lobes of increased charge density at the surface, the first question this work wished to answer was, "Are similar lobes present in *non-bulk* systems such as AFM tips?"

In DFT, the initial electron density ρ_0 in the tip-sample system is a superposition of the individual atom electron densities. During each self-consistent field (SCF) calculation for the system, the change in electron density $d\rho$ is calculated. The total electron density for the system is then the sum of the initial density and the change. Figure 4.4A shows a single isosurface of the change in electron density ($d\rho$ = 0.17 $e^-/Å^3$) calculated in SeqQuest for the 3L tip alone, which reveals only a single lobe normal to

the apex atom (indicated by a red square). However, the four lobes of increased electron density appear during the interaction between the tip and the NPTH surface, as shown in Figure 4.4B (again indicated by a red square). Here, the apex atom is 2.50 Å directly above the solid red circle of Figure 4.8, which shows the grid above the small model surface.

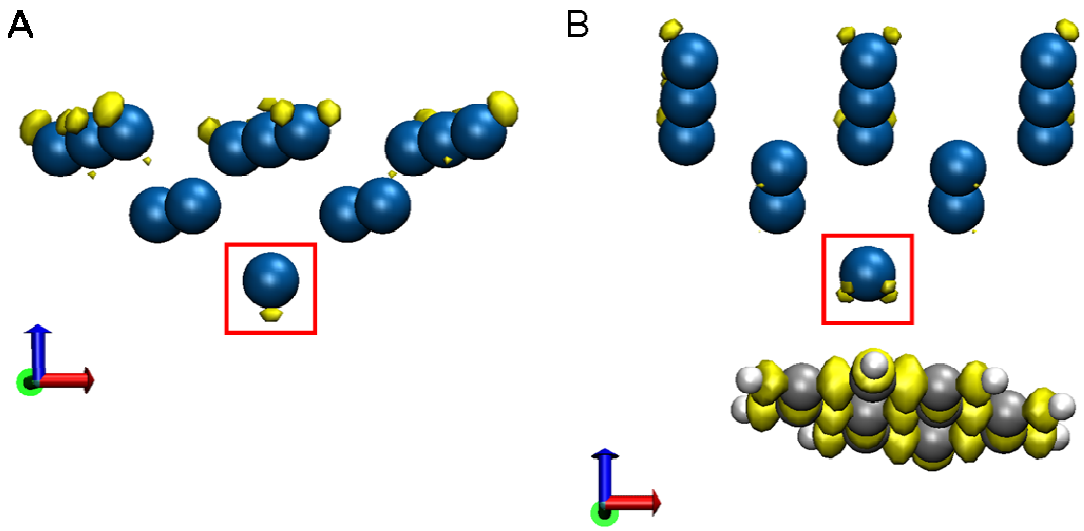

Figure 4.4 – (A) A single isosurface of the change in electron density, $d\rho$, for the 3L tip alone (left) and (B) 2.50 Å directly above a carbon atom in the NPTH surface model (indicated by a red circle in Figure 4.8). The isovalue shown is $d\rho$ = 0.17 $e^-/Å^3$.

Figure 4.5A shows the same $d\rho$ = 0.17 $e^-/ Å^3$ isosurface for the S2 tip alone. Here we see that the four lobes of increased charge density are present at the tip's apex atom even in the absence of a tip-sample interaction. Because quantum mechanics calculations for *bulk* W(001) have suggested that four lobes of increased charge density are present at surface atoms [39, 85], it is reasonable to conclude that the additional second layer atoms increase the bulk-like nature of the tip. Figure 4.5B shows the S2 tip 2.50 Å above the

same solid red circle of Figure 4.8. Because the four lobes are more pronounced for the S2 tip than for the 3L tip, the former was used for all W(001) tip simulations in this work.

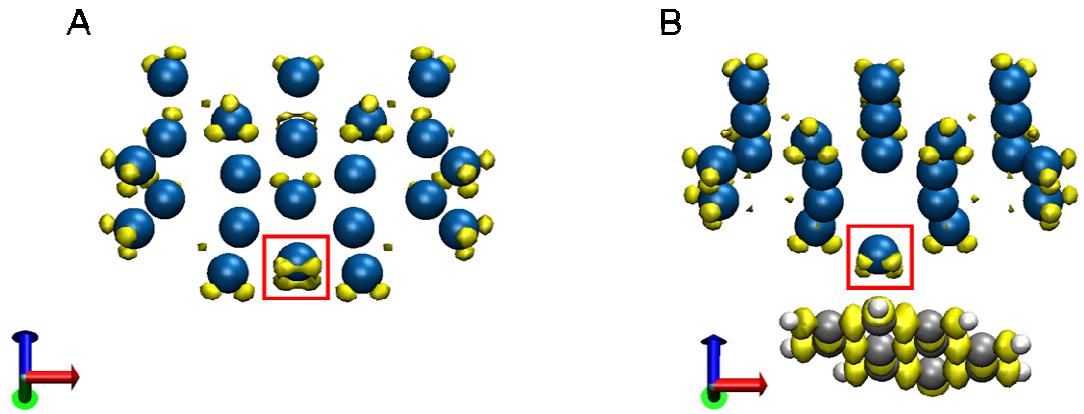

Figure 4.5 – A single isosurface of the change in electron density, $d\rho$, for the S2 tip alone (A) and during an interaction with the NPTH model surface (B). The isovalue in both images is $d\rho$ = 0.17 $e^-/Å^3$.

Because the crystallographic structure of the tip apex is so crucial to the interpretation of the subatomic features in Hembacher's work, the possibility that the four-fold symmetry features were caused by four atoms at the tip apex was not discounted. The idea was not that the four lobes represented the signature of each of these apex atoms, but rather that a single carbon atom may have simultaneously imaged partial densities from each. By analogy, instead of four electron density "arms" of a single apex atom reaching toward a surface carbon atom, one "arm" from each of four apex atoms is reaching toward it. The change in electron density for the isolated Blunt3L tip (see Figure 4.6A) helps to illustrate this. However, subsequent tip-sample simulations with the 9R model (see Figure 4.6B) revealed that these four lobes do not bend toward the surface in

a manner that would result in four features within the diameter of a single tungsten atom. Simulated higher harmonics images using the Blunt3L force curves also suggest that a blunt tip was not responsible for the experimentally observed subatomic features. These results are presented in more detail in Section 5.7.

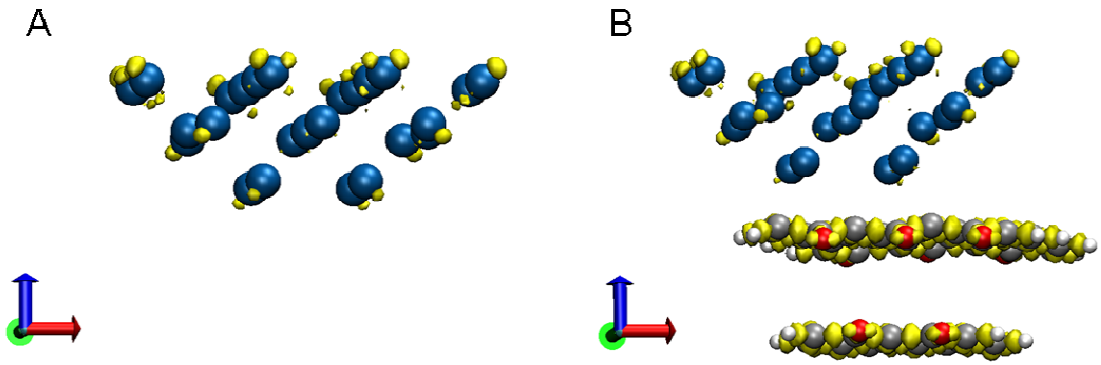

Figure 4.6 – The same $d\rho$ = 0.17 $e^-/Å^3$ isosurface for the Blunt3L tip alone (A) and 2.50 Å above the solid red surface grid position of Figure 5.1B. (DFT calculations for the Blunt3L tip above the NPTH surface were not performed.)

While the presence of the four lobes of increased charge density in non-bulk tip structures is a promising result, it is important to note that the *value* of the density increase is small in comparison to the total electron density in the same region of space. Figure 4.7 shows side and bottom views of the ρ = 1.7 $e^-/Å^3$ isosurface of the *total* electron density at the S2 apex tip atom (gray), along with the $d\rho$ = +0.17 $e^-/Å^3$ isosurface (orange), which is an order of magnitude smaller. Although this is a concern, it is possible that larger (or differently-shaped) tip structures will amplify the density increase at the apex. It is also important to remember that the experimental higher harmonic images were obtained using simultaneous STM/FM-AFM. The bias voltage between the

tip and the sample likely affected the electron density of the tip atoms and possibly played a role in the nature of the experimental images. SeqQuest has the ability to incorporate an electric field in the DFT simulations, so investigating the effect of the tip bias will be an important topic in future work; however, it is not covered in this dissertation.

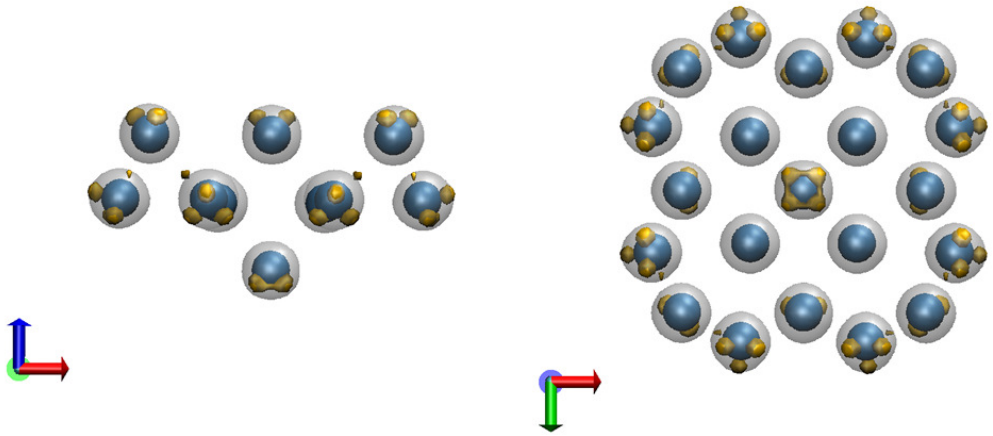

Figure 4.7 – A comparison of the total density (ρ) to the change in density ($d\rho$) after a self-consistent field calculation for the S2 tip. The ρ = 1.7 $e^-/Å^3$ isosurface of the total density is shown in gray, along with the $d\rho$ = +0.17 $e^-/Å^3$ isosurface shown in orange.

Although the discussion thus far has been limited to [001] oriented tungsten tip structures, the fact that the crystallographic orientation of the apex tip atoms is not known during any given experiment makes the investigation of multiple tip structures critical to this work. Chapter 7 will touch on this topic further, as it explores the connection between the tip's electron density and experimentally observable image contrast, but first we turn to the initial simulations of higher harmonics images, which revealed important

challenges to demonstrating the feasibility of subatomic imaging with atomic force microscopy.

4.4. – Simulating Higher Harmonics AFM: Initial Results and Challenges

4.4.1. The NPTH System

For the purposes of method development, the graphite surface was approximated with the two carbon-ring NPTH surface. To simulate the tip-sample interaction, SeqQuest was used to create a 6x6 grid (see Figure 4.8) of relaxed energy curves from 6.00 Å down to 1.25 Å (in steps of 0.25 Å) above the NPTH surface, with the *z*-distance defined as the distance between the centers of the apex tungsten tip atom and the surface atoms prior to relaxation. Over each (*x*, *y*) grid point, the S2 tungsten tip began 6.00 Å above the surface. The system was allowed to fully relax, and then the tip atoms were shifted downward 0.25 Å before allowing the system to fully relax again. This process was repeated for the entire *z*-distance range and was automated using a bash shell script.

Each SCF calculation was converged to within 0.0020 Ry (0.027 eV). SeqQuest uses a modified Broyden blending scheme on the Hamiltonian matrix in its SCF updates, so this value is the maximum change of a Hamiltonian matrix element, as opposed to the maximum change of the total energy [78]. The geometry relaxation was governed by a force convergence criterion of 0.0010 Ry/bohr (41 pN). During each relaxation, the top

layer of the tungsten tip remained fixed, as did the hydrogen atoms on the edges of the surface structure.

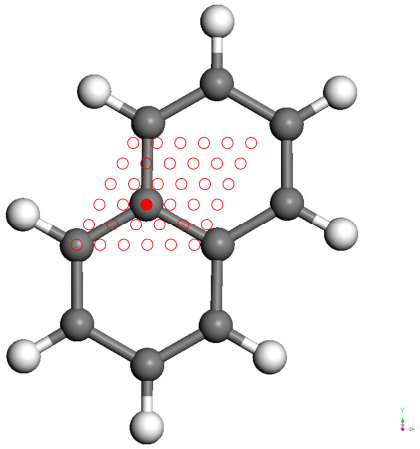

Figure 4.8 – The two carbon-ring NPTH surface used for method development. A 6x6 grid of relaxed energy curves was developed using SeqQuest. The solid red circle corresponds to the tip positions shown in Figures 4.4B, 4.5B, and 4.9.

It was found that the lobes of increased electron density on the tip interacted considerably with the surface as the *z*-distance between the tip and sample was reduced. In Figure 4.9A, the S2 tip is 6 Å above the surface (at the grid position indicated by the solid red point in Figure 4.8), while in Figure 4.9B the tip is 1.25 Å above the same position. The presence of four lobes of increased electron density on the tip's apex atom and their interaction with the carbon ring surface are promising results, but ultimately we must determine if these lobes are resolvable via higher harmonic FM-AFM.

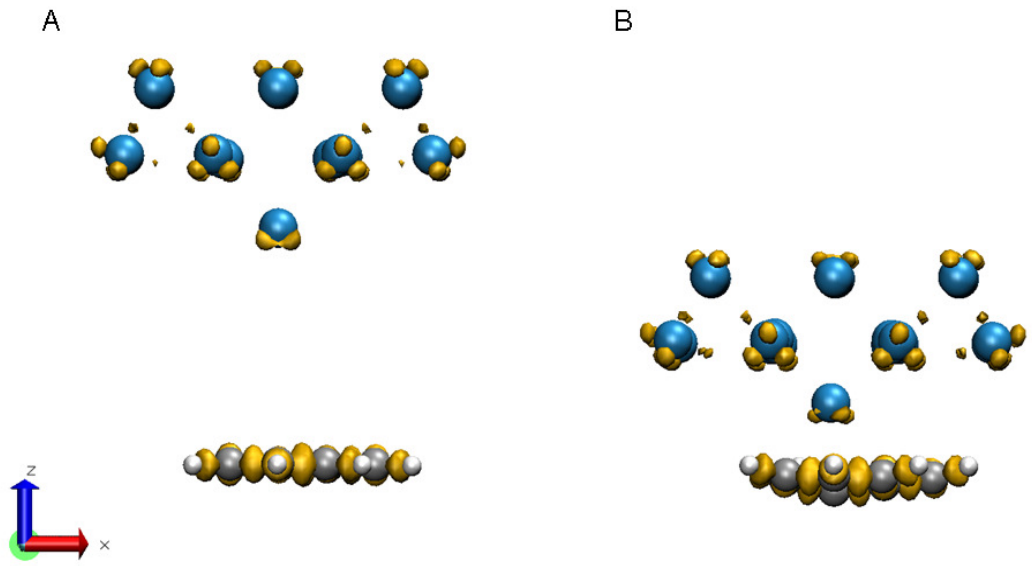

Figure 4.9 – The S2 tip structure (A) 6 Å above the surface (the grid position indicated by the solid red point in Figure 4.8), and (B) 1.25 Å above the same position.

4.4.1.1. Curve Fitting the DFT Data

The iterative tip-sample approach performed in SeqQuest for the S2 tip over the NPTH surface produced a three-dimensional grid of 720 (6x6x20) relaxed energy data points, i.e., 36 relaxed energy approach curves consisting of 20 data points each. In order to generate force curves, these energy curves were fit to a function that was then analytically differentiated with respect to z: $F(z) = -\nabla E(z)$.

Finding the optimum function for curve fitting is a critical step. An ill-fitting function undermines the precision of the DFT simulations, which are at the core of this method. The standard Morse potential, given by

$$V(z) = De\left\{1 - \exp\left[-\beta(z)\cdot\left(z - z_e\right)\right]\right\}^2 - De \tag{4.1}$$

where *De* is the depth of the potential well, z is the tip-sample distance, z_e is the equilibrium separation and $\beta(z)$ = constant, is one such ill-fitting function. One can alter the Morse potential with correction terms to achieve a more accurate fit to the data (for example, $\beta(z)$ can be given a linear or even quadratic form), but in *some cases* these modified energy functions result in force curves that do not have well-behaved slopes in regions away from the 20 data points (see Figure 4.11). This is relevant because we are interested in not only the first energy gradient (to obtain the force), but also the higher energy gradients that couple to the higher harmonics of the cantilever motion. While it may seem obvious, the best functional form will be specific to each tip-sample system, and one must always take care to determine it. It is important to note that poorly behaved force functions do not necessarily need to be discarded, but they must be implemented with care. The determining factor in all cases is the fundamental oscillation amplitude that is to be used to calculate the higher harmonics from the theory of Dürig (see Eqn. 3.15 in Section 3.2.2). We will return to this last point in Chapter 7.

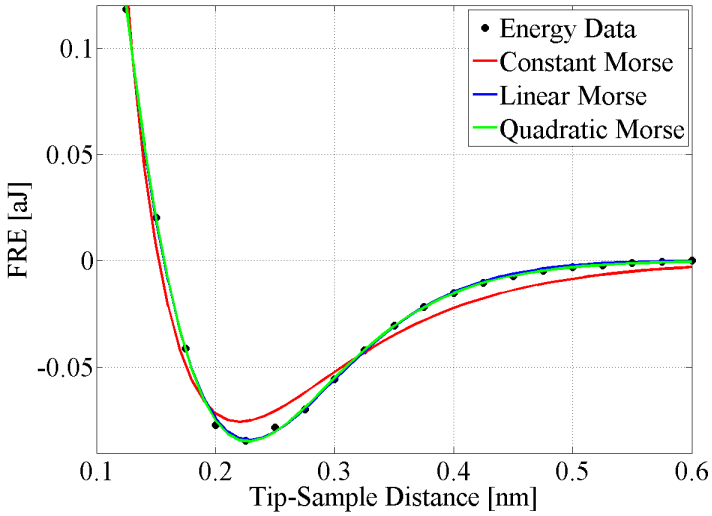

Figure 4.10 – Better fits can be achieved by giving $\beta(z)$ a linear or quadratic form in the standard Morse potential (Eqn. 4.1), but doing so may result in force curves with ill-behaved slopes in regions away from the 20 relaxed energy data points (see Figure 4.11).

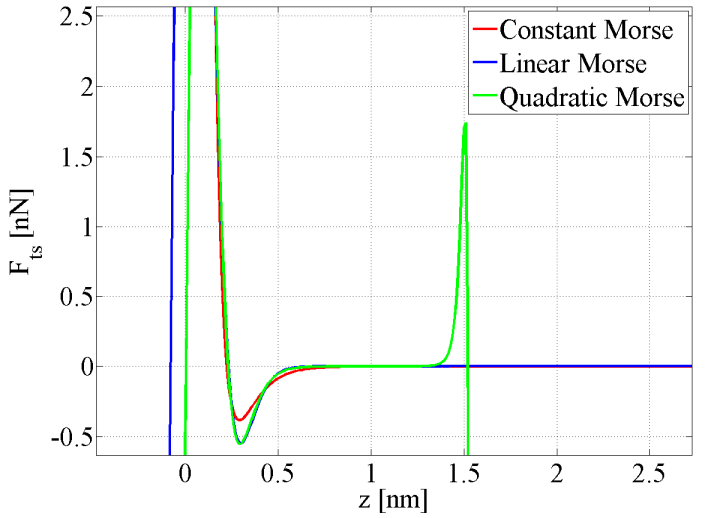

Figure 4.11 – The force curves resulting from the energy curve fits of Figure 4.10, illustrating the potential problems with linear and quadratic Morse potential.

For the NPTH system, the best energy fit was determined to be the four-parameter Levine potential [86], given by

$$V(z) = De\left\{1-\left(z_e/z\right)\cdot\exp\left[-\beta\cdot\left(z^p - z_e{}^p\right)\right]\right\}^2 - De \tag{4.2}$$

where p is not restricted to integer values. This function exhibits a better fit to the relaxed energy data than Morse, while remaining well-behaved in regions away from the 20 data points. An illustrated comparison between Morse and Levine for an example NPTH energy curve is shown in Figure 4.12.

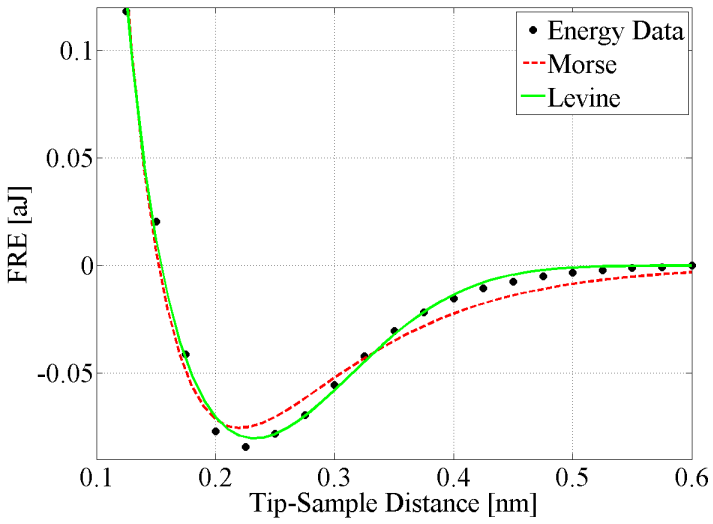

Figure 4.12 – An example of relaxed DFT energy data (black dots) for the NPTH-S2 system with the corresponding Morse (dashed red line) and Levine (solid green line) fits. The latter was used in the simulation data presented in this section.

4.4.1.2. van der Waals Correction

After the analytical differentiation of the fitted energy curves, the resulting short-range force functions were combined with a long-range van der Waals force, which for a spherical tip above a flat surface is given by

$$F_{vdW}\left(z_{vdW}\right)=\frac{-A_H R}{6 z_{vdW}^2} \tag{4.3}$$

where A_H is the Hamaker constant (~1 eV for solids; a value of 1.25 eV was used in this work), R is the radius of the tip (150 nm was used for the tungsten tip), and z_{vdW} is the distance between the surface atom centers and the edge of the spherical tip [14]. Note that $z_{vdW} = z + OS$, where OS is the distance offset between the edge of the spherical tip and the center of the apex tip atom in the simulated cluster (see Figure 4.13).

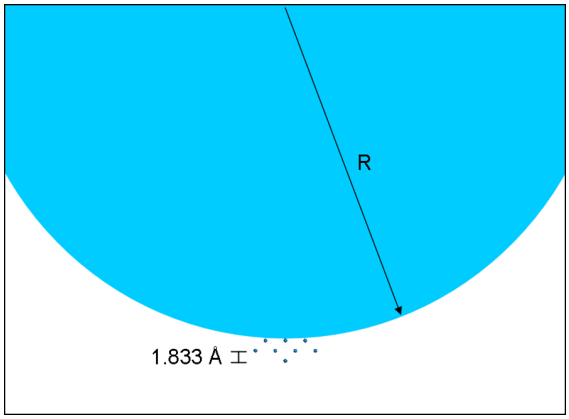

Figure 4.13 – Illustration of the vdW radius for the macroscale tip with the atomistic S2 cluster that is simulated with DFT.

The effect of the tip radius and the number of offset layers on the higher harmonics images will be discussed in Section 4.4.1.4.

4.4.1.3. AFM Simulation

In order to obtain the higher harmonic amplitudes needed to simulate the constant-height experimental images of Hembacher *et al*., continuum simulations of a quartz tuning fork oscillating above a graphite surface were performed at each specified grid location (recall Figure 4.8), i.e., in the presence of each individual force curve. Thus, each force curve requires a separate simulation, with the base position of the tuning fork being the same for each.

The simulator is written in the C programming language and implements the Verlet algorithm [73, 74, 87] for the numerical integration of the first three eigenmodes of the tuning fork in UHV (f_0 = 18 kHz; k_0 = 1800 N/m; Q_0 = 20,000). Consistent with FM-AFM operation, the tuning fork is self-oscillated, meaning that the excitation frequency is updated every oscillation cycle. However, the excitation force amplitude is not adjusted during the course of the simulation, as it would be experimentally. Instead the drive is kept constant and the simulation is allowed to run until the oscillation amplitude has stabilized. Stable oscillation is typically reached after ~3 seconds. Figure 4.14 is a typical plot of the measured effective frequency versus the oscillation number. The dotted black line is drawn at the 18 kHz fundamental cantilever frequency, f_0. The dotted red line marks the stabilized effective resonance, f_{eff}. The frequency shift is taken as the difference between these two values:

$$\Delta f = f_{eff} - f_0 \tag{4.4}$$

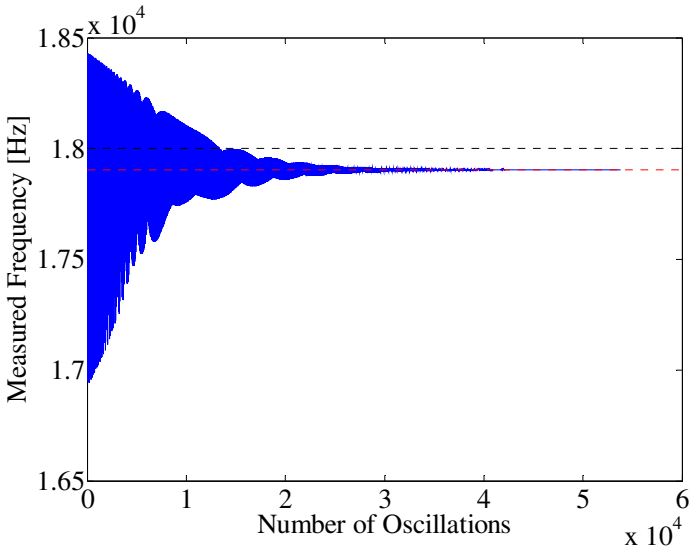

Figure 4.14 – The frequency of each cantilever oscillation of the continuum simulation is tracked. The fact that the oscillation amplitude is not controlled means that the frequency shift takes time to stabilize in the presence of each force curve. Here the dotted black line is at the 18 kHz fundamental frequency. The dotted red line marks the stabilized effective resonance. The frequency shift is then the difference between the two.

MATLAB software was used to simulate the experimental images. The frequency shift at each grid point is readily accessible from the steady-state tuning fork oscillation, but the higher harmonics require additional processing. Consistent with experiment, the trajectory is high-pass filtered before collecting the amplitudes of the higher harmonics from a Fast-Fourier Transform (FFT).

Hembacher *et al*. used a programmable Stanford Research Systems SR650, which is an 8-pole elliptic-type high-pass filter with 0.1 dB of passband ripple and 80 dB of stopband attenuation [35] and is easily simulated with MATLAB's `ellip` function. They

used a cutoff frequency of 20 kHz in order to eliminate the fundamental frequency of ~18 kHz. The combined higher harmonics signal is the voltage output from the filter, given by

$$V_{hh} = \left(\sum_{2}^{\infty} \left(S_n a_n \right)^2 \right)^{1/2} \tag{4.5}$$

where S_n is the sensitivity of the deflection sensor for the nth harmonic [1],

$$S_n \approx \frac{n}{\left(1 + 0.0767 n^2\right)^{1/2}} \times 0.1 \text{ mV/pm} \tag{4.6}$$

The justification for collecting the harmonics this way is given in Ref. [33], as well as in Note 22 in Ref. [1]. The crux of the argument is that (simulated) images produced by individual higher harmonics are similar; therefore, collecting a quasi-rms sum of all higher harmonics will not change the nature of the image. Further, collecting all harmonics offers ease of implementation and increases the signal-to-noise ratio. This experimental technique will be explored further in Chapter 6, which deals exclusively with the effects of signal processing on the higher harmonics images obtained.

The higher harmonics in the FFT of an example filtered tip trajectory (above a single surface grid point) are shown in Figure 4.15. Note that the amplitudes are on the order of 10^{-2} pm, with the horizontal dotted green lines indicating the amplitude of each harmonic. While the amplitude of each harmonic is quite small, each represents physical cantilever deflection. In an experiment however, the harmonic amplitudes are measured as voltages – with the piezoelectric detection of the qPlus sensor providing increasingly enhanced sensitivity to each a_n as n increases (as discussed in Section 3.3). Also visible is

the peak corresponding to the second eigenmode at approximately 113 kHz. The higher harmonics voltage V_{hh} for each surface grid point is obtained via Eqns. 4.5 and 4.6.

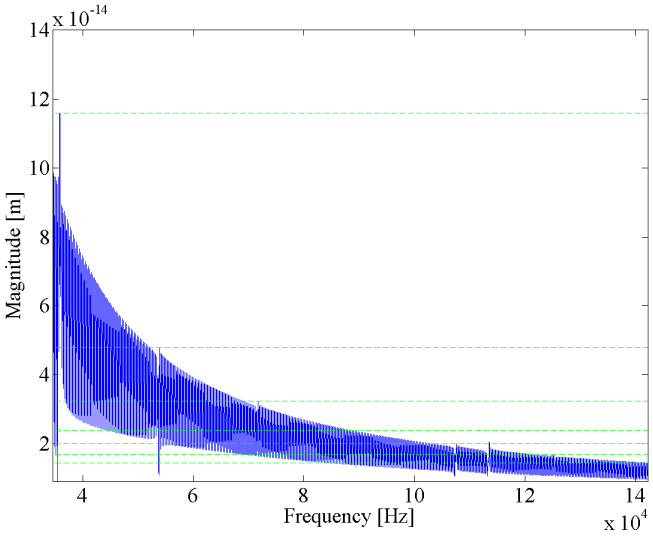

Figure 4.15 – Example FFT of a filtered tip trajectory revealing small but measurable higher harmonics. The horizontal dotted green lines indicate the amplitude of each harmonic. The peak corresponding to the second eigenmode at ~113 kHz is also visible.

4.4.1.4. Simulated Images and the Effect of the vdW Offset

Simulated constant height Δf (top) and V_{hh} (bottom) images for the S2 tip above the NPTH surface are shown in Figure 4.16 and 4.17 for a two-layer and five-layer macroscopic vdW offset (refer to Figure 4.13), respectively. The grid above the surface has been repeated five times in both the x- and y-directions and then cropped to produce a rectangular image. The Levine potential was used to fit the DFT data for the 6x6 surface grid shown in Figure 4.8. The oscillation amplitude is 3 Å and the distance of closest

approach (z_c) is 1.50 Å. The frequency shifts are given in Hz and the higher harmonics voltages in mV.

Each Δf image clearly demonstrates atomic resolution of the graphite lattice – a single hexagon of which has been drawn over the carbon atom positions. It is interesting to note that in both cases, while the apex tip atom probes the repulsive regime of the force curve (z_c = 1.50 Å), the overall frequency shift remains negative. This is due to the large radius (150 nm) used to represent the macroscopic portion of the tip, and the fact that its closest approach remains in the attractive force regime due to the offset layers. While increasing the number of layers between the apex and macroscopic tip does not change the *qualitative* nature of the frequency shift images, it does decrease the attractive contribution to the overall frequency shift as reflected in the contour scaling.

The V_{hh} images were created using seven harmonics in the summation (see Eqn. 4.5). The V_{hh} image for the two-layer offset (Figure 4.16) does not show the four lobes of increased charge density (see Figure 1.2F); however, there is a clear visual difference between the two inequivalent carbon atoms that make up the ring. It is possible that differences in bonding for the two carbon atoms that comprise the unit cell of graphite play a role in this image contrast, but the electron density of the tip model (Figure 4.5B) is not reproduced. However, four-fold symmetry features do appear in the V_{hh} image for the five-layer offset shown in Figure 4.17. For comparison with the experimental image (Figure 4.18), the five-layer offset V_{hh} image is displayed with the circumference of a tungsten atom (dotted red circle) and carbon atom (white circle) in Figure 4.19. The white cross marks the location of the carbon atom on the surface. Note that the four-fold symmetry features of the simulated image are smaller than those in the experimental one,

and appear to be offset from the center of the carbon atom. For a clearer comparison to the atom sizes, the representative circles are shifted to the center of the four maxima in Figure 4.20.

z_c = 1.50 Å

***OS* = 2**

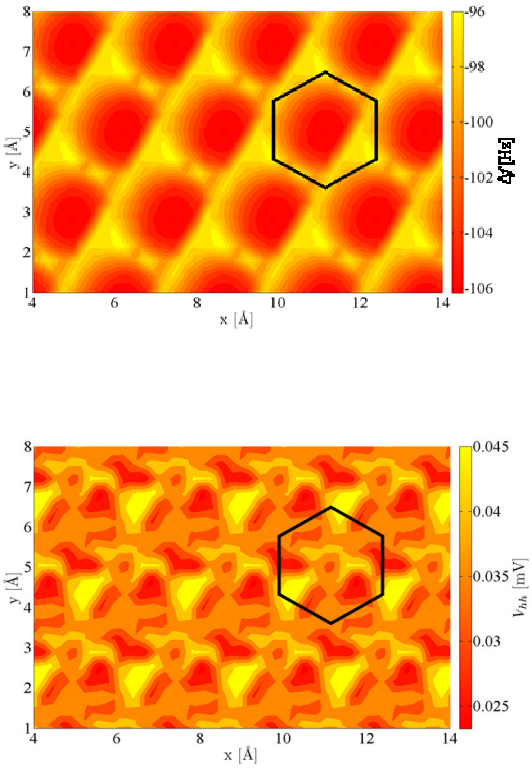

Figure 4.16 – Simulated constant height Δf (top) and V_{hh} (bottom) images for the NPTH system. The distance of closest approach z_c = 1.50 Å and two vdW offset layers are used (i.e., *OS* = 2).

z_c = 1.50 Å

***OS* = 5**

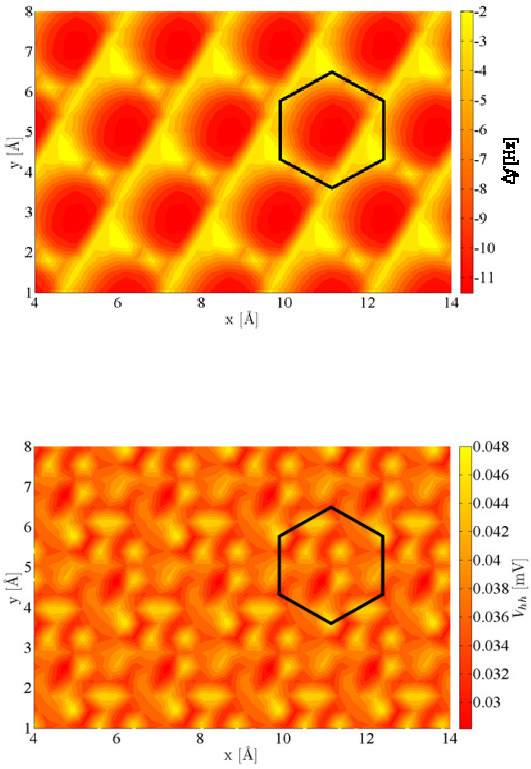

Figure 4.17 – Simulated constant height Δf (top) and V_{hh} (bottom) images for the NPTH system. The distance of closest approach z_c = 1.50 Å and five vdW offset layers are used (i.e., *OS* = 5).

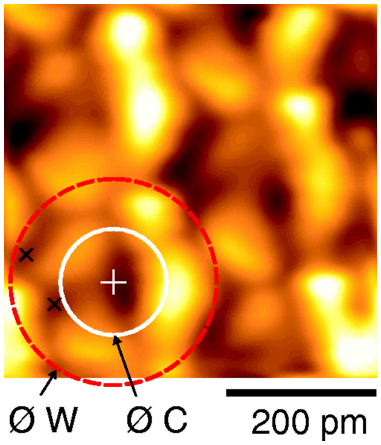

Figure 4.18 – Hembacher experimental V_{hh} image for comparison.

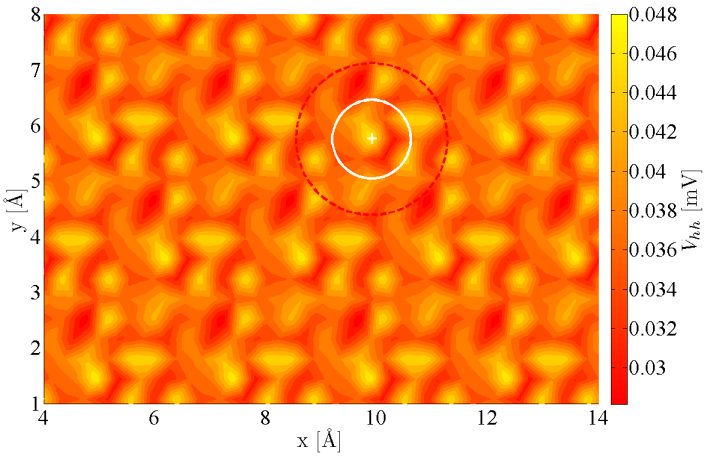

Figure 4.19 – The five-layer offset V_{hh} image of Figure 4.17 (bottom) displayed with the circumference of a tungsten atom (dotted red circle) and carbon atom (white circle). The white cross marks the center of the carbon atom on the surface.

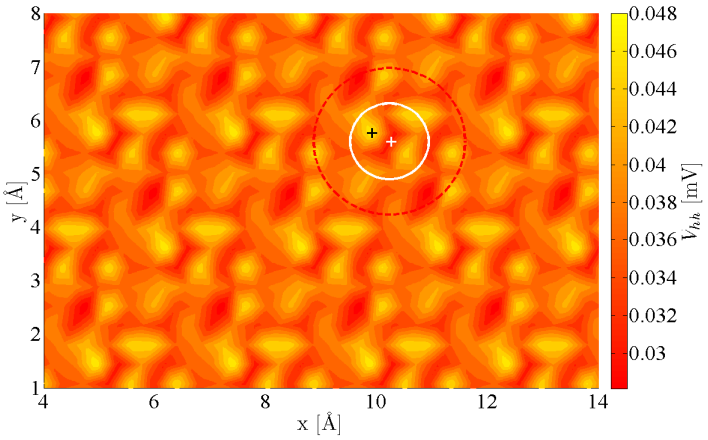

Figure 4.20 – The five-layer offset V_{hh} image of Figure 4.17 (bottom) with the circles illustrating atom size shifted to the center of the four maxima.

To understand why the number of vdW offset layers between the apex atoms and macroscopic tip results in such drastic changes to the higher harmonics image, it is instructive to view the offset's effect on the tip-sample force curves, shown in Figure 4.21. Clearly the number of offset layers between the micro- and macroscopic tip structures significantly alters the curvature of F_{ts}, which in turn alters the higher harmonics amplitudes. However, the first gradient remains relatively unchanged, which explains the qualitative similarity between Δf images. As the number of offset layers is increased, the force curve also becomes dominated by the short-range component, which is an intuitive result.

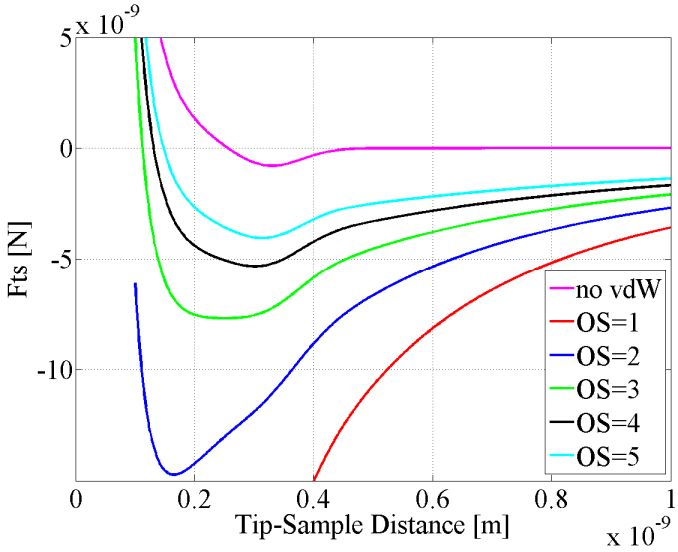

Figure 4.21 – The effect of the vdW offset (OS) on the tip-sample force curve. As the number of layers between the micro- and macroscopic parts of the tip is increased, the force curve becomes dominated by the short-range component.

The other variable that affects the contribution of the vdW force component is the tip radius, R, as illustrated in Figure 4.22. The proportionality of F_{vdW} to the first power of R (as opposed to the square of the vdW offset, OS) makes the effect of the tip radius less dramatic. From Eqn. 4.3, we already know that a smaller tip radius equates to a smaller F_{vdW} contribution to the total force, and hence to a stronger dependence on the short-range component, which is why sharp tips provide higher resolution. However, we chose not to investigate the qualitative effect of the tip radius on the simulated images because our results to this point made it clear that the continuum simulation produced an undesirable level of uncertainty for the purposes of establishing a fundamental connection between the electron density of the tip and subatomic features in the higher harmonics images. Fortunately, a simpler approach exists, as discussed in the next (and final) section of this chapter.

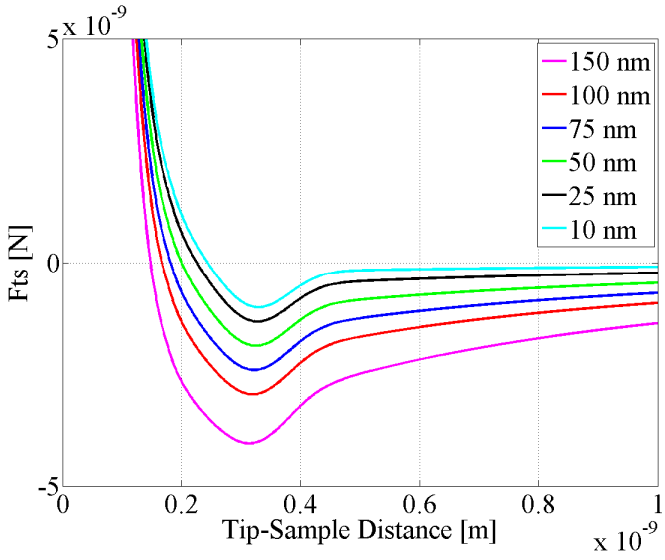

Figure 4.22 – The effect of the vdW tip radius on the tip-sample force curve.

4.4.2. A More Fundamental Approach

Before attempting to draw any conclusions from a full-scale theoretical simulation of the 2004 experiment, one should be able to determine if the harmonic amplitudes calculated *directly* from Dürig's equations can produce sub-atomic contrast (which by Hembacher's argument they should [1]). The advantage of calculating the purely theoretical frequency shift and higher harmonic amplitudes this way is two-fold. First, it allows one to study the most *ideal* imaging scenario. Thus, if the subatomic contrast cannot be reproduced in this manner, then one can conclude that there is no true connection between the electronic density at the apex tip atom and the subatomic features of the higher harmonics images. Second, if the higher harmonics images *do* reflect the apex atom electron density, then the calculated ideal amplitudes establish a baseline for

evaluating the effects of each continuum simulation parameter on the "measured" amplitudes.

Note that proceeding in this manner eliminates only the variables inherent to the continuum simulation. One must still use DFT on a model atomistic system to develop the force curves necessary to carry out the purely theoretical calculations. This means that one must still consider the accuracy of the atomistic model itself, as well as the parameters used in the DFT calculation. Unfortunately, there is no way to gauge the accuracy of the atomistic model *a priori*. However, with regard to the DFT parameters, one may take a small measure of solace in the fact that the physical accuracy of a DFT calculation for a given system is determined entirely by the choice of the exchange-correlation functional (or simply "the functional"), which defines the Kohn-Sham equations (refer to Section 3.5.2). In this case, we can also be confident in the fact that SeqQuest is a well-established DFT code with robust local orbital basis sets.

In the next Chapter, we explore this new, more fundamental approach again using the W(001) S2 tip but this time probing the more realistic 9R surface structure shown in Figure 4.2B.

5. Demonstrating the Feasibility of Observing Subatomic Features

This chapter is an adaptation of the work published in Nano Letters [2]. While the description of the experimental background present in the published work has been largely excluded, there remains some repetition of certain topics discussed earlier in this dissertation. These redundancies make this chapter self-contained, and as such have been preserved.

5.1. – Introduction

We begin with a summary of the important features of the 2004 experiments [1] that must be considered in a full theoretical treatment of the same: 1) the crystallographic plane of tungsten responsible for image contrast, and the presence of bulk-like surface states in a non-bulk system such as an AFM tip, 2) the effect of simultaneous STM/AFM on the electronic states of the system, 3) the cantilever dynamics, and 4) the effect of filtering the cantilever trajectory. In this chapter we focus on the first feature, with the specific objective of reproducing the four-fold symmetry features of Figure 1.2F (reprinted as Figure 5.11C). Ultimately, to study the effect of the cantilever dynamics and control systems on the imaging process, continuum simulation (and thus multiscale

modeling) is necessary. However, the validity of the interpretation must first be tested in the most ideal imaging scenario. To this end, we can avoid the additional uncertainty of the cantilever dynamics and the filtering of a simulated cantilever trajectory by calculating the frequency shift and amplitudes of the higher harmonics directly from the fundamental theory of Dürig (see Eqn. 3.15), which by the argument of Hembacher *et al*. should reproduce the sub-atomic contrast seen experimentally. The advantage of calculating the purely theoretical frequency shift and higher harmonic amplitudes this way is two-fold.

First, as mentioned previously, it allows one to study the most *ideal* imaging scenario in which the higher harmonics amplitudes can be calculated aside from any artifacts that could be introduced through the experimental processing of the cantilever deflection signal. (One of the major points of critique that has been brought up against the work of Hembacher *et al.* is the hypothesis that the four-fold symmetry features could be the result of filtering artifacts; we discuss this in the next chapter.) Consequently, if the subatomic contrast cannot be reproduced in this manner, then one can readily conclude that there is no true connection between the electron density at the apex tip atom and the subatomic features of the higher harmonics images.

Second, if the higher harmonics images *do* reflect the apex atom electron density, then the calculated *ideal* amplitudes establish a baseline for evaluating the effects of the cantilever dynamics and filtering which would be introduced in a full multi-scale simulation.

5.2. – Tip and Surface Models

The W(001) tip and graphite surface models used are shown in Figure 5.1. The DFT code SeqQuest developed by Shultz at Sandia National Laboratory [78] was used to run all calculations (the computational methods are described in detail in the Sections 4.3 and 4.4). Recalling that quantum mechanics calculations of the W(001) surface reveal four lobes of increased charge density above the top layer atoms, the first question we wish to answer is: Are similar lobes present in *non-bulk* systems such as AFM tips? Plotted in Figure 5.2A is a single isosurface (isovalue = +0.2 $e^-/Å^3$) of the change in electron density, $d\rho$, for the tip structure investigated[1]. Four lobes of increased charge density are indeed visible at the apex atom of the structure (indicated by the red square). While the presence of the four lobes of increased charge density in a non-bulk tip structure is a promising result, it is important to note that the *value* of the density increase is small in comparison to the total electron density in the same region of space. Figure 5.2B illustrates the ρ = 2.0 $e^-/Å^3$ isosurface of the total electron density at the apex tip atom (gray), along with the $d\rho$ = +0.2 $e^-/Å^3$ isosurface (orange), which is an order of magnitude smaller.

[1] In DFT, the initial electron density ρ_0 in the tip-sample system is a superposition of the individual atom electron densities. During each self-consistent field (SCF) calculation for the system, the change in electron density $d\rho$ is calculated. The total electron density for the system is then the sum of the initial density and the change.

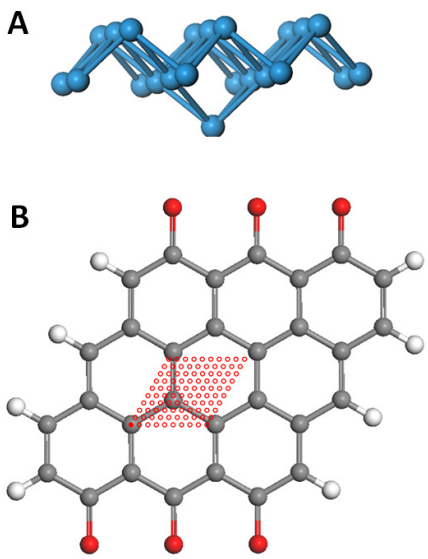

Figure 5.1 – The three-layer W(001) tip structure (A) and graphite top layer (B) studied in this work. The model surface of graphite consisted of a 9-carbon-ring top layer edge-terminated with either oxygen or hydrogen depending on which was needed to maintain the sp^2 hybridization of the carbon atoms. This model also contains a 4-carbon-ring second layer that has been excluded in this figure for clarity. The second layer is included in order to reproduce the difference in electronic states between α- and β-surface carbon atoms. The red circles indicate the grid points for which tip-sample force curves were calculated.

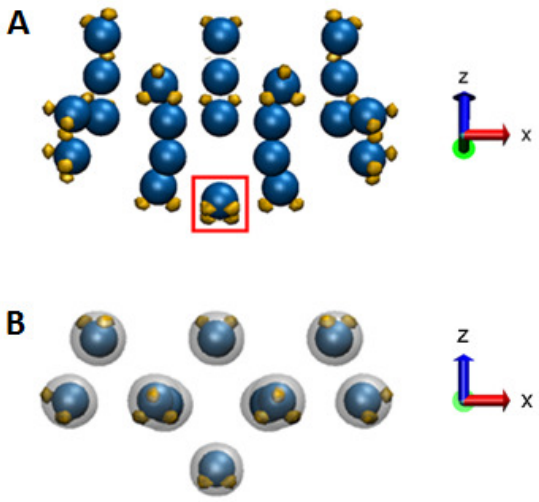

Figure 5.2 – (A) A single isosurface (isovalue = +0.2 $e^-/Å^3$) of the change in electron density for the model tip structure used. The view is at an angle from below. The apex atom is indicated by a red square. Four lobes of increased charge density are visible. (B) Comparison of the total density (ρ) to the change in density ($d\rho$) after a self-consistent field calculation for the tip. The ρ = 2.0 $e^-/Å^3$ isosurface of the total density is shown in gray, along with the $d\rho$ = +0.2 $e^-/Å^3$ isosurface shown in orange.

Note that only *single* isosurfaces are plotted in Figure 5.2. For this specific case, density changes in the interior of the tip structure are not visible because none occur at the selected isovalue ($d\rho$ = +0.2 $e^-/Å^3$). Plotted in Figure 5.3 are two cross sections through the entire change in electron density of the model tip structure, showing all isovalues. Figure 5.3B indicates that four lobes are also present below the center atom in the top layer of the tip, which is to be expected since this is one of the most bulk-like atoms in the system.

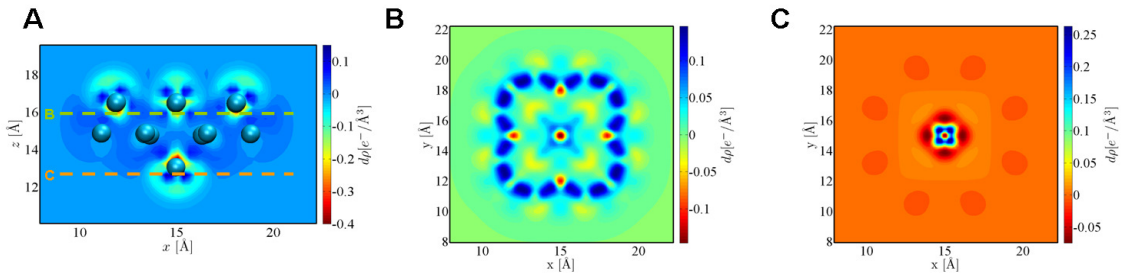

Figure 5.3 – (A) Side view of the change in electron density ($d\rho$) for the model tip structure, indicating the location of horizontal cross sections taken directly below the topmost tip layer (B) and directly below the apex atom (C). Horizontal cross section B reveals four bonding lobes below the top layer's center atom and horizontal cross section C reveals four smaller lobes below the apex tip atom, with all isovalues of $d\rho$ included.

5.3. – Force Curve Calculation

In order to calculate the force curves necessary to simulate the frequency shift and higher harmonics images, the tip model was placed above the surface at each red grid point shown in Figure 5.1B. Data points were calculated from 6.00 Å down to 1.00 Å (in steps of 0.25 Å) above the surface, with the z-distance defined as the distance between the centers of the apex tungsten tip atom and the surface atoms, prior to relaxation. Over each surface grid point, the tungsten tip began 6.00 Å above the surface. The system was allowed to fully relax, and then the tip atoms were shifted downward by 0.25 Å before the system was allowed to relax again[2]. This process resulted in 100 relaxed energy curves each consisting of 21 data points, an example of which is shown in Figure 5.5,

[2] Each SCF calculation was converged to within 0.0020 Ry (=0.027 eV). The geometry relaxation was governed by a force convergence criterion of 0.0010 Ry/bohr. During each relaxation, the top layer of the tungsten tip remained fixed, as did the oxygen and hydrogen atoms on the edges of the surface structure.

which is the curve calculated above the solid red grid circle of Figure 5.1B (directly above one of the carbon atoms). In order to generate force curves, each energy data set was fit to a function that was then analytically differentiated with respect to z: $F(z) = -\nabla E(z)$.

Finding the optimum function for curve fitting is a critical step. An ill-fitting function undermines the precision of the DFT simulations, which are at the core of this method. In this particular case, the standard three-parameter Morse potential is one such ill-fitting function. One can alter the Morse potential with correction terms to achieve a more accurate fit to the data, but in *this* case these modified functions either do not offer a satisfactory improvement (e.g., the four-parameter Levine potential [86]), or offer an improved fit but do not have well-behaved slopes in regions away from the 21 data points (see Section 4.4.1.1). This is uniquely relevant to higher harmonics AFM simulation because we are interested in not only the first energy gradient (to obtain the force), but also the higher energy gradients that couple to the higher harmonics of the cantilever motion. The issue of curve fitting the DFT data is of less importance in the simulation of standard frequency shift images because slight deviations from the data do not result in drastic qualitative differences between simulated images but instead alter only the quantitative frequency shift values. To ensure continuous, realistic force curves, we used an in-depth, two-stage fitting method which is discussed in the next subsection.

5.3.1. Two-Stage Curve Fitting

Allowing the tip and surface atoms the freedom to relax (excluding the top-layer tip atoms as well as the oxygen and hydrogen surface edge atoms) meant that attractive and repulsive forces could cause significant geometry deformations, as illustrated in Figure 5.4, which shows the tip (from left to right) 6 Å, 3 Å, and 1 Å above the surface. The relevant consequence of this was a broadening of the tip-sample interaction potential well, which in turn meant that standard interaction potential functions such as Morse, Levine, and Lennard-Jones did not fit the data well. Figure 5.5 shows the energy data acquired over the solid red circle of Figure 5.1B with the Morse and Levine fits overlaid. (The Lennard-Jones fit is not shown, as it was far worse than the others.) Because the Morse and Levine functions did not accurately capture the nature of the potential well, we developed an alternative, two-stage, curve-fitting approach.

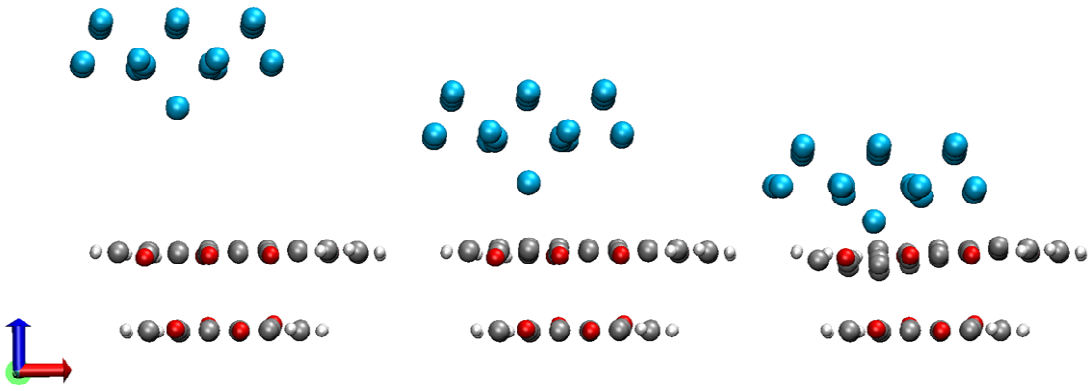

Figure 5.4 – The ability of the tip and surface atoms to relax meant that attractive and repulsive interactions caused large deformations in the surface geometry. From left to right, the tip is 6 Å, 3 Å, and 1 Å above the solid red surface grid position of Figure 5.1B.

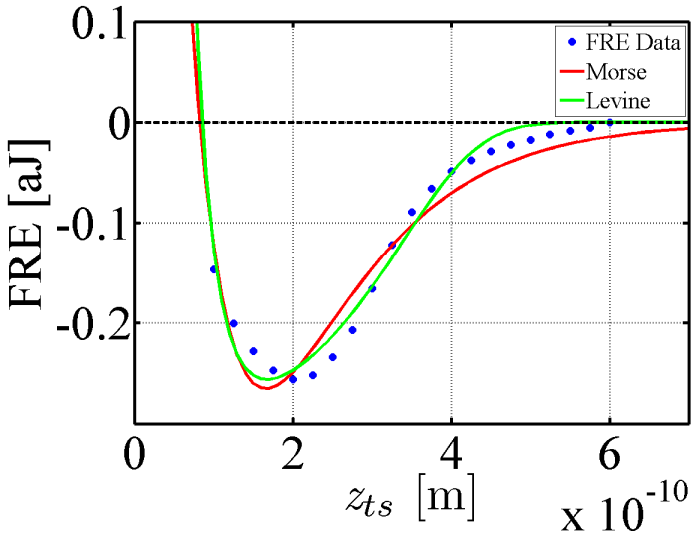

Figure 5.5 – Final Relaxed Energy (FRE) DFT data for the tip-sample interaction (over the solid grid point of Figure 5.1B) illustrating the poor fits of both the Morse and Levine potentials. All of the energy curves exhibited a similar broadening of the interaction potential well with respect to these standard fits, necessitating a different curve fitting strategy.

To begin, the final relaxed energy data was fit to a 9th-order polynomial (hereafter referred to as a Poly9 fit). Figure 5.6 shows how accurate the Poly9 fit is to the DFT data, while the larger-range view of Figure 5.7 demonstrates the shortcoming of such a fit for force curve development. Clearly a 9th-order polynomial is not a realistic representation of the tip-sample interaction for regions far from the surface. Figure 5.8 shows the force curve analytically calculated from the Poly9 fit.

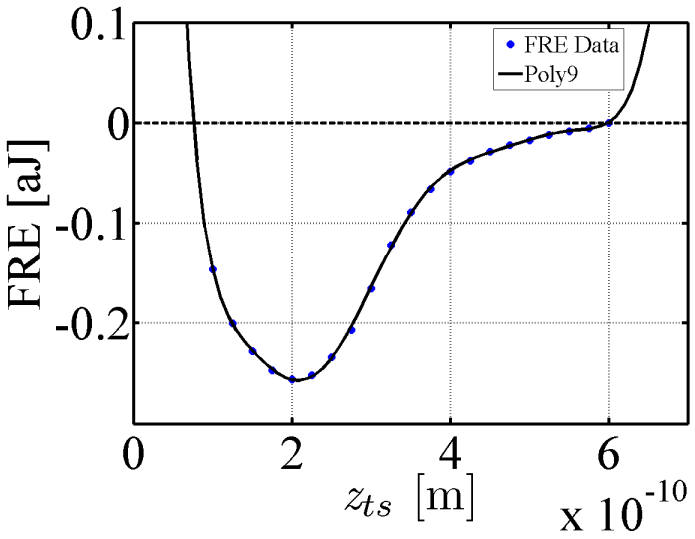

Figure 5.6 – The FRE data of Figure 5.5 fit to a 9th order polynomial.

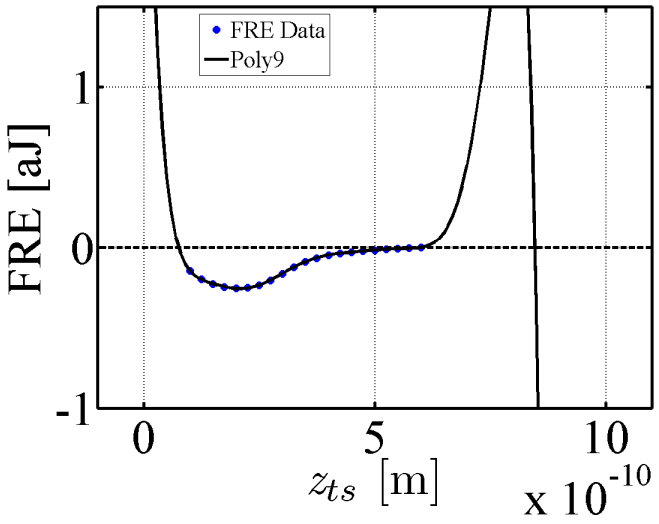

Figure 5.7 – A larger-range view of Figure 5.6 demonstrating the shortcoming of a 9th-order polynomial fit for developing a tip-sample force curve.

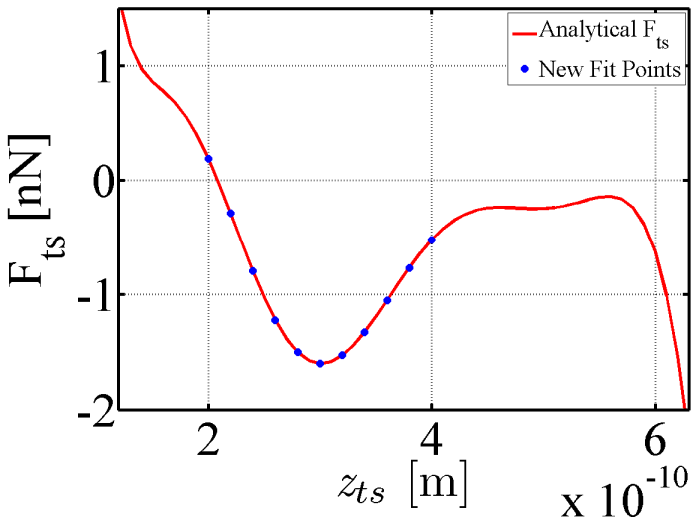

Figure 5.8 – Tip-sample force curve analytically calculated from the Poly9 curve fit. The blue points indicate the force data points that are subsequently used to fit to a Levine-based force function.

In order to circumvent the shortcoming of the Poly9 fit, a second curve fit was carried out using the blue data points of Figure 5.8 as a means to recreate the interaction well of the tip-sample force, while replacing the unrealistic regions of the force curve with a more realistic force model. The function used for the second fit was the differentiated Levine potential, multiplied by -1,

$$F_{Levine}(z) = -2De\left(1-\frac{z_e e^{-\beta(z^p - z_e^p)}}{z}\right)\left(z^{p-2} z_e p\beta e^{-\beta\left(z^p - z_e^p\right)} + \frac{z_e e^{-\beta\left(z^p - z_e^p\right)}}{z^2}\right) \qquad (5.1)$$

The fit to this Levine-type force function is illustrated in Figure 5.9.

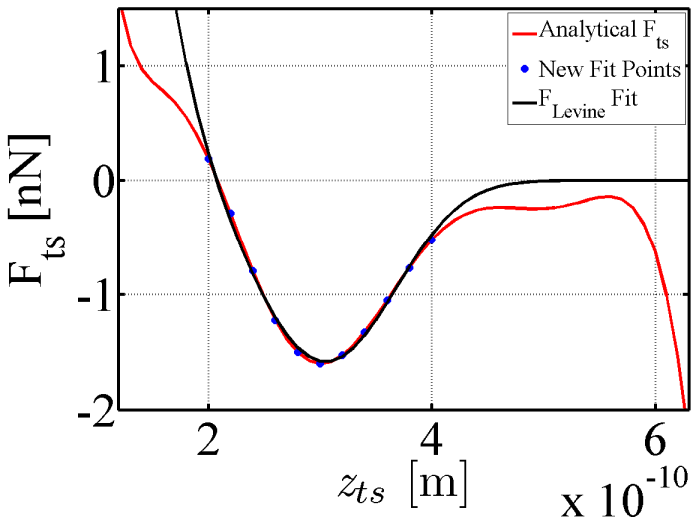

Figure 5.9 – A force function based on the Levine potential was used to fit the interaction well of the Poly9 tip-sample force.

In essence, this two-stage curve fitting method exploits the accuracy of the Poly9 fit to the FRE data and then truncates the regions where the fit is poor. This method was used to create force curves for the 100 grid points of Figure 5.1B.

5.3.2. Verifying Force Reconstruction

With the force curves calculated, we first determine the number of harmonics necessary to reconstruct the tip-sample force with the 3 Å oscillation amplitude used in the experiment. Figure 5.10B shows the force curve calculated from the energy data of Figure 5.10A as well as the reconstruction calculated from Dürig's equations (see Section 5.6 for details) using the first six harmonics of the 3 Å cantilever oscillation. The three vertical grid lines represent the cantilever base position (chosen to be 5 Å) and the two end points of the oscillation. Clearly the force curve is well reproduced over the range of

oscillation. (Additional reconstructions done with 3 and 9 harmonics can be found in Section 5.6.)

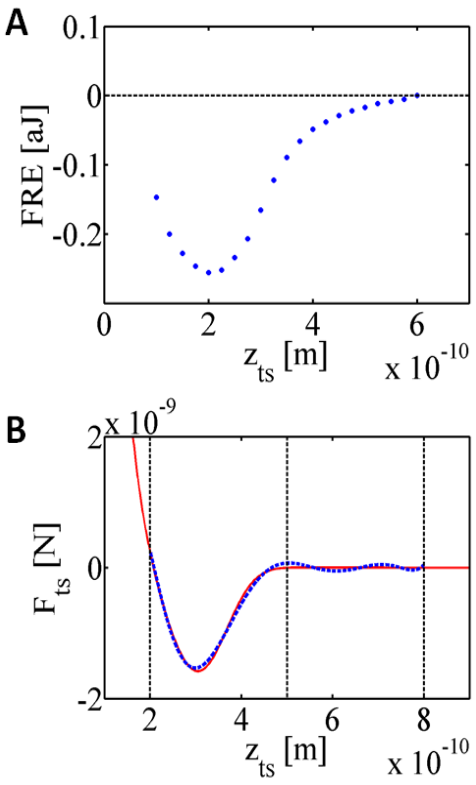

Figure 5.10 – (A) Example Final Relaxed Energy (FRE) [aJ] versus distance curve. Such curves were collected on all locations (red circles) shown in Figure 5.1B. Each point on the graph is the result of a separate simulation. (B) Example force curve developed through DFT and curve fitting (red trace) and the reconstruction of the force curve using 6 harmonics in Dürig's equations (blue dotted trace). These curves correspond to the location marked with the solid red circle in Figure 5.1B (directly above one of the carbon atoms).

5.4. – Simulated Images

We now proceed from Dürig's equations (Section 3.2.2.) and simulate experimental frequency shift (using Eqns. 3.3 and 3.13) and higher harmonics images (using Eqn. 3.15). We begin by focusing on the short-range force curves developed through the two-stage fitting method described above, disregarding the long-range van der Waals forces. Figure 5.11 shows simulated frequency shift (A) and higher harmonics, V_{hh} (B), images calculated using a 3 Å fundamental oscillation amplitude with the distance of closest tip-sample approach set at 1.88 Å. (Simulated images at varying closest approach distances are provided Section 5.6 for not only the tip discussed above, but also for a "blunt" tip whose apex is terminated with four atoms.) The gray color map was chosen simply because it provided the best visual contrast. A red hexagon has been overlaid to indicate the positions of the surface carbon atoms. To produce the higher harmonics image, the amplitudes of the first seven harmonics (based on the force reconstruction exercise of Figure 5.10) were entered into Eqns. 1.3 and 1.4 (see Section 1.3). While the graphite lattice is clearly visible in the simulated frequency shift image, four-lobed features similar to those observed experimentally appear in the simulated higher harmonics image (see also Figure 5.18, which was constructed using a blunt tip and in which the number of features in the higher harmonics image appears to multiply with the number of apex atoms).

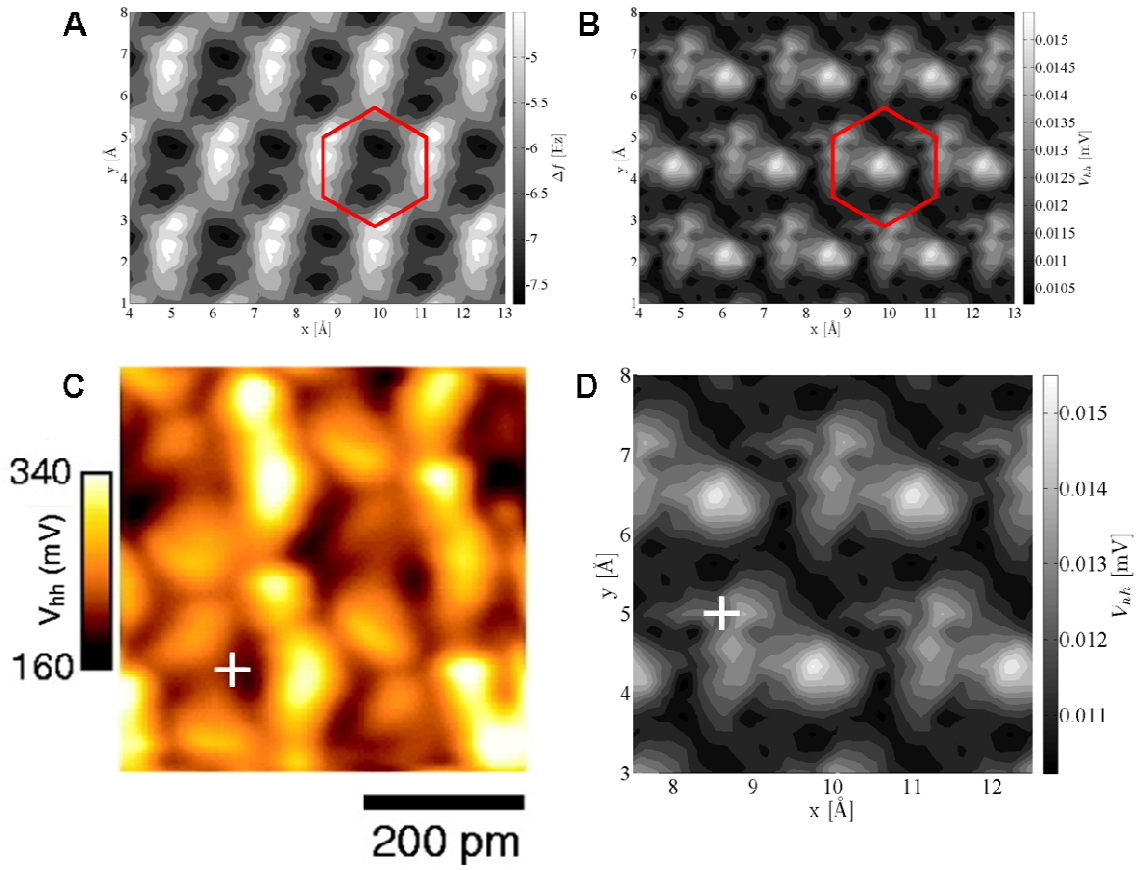

Figure 5.11 – Simulated frequency shift (A) and higher harmonics, V_{hh} (B), images calculated using Dürig's equations. The grid of Figure 5.1B has been repeated multiple times in both the x- and y-directions and then cropped to produce rectangular images. Here the distance of closest approach is 1.88 Å. A red hexagon has been overlaid to indicate the positions of the surface carbon atoms. While the graphite lattice is clearly visible in the frequency shift image, four-fold symmetry features similar to those observed experimentally appear in the simulated higher harmonics image. (C) and (D) show a close-up side-by-side comparison of the experimental (C) and simulated (D) V_{hh} images revealing four-fold symmetry features.

A direct comparison with the four-fold experimental higher harmonics image is instructive. Figure 5.11 also shows close-up views of both the experimental (C) and simulated (D) V_{hh} images revealing four-lobed features. In both cases, the features appear

within a 200 pm (2 Å) diameter. The white cross in the experimental image was placed at a maximum in the tunneling current image, which is presumed to occur directly above a surface carbon atom [1]. In a similar fashion, we have placed a white cross at the exact position of the nearest surface carbon atom in our simulation. Clearly the simulated features are not centered above a single carbon atom. In Figure 5.11B, we see that the brightest of the features actually occurs at a hole position on the surface.

The fact that the simulated features are *not* centered above a carbon atom is not necessarily problematic, but it suggests that the assumption by Hembacher *et al.* that the carbon atom position is the same in both tunneling current and higher harmonics images is not guaranteed to be accurate. The experimental observation of offsets between the maxima of simultaneously acquired data channels is not uncommon [88]. Note that a comparison between the simultaneously acquired tunneling current and higher harmonics images of Figures 1.2A and 1.2B, as well as Figures 1.2C and 1.2D, reveal that even in these instances, the subatomic features are not centered about a maximum in the tunneling current.

Another clear difference between the experimental and simulated higher harmonics images is the symmetry of the four-fold features. While the lobes near the white cross on the experimental image (Figure 5.11C) appear to be approximately equal in weight, those in the simulated image do not. A possible explanation for this disparity is the influence of the pinned hydrogen and oxygen atoms on the edge of the model surface. It is reasonable to conclude that the lack of exact bonding symmetry in the surface model would lead to a lack of symmetry in the calculated force curves and hence in the

simulated higher harmonics images as well. Additionally, close inspection of the experimental image shows that the lobe symmetry is not uniform throughout the surface.

Figure 5.12 shows vertical cross sections of the calculated tip-sample forces, which offer further insight into our simulated images. Figures 5.12A and B indicate the location of the cross sections relative to the simulated frequency shift and higher harmonics images of Figures 5.11A and B, respectively. The force map through the carbon ring centers (Figure 5.12C) reveals both hole sites and bond sites. The hole sites exhibit the greatest attractive force, similar to previous experimental studies using other types of tips (see for example Ref. [88]). Note that the force corrugations are also consistent with the lobe features in Figure 5.12B. For example, the force cross section through the surface β atoms (Figure 5.12D) shows two lobes above each atom. The horizontal variation in the forces through the regions resembling the bonding lobes is within one nN.

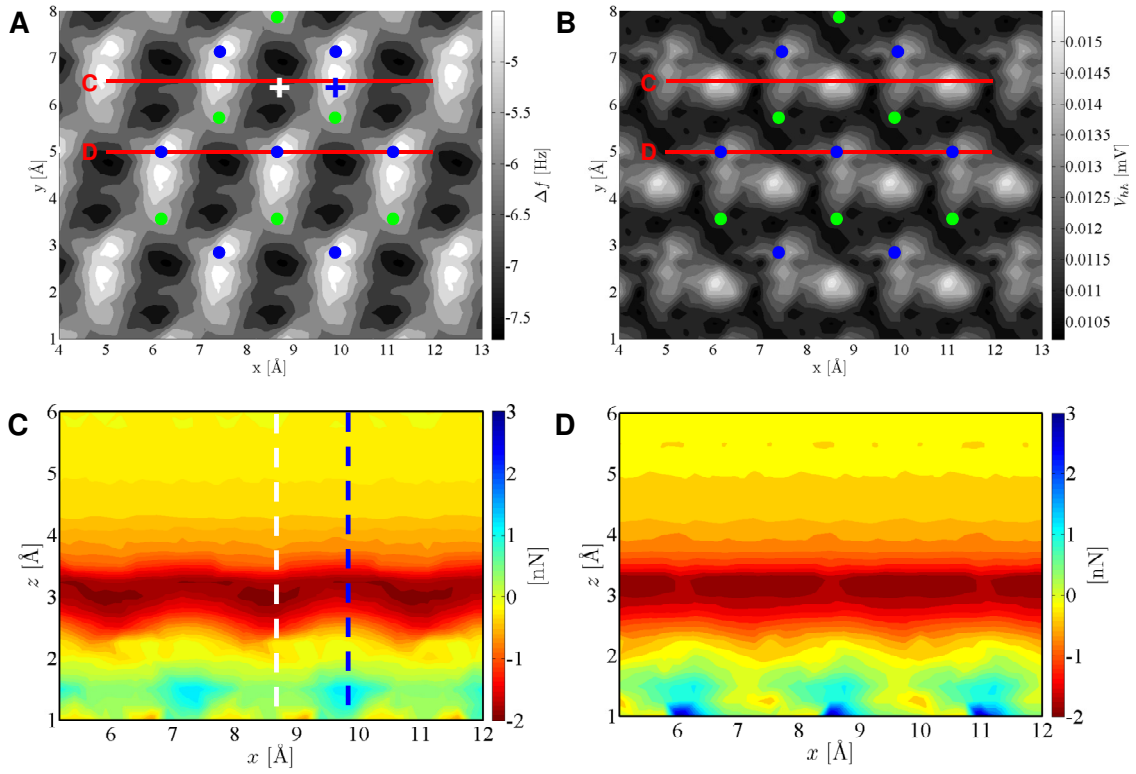

Figure 5.12 – Force cross sections taken relative to (A) the frequency shift and (B) the higher harmonics images of Figure 5.11. The force corrugations through the carbon ring centers (C) reveal both hole sites (white cross and dotted line) and bonds (blue cross and dotted line), with the hole sites exhibiting the maximum attractive force. The force cross section through the surface *β* atoms (D) shows corrugations consistent with the two lobes above each atom.

The similarity between the images in Figures 5.11C and D is a promising result that supports the concept of mapping sub-atomic features via higher harmonics AFM under ideal conditions. However, it is also important to qualify the *meaning* of the observed features. While it is reasonable to view them as the signature of the unpaired bonding lobes of the tip apex, they do not correspond to a static imprint of their shape. This can be realized if one considers that for a fundamental amplitude of 3 Å, the tip oscillation spans a total vertical distance of 6 Å, which is significantly greater than the

size of the bonding lobes. In this case, it may be more proper to qualify the observed features as a dynamic signature representing the convolution of the cantilever dynamics and parameters with the intermittent short-range forces that emerge between the probe and sample orbitals. In fact, our calculations suggest that the observed subatomic features can change shape and even appear or disappear in a non-monotonic fashion as a function of the cantilever height, which is not surprising if one considers the evolution of the lobes at the tip apex as the vertical tip position changes (see Section 4.3). Thus, we cannot yet establish a quantitative connection between the electron density of the probe and sample and the higher harmonics images, even under ideal conditions.

Additionally, there remain other aspects of the method that require further study. First, the effect of the STM bias voltage, which is expected to induce changes in the geometry of the apex lobes by generating attractive forces between the orbitals of the tip and the sample. Second, the filtering procedure that is used to separate the small higher harmonics signals from the fundamental oscillation. (The calculated amplitudes of the first three higher harmonics under the conditions evaluated – specifically zero bias voltage and disregarding the long-range attractive forces – were below 0.01% of the fundamental amplitude, in the range of hundredths of picometers[3].) Finally, the effect of the tip layers directly above the apex atom, whose geometry has a direct effect on the bulk-like nature of the apex atom and which our calculations show affects the size of the lobes (see Section 4.3).

[3] The first three harmonic amplitudes obtained for the force curve shown in Figure 5.10 are only 0.0049, 0.0098, and 0.0052% of the fundamental amplitude, respectively, which when taken as the only three harmonics in the V_{hh} sum (Eqn. 1.3) would correspond to 0.029% of the fundamental amplitude signal, after considering the piezoelectric sensitivity factor (Eqn. 1.4).

5.5. – Conclusions

In summary, we have presented the results of DFT simulations that confirmed the existence of four lobes of increased charge density at the apex atom of a non-bulk W(001) tip, which had previously been observed in quantum mechanics calculations of the W(001) surface [38, 39]. These bonding lobes have been proposed to be responsible for experimentally observed subatomic, four-fold symmetry features produced via higher harmonics AFM imaging [1]. To test the feasibility of this claim, we first developed a method for simulating higher harmonics AFM imaging. Using the method, we showed that it is possible to obtain four-lobed features in a simulated higher harmonics image that are qualitatively similar to those observed experimentally. Important questions not addressed in this work still remain open, such as the challenges involved in filtering and processing sub-picometer higher harmonics amplitudes (discussed in the next chapter) and the effect of the bias voltage in simultaneous AFM/STM imaging, which could have a significant effect on the magnitude of the short-range tip-sample forces and the corresponding harmonics amplitudes. Furthermore, a direct quantitative connection between the images and the probe's electron density cannot yet be established due to the complex, intermittent nature of the tip-sample interaction. We address the question of higher harmonics processing in Chapter 6, and the connection between the images and the system's electron density in Chapter 7.

5.6. – Additional Force Reconstructions

Recall from Section 3.2.2 that the higher harmonics amplitudes are calculated from tip-sample forces via Eqn. 3.15 (reprinted below as Eqn. 5.2). The inversion necessary for force reconstruction is accomplished with Eqns. 5.3 and 5.4.

$$a_n = \frac{2}{\left(1+\delta_{n,0}\right)\pi} \frac{\omega_0^2}{k\left(\omega_0^2 - n^2\omega^2\right)} \int_{-1}^{1} F_{ts}\left(z_0 + a_1 u\right) T_n\left(u\right) \frac{du}{\sqrt{1-u^2}} \tag{5.2}$$

$$F_{ts}\left(z_0 + a_1 u\right) = \sum_{n=0}^{\infty} f_n(z_0, a_1) T_n(u) \tag{5.3}$$

$$\begin{aligned} f_n(z_0, a_1) &= a_n(z_0, a_1) k \left(1 - \frac{n^2\omega^2}{\omega_0^2}\right) \\ &= a_n(z_0, a_1)\left(k - n^2\left(k + k_{ts}^{eff}\right)\right) \end{aligned} \tag{5.4}$$

Figure 5.13 shows the force curve chosen for this exercise (note: this is a reproduction of Figure 5.10B). The base position of the cantilever, z_0, is chosen to be 5 Å and the oscillation amplitude, a_1, is 3 Å, as indicated by the three vertical dotted lines. The calculated harmonics amplitudes are shown in Figure 5.14. Keeping with the experiment, the cantilever resonance frequency was chosen to be f_0 = 18 kHz, and the stiffness k = 1800 N/m.

Figure 5.15A, B, and C illustrate the force reconstruction calculated from Eqn. 5.3 using 3, 6, and 9 harmonics, respectively. The force curve can already be reconstructed accurately using six harmonics. We have therefore chosen to use seven harmonics to

calculate our simulated images (as discussed previously), such that they contain most of the tip-sample force information.

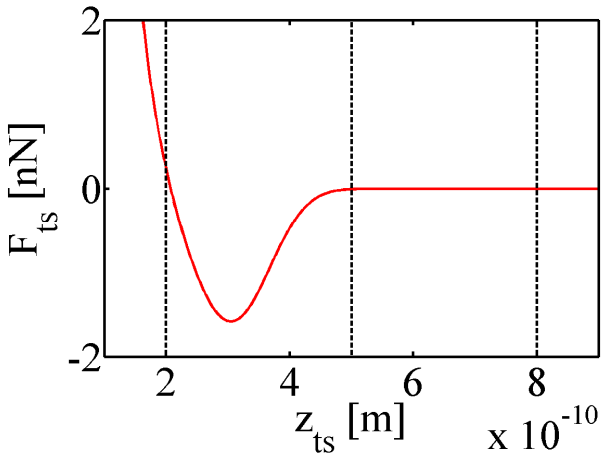

Figure 5.13 – The force curve used for the reconstruction exercise using Dürig's equations. The base position of the cantilever is 5 Å and the fundamental oscillation is 3 Å.

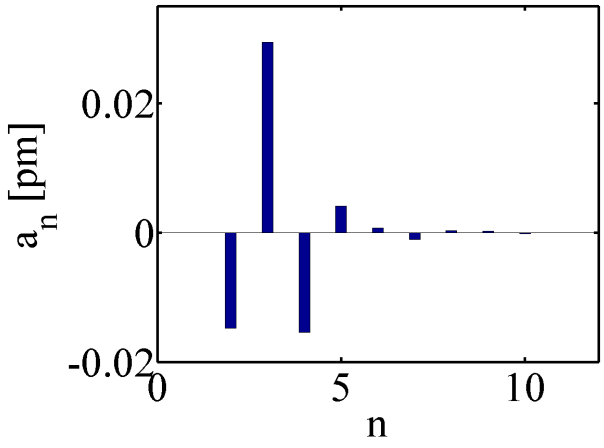

Figure 5.14 – The amplitudes of the higher harmonics for a cantilever oscillating in the tip-sample forces of Figure 5.13, as calculated by Eqn. 5.2. Recall that a_1 is the fundamental amplitude (not shown), so a_2 is the amplitude of the first harmonic, a_3 the second, and so on.

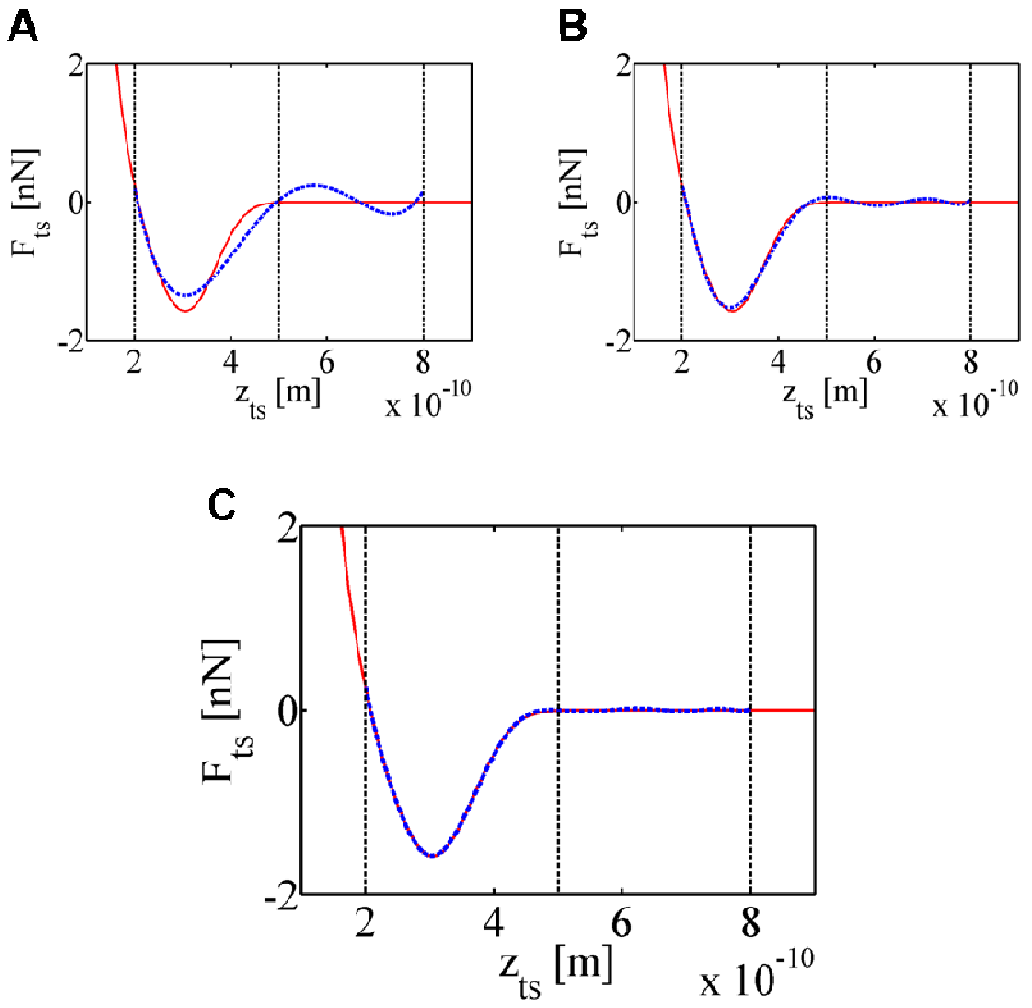

Figure 5.15 – Reconstructing the force curve of Figure 5.13 using (A) 3, (B) 6, and (C) 9 harmonics in the expansion of Eqn. 5.3. The accuracy of the reconstruction is already quite high when 6 harmonics are used.

5.7. – Additional Simulated Images

Figures 5.16A through D show a series of simulated Δf (left column) and V_{hh} (right column) images for a varying distance of closest approach, z_c, for the 9R-S2 system. For A through D, respectively, z_c = 2.50, 2.00, 1.90, and 1.70 Å.

At a closest tip-sample approach of 2.50 Å, the graphite lattice is visible in the frequency shift image, but the harmonics are not sufficient to produce useful contrast. When z_c is reduced to 2 Å, interesting features begin to appear in the higher harmonics image. At z_c = 1.90 Å, the features exhibit a resemblance to the four-fold symmetry of Figure 1.2F that we wish to reproduce. Then when z_c hits 1.70 Å, the frequency shift becomes positive, meaning the tip is probing repulsive forces. Here, both images show the four-fold symmetry features, a finding that coincides with Note 23 in Hembacher *et al*.'s 2004 paper, which states that "the frequency shift data are similar to the higher harmonics data…yet with much less contrast and a substantially smaller signal-to-noise ratio" [1]. Contrary to this statement, the frequency shift image of Figure 5.16D does not appear to have lower contrast. In fact, the contrast seems higher. However, the simulated images are not subject to differences in signal-to-noise ratio, which the authors claim is higher for their experimental higher harmonics images, offering a possible explanation for this discrepancy.

A) z_c **= 2.50 Å**

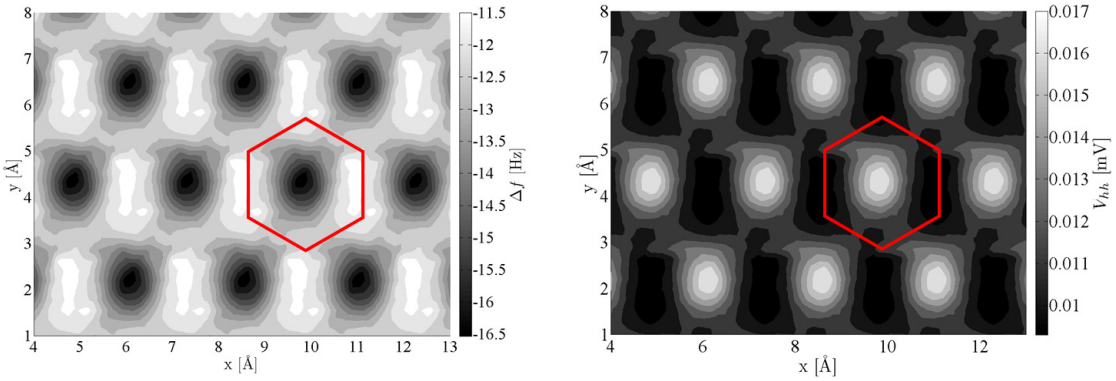

B) z_c **= 2.00 Å**

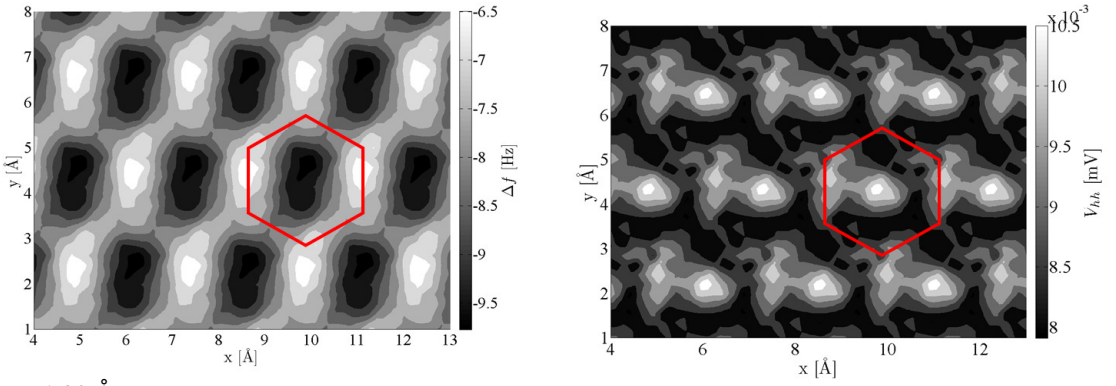

C) z_c **= 1.90 Å**

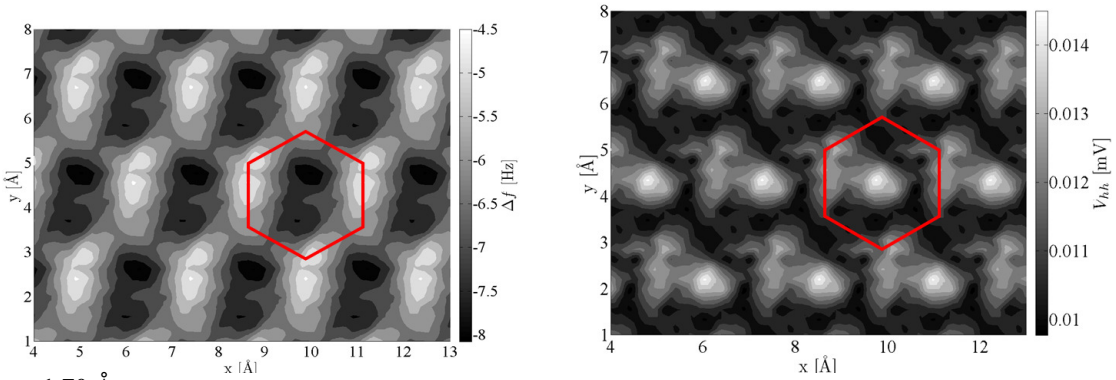

D) z_c **= 1.70 Å**

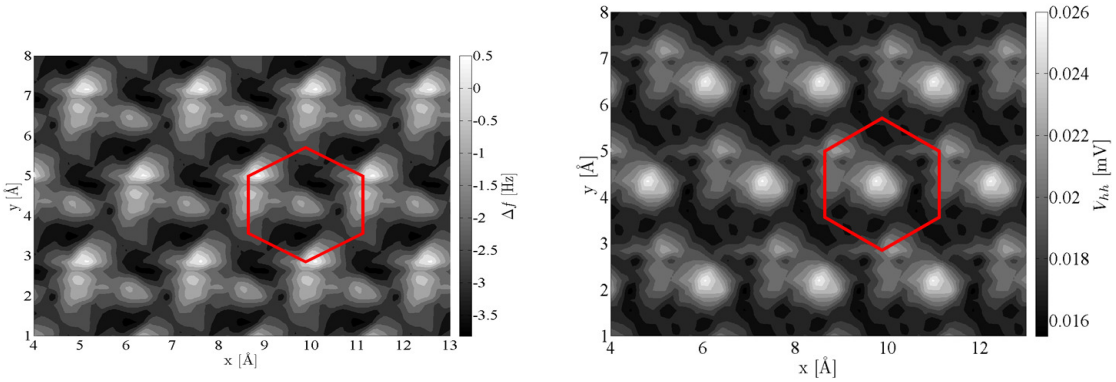

Figure 5.16 – Δf (left) and V_{hh} (right) images as calculated from Dürig's equations for the 9R-S2 system.

Figures 5.17A through D show an analogous series of simulated Δf (left column) and V_{hh} (right column) images for the 9R-Blunt3L system (refer to Section 4.3). Again, for A through D, respectively, z_c = 2.50, 2.00, 1.90, and 1.70 Å.

At a closest tip-sample approach of 2.50 Å, the graphite lattice is discernible in the frequency shift image, though it appears shifted from the true positions of the surface carbon atoms. The higher harmonics image at this distance indicates the periodicity of the graphite lattice, though the image resolution is low. At 2.00 Å, the graphite lattice in the frequency shift image appears more accurate in terms of the true positions of the carbon atoms, and the higher harmonics image seems to offer even higher contrast. Reducing z_c to 1.90 and then 1.70 Å does not produce features similar to the experimentally observed four lobes; however, the higher harmonics images begin to reveal what may be interpreted as a multiplication of the four-fold features produced when imaging the surface with lone-atom-terminated S2 tip. A side-by-side comparison of the higher harmonics images produced by the S2 tip and Blunt3L tip for a closest approach distance of 1.88 Å is shown in Figure 5.18.

A) z_c **= 2.50 Å**

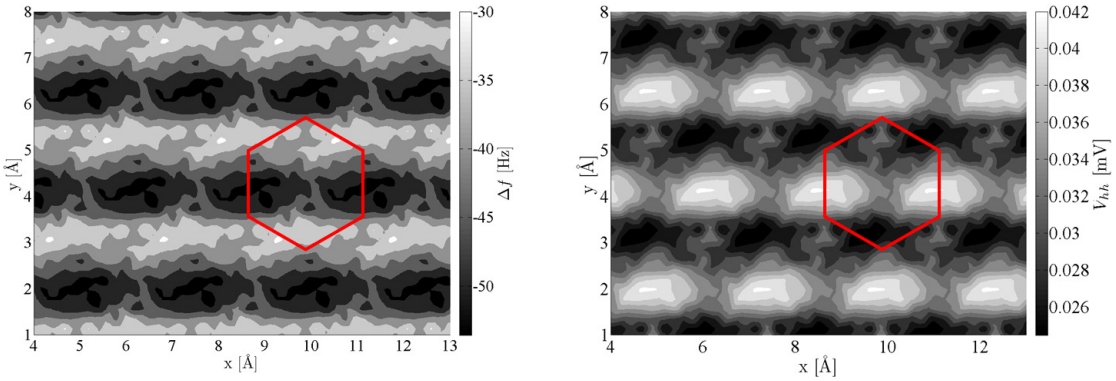

B) z_c **= 2.00 Å**

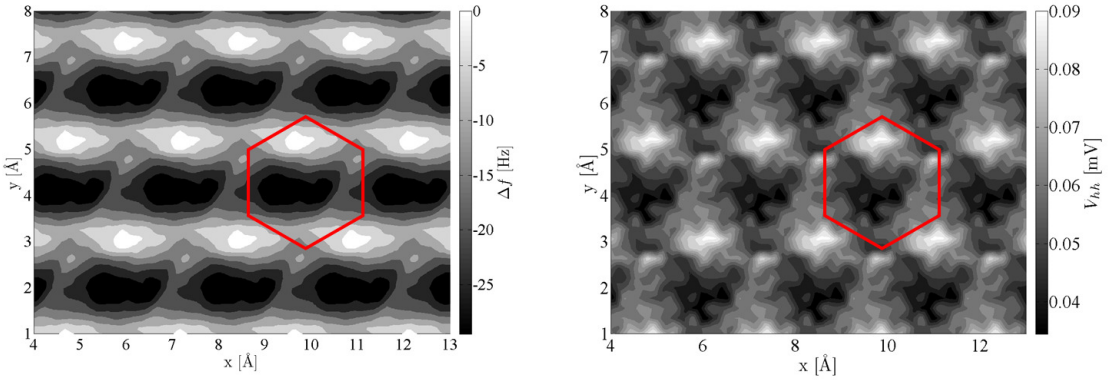

C) z_c **= 1.90 Å**

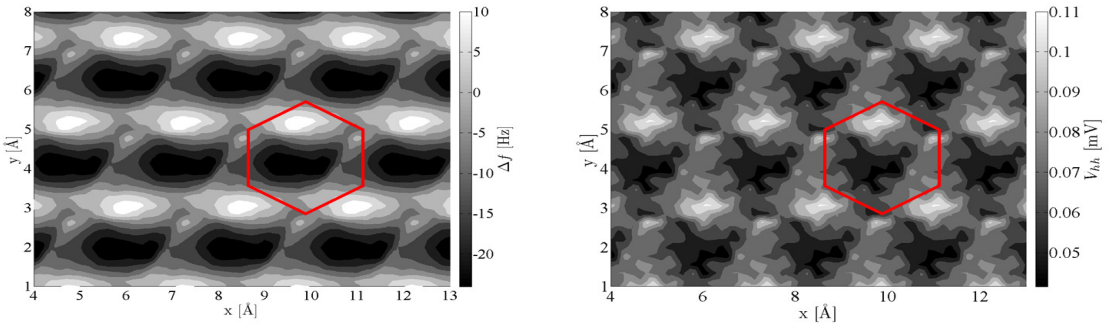

D) z_c **= 1.70 Å**

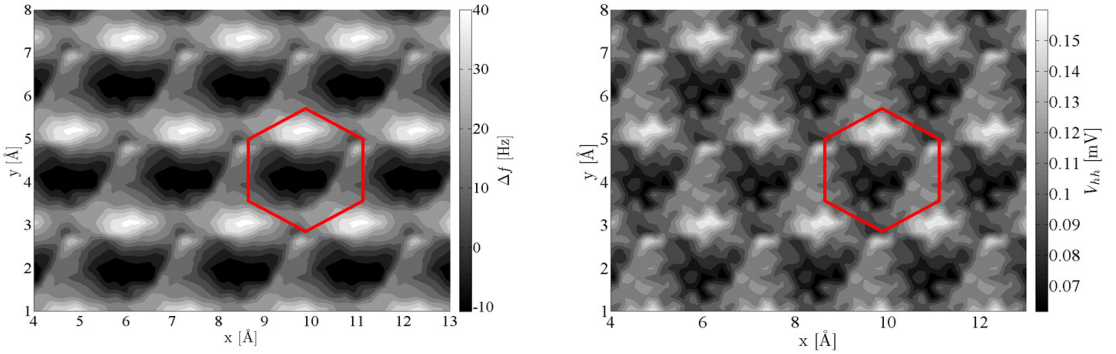

Figure 5.17 – Δf **(left) and** V_{hh} **(right) images calculated from Dürig's theory for the 9R-Blunt3L system.**

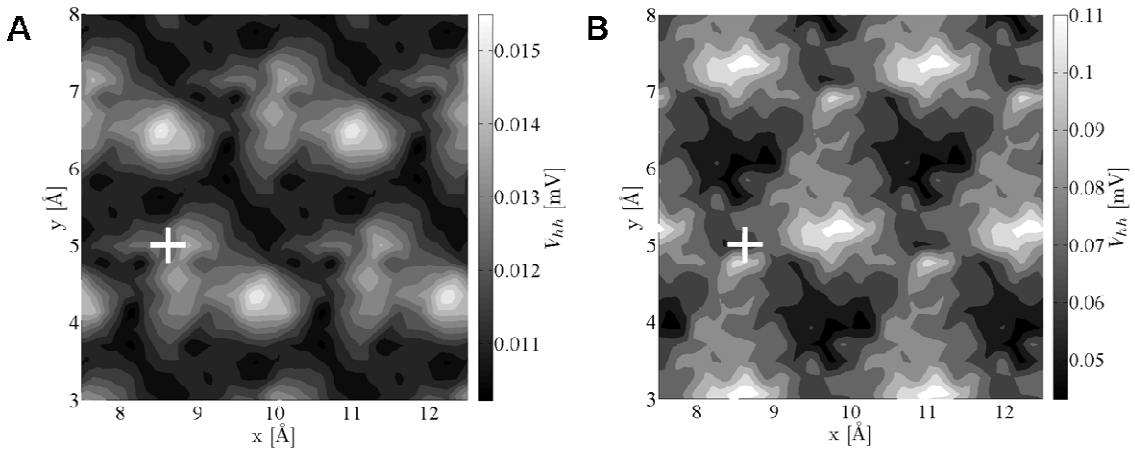

Figure 5.18 – A side-by-side comparison of the higher harmonics images produced by the S2 tip (A) and the Blunt3L tip (B) at a closest approach distance of 1.88 Å.

6. The Effects of Signal Processing

This chapter is an adaptation of the work published in Applied Physics Letters [3]. As in Chapter 5, the overlap with topics discussed earlier in this dissertation has been preserved.

6.1. – Introduction

The ability to image the electron cloud of surfaces at the nanoscale has profound implications for the progress of nanotechnology. The scanning tunneling microscope (STM) has this ability but is limited to conducting surfaces and can only characterize the most loosely bound surface electrons, i.e., those near the Fermi level. Recent experiments using frequency modulation atomic force microscopy (FM-AFM) suggest that this technique might be better suited to probing the *total* electron density at a surface [1, 7, 89]. However, the interpretation of experimentally recorded subatomic features as the signature of the probe tip's electron density has been highly controversial [8, 10, 11, 90]. The most recent experimental report of subatomic imaging is the 2004 work of Hembacher *et al.* [1], in which a tungsten tip attached to a qPlus sensor [6] was used to characterize a graphite surface using simultaneous STM/FM-AFM. Features of subatomic size were observed in the maps of the quartz "cantilever's" higher harmonics and were

interpreted as the footprint of electron bonding lobes at the apex atom of the tungsten tip [1]. Figure 6.1 (adapted from Figure 1.2) shows one set of simultaneously acquired maps of tunneling current and higher harmonics voltage. The four-fold features in the higher harmonics image are attributed to the bonding symmetry of a W(001) tip apex atom, as indicated by the Wigner-Seitz cell for body-centered cubic W(001) (Figure 6.1C). While it is true that individual higher harmonics in dynamic AFM can provide increased spatial resolution, the authors' interpretation of the experimental higher harmonics images has been met with much scrutiny, primarily due to the experimental methods used to process the harmonics [1, 2].

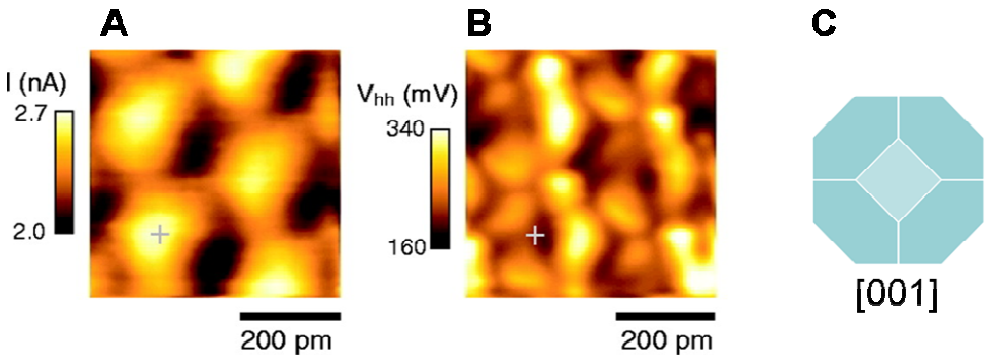

Figure 6.1 – Simultaneously acquired tunneling current (A) and higher harmonics voltage (B) from the experiment of Hembacher *et al.* (adapted from Figure 1.2). The features of subatomic size in the higher harmonics image (B) were interpreted as the signature of bonding lobes of increased charge density at the apex atom of a [001] oriented tungsten tip. The Wigner-Seitz cell (C) for body-centered cubic W(001) exhibits the same four-fold symmetry observed in the features in (B).

It is well known that the response spectrum of a sinusoidally driven, nonlinear oscillator will contain harmonic components. In the case of dynamic AFM, it has been shown that the higher harmonics in the cantilever oscillation contain detailed information

about the tip-sample interaction [28, 30, 32, 91-97]. This result has led to experimental methods to reconstruct tip-sample forces from measured harmonics, as well as research aimed at determining if material properties can be extracted from them, and how they can be utilized to improve imaging resolution. The harmonics in tapping mode AFM operation have been related to the mechanical stiffness of the sample [97], and various researchers have demonstrated material-specific contrast by mapping a specific harmonic [93, 94].

Expanding on previous work by Dürig on force reconstruction in FM-AFM [28, 29, 32], Hembacher *et al.* derived an expression relating the *n*th higher harmonic to a convolution of the *n*th gradient of the tip-sample force curve, F_{ts}, with a bell-shaped weight function [1, 2, 33],

$$a_n = \frac{2}{\pi k}\frac{1}{1-n^2}\frac{A^n}{1\cdot 3\cdot 5\cdot \ldots \cdot (2n-1)} \times \int_{-1}^{1} \frac{d^n F_{ts}(z_0 + a_1 u)}{dz^n}\left(1-u^2\right)^{n-1/2} du \,. \qquad (6.1)$$

where a_n is the amplitude of the *n*th harmonic, k is the cantilever stiffness, and z_0 is the cantilever equilibrium position. Because atomic resolution generally requires the isolation of the short-range component of the tip-sample force [12, 13], this mathematical relationship implies that higher harmonics in noncontact AFM should offer increased spatial resolution. This is because that for attractive forces in noncontact AFM – which are generally monotonic and typically proportional to $1/z^n$ – higher gradients of F_{ts} will exhibit steeper distance dependence; thus, contributions to the higher harmonics should come primarily from the front-most tip atom(s) [1]. It is important to note that while this is valid for attractive forces, it is not true in general.

In Chapter 5, we introduced a method for simulating higher harmonics imaging as a means to investigate the fundamental feasibility of subatomic imaging and its relationship to probing electron density. Briefly, the method involves the use of density functional theory (DFT) to calculate the tip-sample forces over a 3-dimensional grid composed of 2100 different tip positions above the surface, an in-depth curve fitting process, and the theory of Dürig [32] to calculate the theoretical harmonics amplitudes, from which the images can be constructed. The surface and tip models used for the DFT simulations are shown in Figure 5.1, but are reprinted for convenience as Figure 6.2 (note also that the new color coding of Figure 6.2 corresponds to the results of this chapter). The model surface of graphite (Figure 6.2A) consisted of a nine-carbon-ring top layer and a four-carbon-ring second layer, which has been excluded from the figure for clarity. Each layer was edge-terminated with either oxygen (blue) or hydrogen (yellow) atoms depending on which type was needed to maintain the sp^2 hybridization of the carbon atoms. The circles above the surface indicate the (x, y) grid points for which tip-sample force curves ($F_{ts}(z)$) were calculated (the solid, colored circles are related to Figures 6.5 and 6.10 and will be discussed in a later section). Details of the DFT calculations can be found in Chapters 4 and 5.

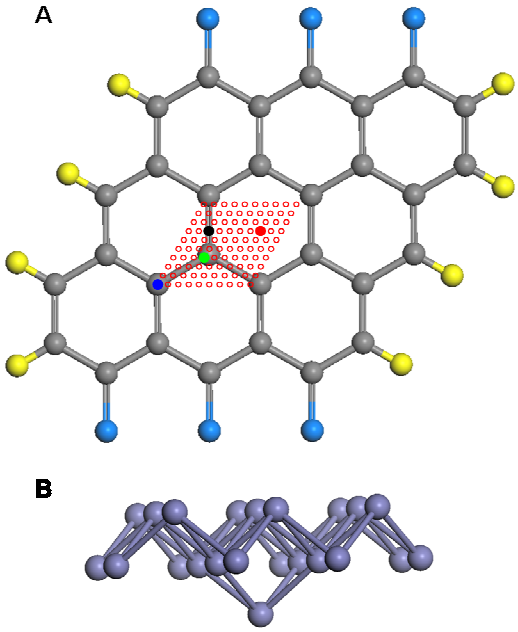

Figure 6.2 – Density functional theory (DFT) calculations form the initial step in simulating the higher harmonics images of Hembacher *et al*. (A) The top layer of the surface model used to approximate graphite and (B) the three-layer W(001) tip model used in the DFT simulations. A tip-sample approach was performed over each of the circles in (A). The filled green, red, blue, and black circles mark the locations where harmonics amplitude ratios were calculated for the construction of Figure 6.5, as well as the locations of the force curves shown in Figure 6.10. Details of the DFT simulations can be found in Chapters 4 and 5.

We previously emphasized that four important features of the 2004 experiment must be considered in a full theoretical treatment of the problem: (1) the crystallographic plane of tungsten responsible for image contrast and the presence of bulk-like surface states in a non-bulk system such as an AFM tip, (2) the effect of simultaneous STM/AFM on the electronic states of the system, (3) the cantilever dynamics, and (4) the effect of filtering and processing the cantilever trajectory. In Chapter 5, we addressed only the first of the four, though we were able to reproduce subatomic features *qualitatively* similar to

those seen experimentally for the tungsten tip with four-fold bonding symmetry at the apex (see Figure 5.11). Here we expand on this work by investigating the effects of signal processing on the higher harmonics images. We again idealize the cantilever dynamics and do not yet consider the effect of simultaneous STM/AFM in order to continue our bottom-up theoretical development from the most ideal (noise-free) imaging scenario.

6.2. – Relevant Experimental Background

In their 2004 experiment, Hembacher *et al.* did not measure the amplitudes of the higher harmonics individually [1]. Instead, the qPlus trajectory signal was fed into a programmable eight-pole elliptic high-pass filter (Stanford Research Systems SR650 [35]) to eliminate the fundamental frequency component and calculate the root-mean-square (rms) of the harmonics amplitudes, followed by an rms-to-dc converter. The higher harmonics images produced were voltage maps representing the rms sum of all higher harmonics [1, 33]. This processing step has been one of the most significant points of contention regarding the interpretation of their images as maps of the tip apex atom's charge density.

The motivation for filtering the cantilever trajectory and taking an rms of the harmonics amplitudes was to enhance the harmonics signal. In contrast to large amplitude tapping mode AFM methods of harmonic imaging [30], Hembacher *et al.* performed small amplitude (A_{osc} = 3 Å) STM/FM-AFM. Oscillation amplitudes on the order of the interaction potential have been demonstrated (using theory) to provide optimum signal-to-noise ratio (SNR) and enhanced sensitivity to short-range forces [20]. However, for

angstrom-scale fundamental oscillations, the amplitudes of even the low-order harmonics are typically sub-picometer and therefore need to be enhanced in order for their measurement to be practical. Nevertheless, the measurement of higher harmonics in the small amplitude limit is desirable because the tip interacts with the surface force field for most (if not all) of the oscillation cycle. Dürig has shown that under this condition, the lower-order harmonics contain enough information to reconstruct the short-range tip-sample force over the range of the oscillation [32]. The increased information content of the lower order harmonics is a significant advantage with respect to large amplitude tapping mode experiments, which can require the measurement of anywhere from tens to hundreds of harmonics to *accurately* reproduce tip-sample force curves, especially near the location of the maximum attractive force [98].

With regard to enhancement, it has been found experimentally that the higher harmonics occurring near a cantilever's flexural eigenmodes are amplified by the excitation of the latter during tip-sample interaction [93]. This result has been exploited by developing cantilevers with a flexural eigenmode that is nearly an exact multiple of the fundamental resonance, thereby providing the maximum enhancement of the harmonic occurring at that frequency [96, 97]. While such cantilevers offer significant advantages in tapping mode higher harmonics AFM, their deflection must still be measured by optical means, which makes them impractical for the measurement of sub-picometer harmonics amplitudes, particularly for low-temperature, ultrahigh vacuum (UHV) AFM. The same is true for torsional harmonic cantilevers [30], whose increased sensitivity is derived from the fact that the photodetector signal is directly proportional to the slope of the cantilever. The torsional paddle experiences relatively large angular

deflections even for small vertical displacements, so harmonics that are small in amplitude can be measured with high signal strength.

Because the specialized cantilevers described above are impractical for the measurement of subpicomenter harmonics amplitudes in UHV, other means of enhancement must be implemented. To this end, Hembacher *et al.* leveraged the piezoelectric properties of quartz. The qPlus sensor also offered the added benefit of enabling simultaneous STM/FM-AFM. In contrast to optical detection schemes, which produce a signal that is proportional to deflection, piezoelectric detectors such as the qPlus sensor generate a current that is proportional to both deflection *and* frequency, thus providing built-in amplification of the harmonics. Hembacher's approach of filtering and collecting an rms sum of all higher harmonics was meant to *supplement* this increased sensitivity, as the output voltage obtained by using all the harmonics amplitudes provides higher signal strength than that of individual harmonics. The rms voltage signal produced from the higher harmonics is given by

$$V_{hh} = \left(\sum_{2}^{\infty} \left(S_n a_n \right)^2 \right)^{1/2} \tag{6.2}$$

where S_n is the sensitivity of the deflection sensor for the n^{th} harmonic,

$$S_n \approx \frac{n}{\left(1 + 0.0767 n^2\right)^{1/2}} \times 0.1 \text{ mV/pm} \tag{6.3}$$

(These are reprints of Eqns. 1.3 and 1.4, respectively.) Note that a_2 is the amplitude of the first harmonic above the fundamental. The sensitivity, S_n, is given by the product of the

current per deflection generated by the qPlus sensor multiplied by the current-to-voltage conversion rate of the preamplifier [1, 33]. Eqn. 6.3 is plotted in Figure 6.3, which demonstrates how the sensitivity plateaus with increasing harmonic number. Plotted in Figure 6.4 are the amplitudes of the higher harmonics directly above a β atom of the model surface (indicated by a solid blue circle in Figure 6.2), as well as the voltages that result from multiplying each by the corresponding qPlus sensitivity value.

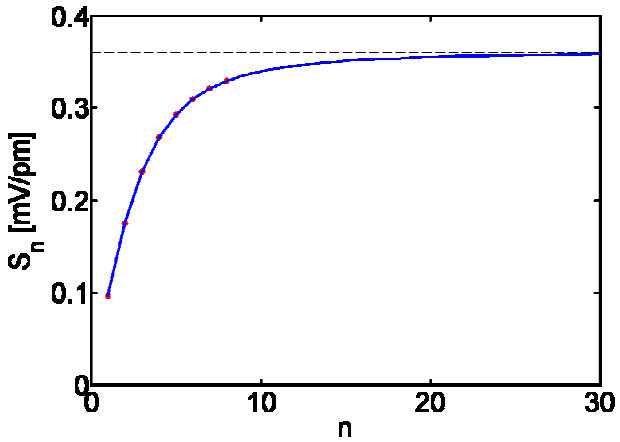

Figure 6.3 – Sensitivity [mV/pm] of the qPlus sensor to harmonic *n* (*n*=1 corresponds to the fundamental oscillation frequency). The sensitivity drops off and plateaus by approximately the 9th harmonic (n=10).

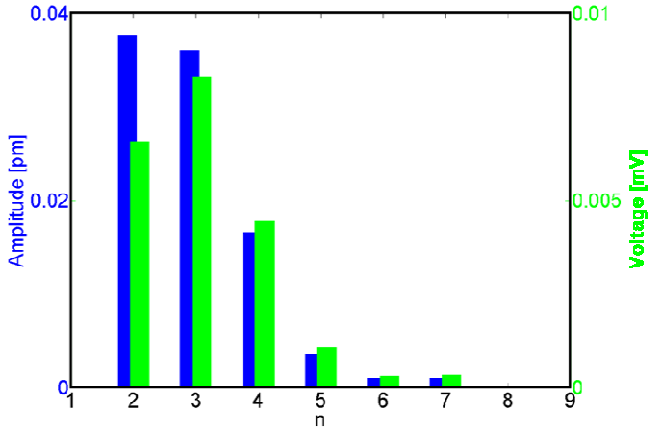

Figure 6.4 – Amplitudes (a_n) and voltages (a_n*S_n) directly above a β atom of the model surface (indicated by a solid blue circle in Figure 6.2).

While the motivation for the experimental rms approach is clear, the justification for its validity needs to be explored in the context of the actual shape of the tip-sample force curves. We will consider the filtering and rms processing separately, beginning with the latter for reasons that will become apparent.

6.3. – Root-Mean-Square Harmonics Collection

Giessibl conducted simulations of a simple electrostatic model (composed of ten *point charges*) for the tip-sample interaction, for which the amplitudes of *individual* higher harmonics produced *qualitatively* similar images [33, 97]. Thus it was assumed that mapping the rms sum of *all* higher harmonics would not change the nature of the resultant image and would increase the SNR [1, 33]. Although the intent was not to reconstruct force curves, it is important to recall that an rms sum of the harmonics is not capable of recovering F_{ts} in real time, which requires measuring the amplitudes and

phases of individual harmonics in order to apply the appropriate inversion procedure [32, 33].

The information content of the harmonics in dynamic AFM becomes clear from a mathematical treatment of the oscillating tip in the presence of nonlinear interaction forces. The periodic excitation of the cantilever means that under steady-state conditions, the tip-sample forces are also periodic in time, which enables them to be expressed mathematically as a Fourier series [92] or Chebyshev series (see Section 3.2.2) [28, 32]. In Dürig's treatment [32], which is the basis of Hembacher's interpretation (see Eqn. 6.1) [1], the higher harmonics amplitudes form the series coefficients (which can be positive or negative). Thus, measuring the harmonics allows one to directly reconstruct F_{ts} using the appropriate series expansion [1, 2, 28, 32, 33]. Further, as discussed above, the relationship between the harmonics and the higher gradients of the tip-sample force implies that – for a conservative potential that is monotonically attractive – mapping individual higher harmonics should result in higher spatial resolution. (The highest measurable harmonic should theoretically have the steepest distance dependence and thus provide the highest resolution of short-range forces.) Higher harmonics have also been shown to provide high resolution material-specific contrast for tapping mode cases where repulsive or dissipative forces are involved [93, 94], although the contrast mechanism differs from that of the attractive regime case.

The reconstruction of F_{ts} from a series summation involving multiple harmonics and the mapping of single harmonics for high resolution are both valid experimental approaches. However, an issue arises when mixing the two methods by mapping an rms sum of higher harmonics for increased spatial resolution. This hybrid method can be

problematic because the individual harmonics depend on the *exact* shape of the interaction potential. The relevant consequence is that the amplitudes of the harmonics do not maintain set ratios across different surface sites. Figure 6.5 shows the amplitude ratios 1:2, 1:3, and 2:3 of the theoretical harmonics over a surface α atom, β atom, hole site, and bond for the model tip-sample system shown in Figure 6.2, demonstrating how the ratios change for each surface site. (Note that harmonic 1 is the first harmonic above the fundamental, i.e., has frequency $2f_0$.) An rms sum of the harmonics at a given position is a statistical measure and therefore does not retain the detailed information encoded into each harmonic. As the difference in ratios implies, increases and decreases in the amplitudes of specific harmonics are not consistent across the surface, and averaging the amplitudes at each surface site cannot capture these changes. Furthermore, such averaging can at least partially eliminate the contrast if the changes in the harmonics amplitudes show inverse correlations to one another. Thus, an image composed of averaged harmonics amplitudes (the rms voltage) cannot be seen as an accurate representation of the surface structure or material properties. Finally, because the ratios shown in Figure 6.5 are for amplitudes calculated from the fundamental theory of Dürig, one can conclude that this phenomenon is independent of the experimental technique used to capture the harmonics.

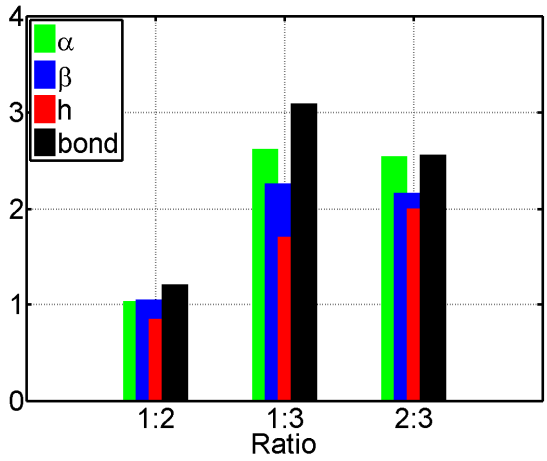

Figure 6.5 – Amplitude ratios 1:2, 1:3, and 2:3 of the theoretical harmonics (note that harmonic 1 is the first harmonic above the fundamental, i.e., has frequency $2f_0$) over a surface *α* atom, *β* atom, hole site, and bond for the model tip-sample system shown in Figure 6.2 for a closest tip-sample approach distance of 1.90 Å and an oscillation amplitude of 3 Å, demonstrating how the ratios change for different surface sites.

The averaging effects of an rms would also be problematic in large amplitude tapping mode AFM. In Ref. [94], Stark and Heckl performed a series of experimental tapping mode images of a Pt-C film on silica. Separate images were created using the third, fifth, and eighth harmonics of the drive frequency (see Figure 6.6). The relevant result is the contrast inversion observed in the image created with the fifth harmonic relative to those created with the third and eighth harmonics. In this specific case, if one were to create an image using an rms sum of these three higher harmonics, the contrast that appears in each individual image would be greatly diminished. While the contrast in an averaged image will not always be lower than that in individual harmonics images, the former will always be artificial. With this in mind, before discussing the effects of

filtering, we will look at simulations for the specific case of Hembacher's 2004 experiment.

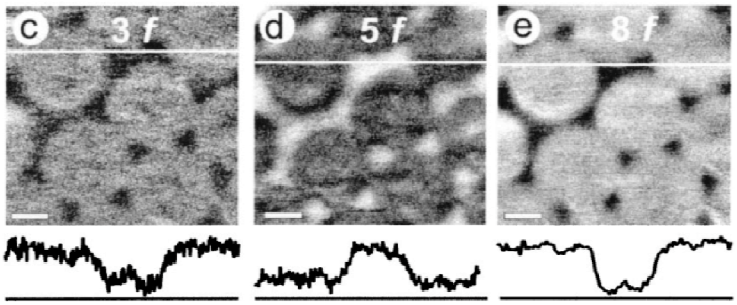

Figure 6.6 – Experimental 3rd, 5th, and 8th harmonics of a 4-nm-thick platinum-carbon test structure on a fused silica coverslip. The contrast inversion between individual harmonics means that the contrast in an rms sum image would be greatly diminished. (Adapted from Figure 2 in Ref. [94]).

6.4. – Simulated Images

Using the method and model system (see Figure 6.2) described in Chapter 5, we can easily simulate images produced with individual higher harmonics. Shown in Figure 6.7 are images created from each of the first four harmonics individually, as well as the image created by their rms sum (see Eqn. 6.2). Figure 6.8 shows the images created using the 5th, 6th, and 7th harmonics, as well as the rms sum of harmonics 1-7. All the images shown are constant-height voltage maps (i.e., each harmonic amplitude has been multiplied by the piezoelectric sensitivity of the qPlus sensor corresponding to that frequency (Eqn. 6.3)) for a 3 Å oscillation and a closest tip-sample distance of 1.90 Å. The positions of the surface carbon atoms are indicated by red hexagons. The partial "frame" observed on the border of the unit cell, evident in the images of the 3rd, 4th and

especially the 5th harmonics, is an artifact caused by the use of a non-periodic system (Figure 6.2A) in the construction of the tip-sample force curves.

While the images created using the 1st and 2nd harmonics exhibit four-fold features (indicated with dotted red ovals) qualitatively similar to the experimental image shown in Figure 6.1B, the features do not get sharper with increasing harmonic number as one would expect based on the steeper-distance-dependence argument of Hembacher *et al*. In fact, not only do the four-fold features appear diminished in the 2nd harmonic image, they do not appear at all in the 3rd and 4th harmonics images. This lack of qualitative similarity conflicts with the justification presented in Refs. [33, 97] (and discussed previously) for collecting an rms sum as a means to enhance signal strength without compromising the nature of the resultant image.

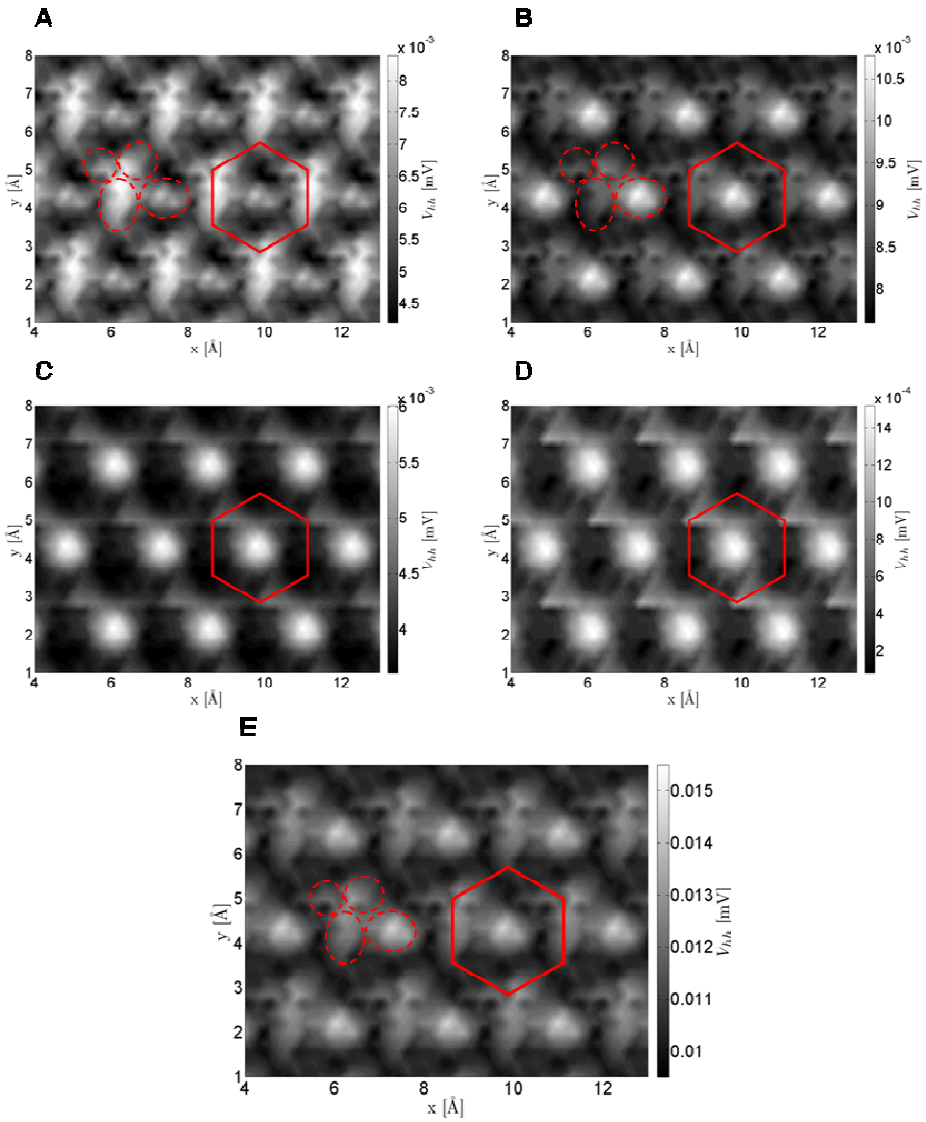

Figure 6.7 – Simulated V_{hh} images for the model system of Figure 6.2 created from the (A) 1st harmonic, (B) 2nd harmonic, (C) 3rd harmonic, (D) 4th harmonic, and (E) rms sum of the 1st – 4th harmonics. The closest tip-sample approach distance is 1.90 Å. The positions of the surface carbon atoms are indicated in each image by a red hexagon. Notice that the contour scaling is different in each image and that the voltage values in the 4th harmonic image have dropped by nearly an order of magnitude relative to the 1st and 2nd harmonic images. Consequently, the features in the rms sum image are dominated by the first two harmonics.

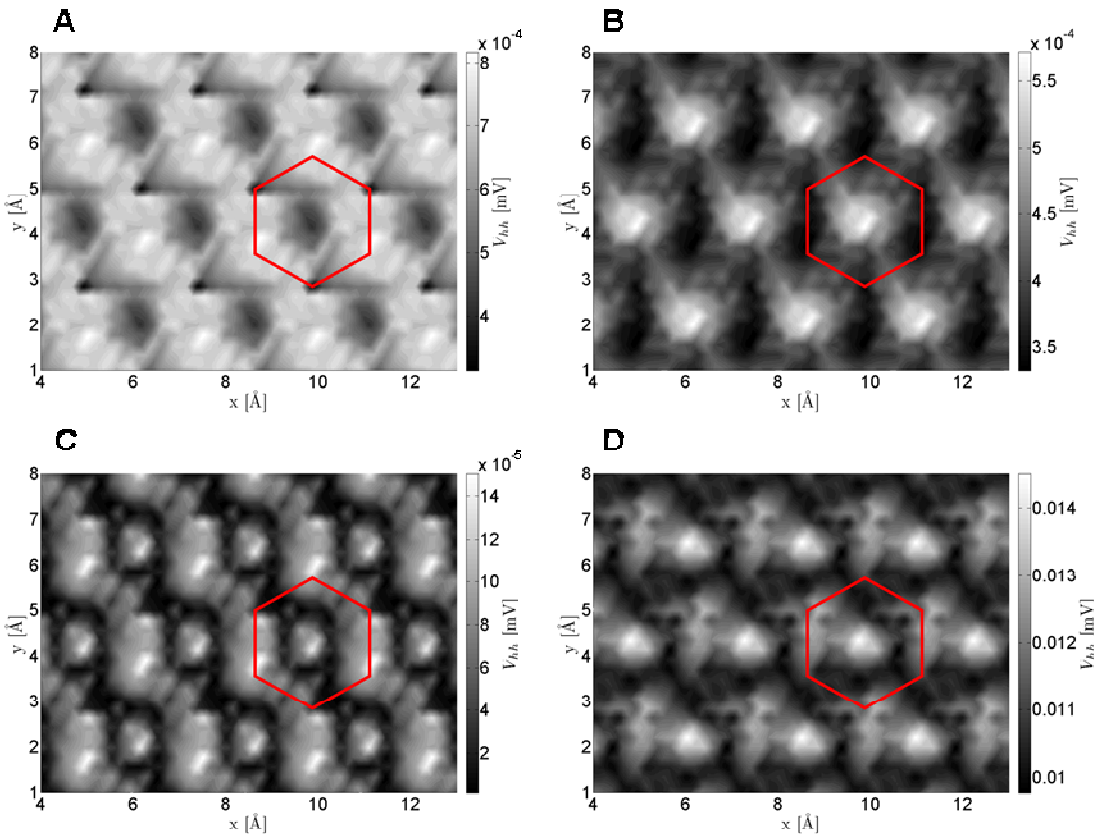

Figure 6.8 – Simulated V_{hh} images created using the (A) 5th, (B) 6th, and (C) 7th harmonics, as well as (D) the rms sum of harmonics 1-7.

The root of this conflict lies in the simple nature of the electrostatic model used for justification [33, 97]. First, while the orientation of the point charges in the simple model approximately reflects the charge distribution of a surface W(001) atom [38, 39, 85], the charges themselves are *fixed in space*, so they cannot reflect the dynamic response of real electron orbitals during the oscillatory tip-sample interaction. Shown in Figure 6.9 are cross sections of the change in electron density directly below the apex atom of the tungsten tip as calculated by DFT (viewed from above; see Figure 6.9A). The tip-surface distance for all cases is 2 Å, and the (x, y) position of the apex atom relative to a β carbon atom of the surface is indicated with a red X in the inset of each panel. The

direction of each of the three carbon-carbon bonds is also shown. Clearly, the four bonding lobes of increased electron density are affected by the lateral position of the tip relative to the surface.

Second, and more important to the validity of the justification, the $1/z^2$ dependence of the Coulombic force between point charges guarantees that the higher gradients of the force will have the steeper distance dependence necessary for increased spatial resolution with increasing harmonic number. The closest approach distance for the simple electrostatic model images presented in Ref. [33] is 1.32 Å. Recalling that the images in Figures 6.7 and 6.8 are for a closest tip-sample distance of 1.90 Å, we see from Figure 6.10 that the DFT tip-sample force curves over the corresponding oscillation range do not satisfy the $\sim 1/z^n$ requirement necessary for increasing harmonics to exhibit steeper distance dependence.

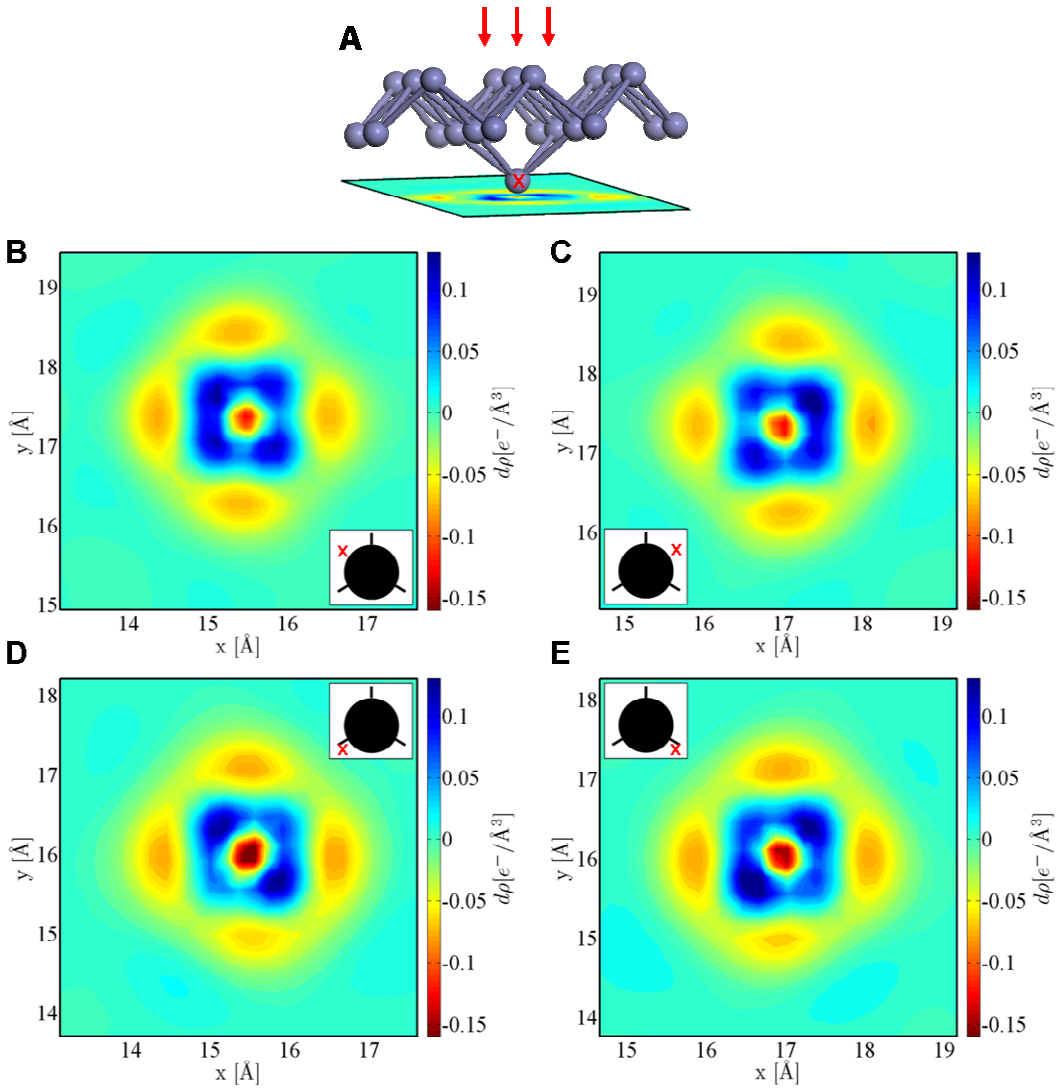

Figure 6.9 – Cross sections (viewed from above) of the DFT-calculated change in electron density directly below the apex atom of the tungsten tip, demonstrating that the four bonding lobes of increased electron density are affected by the lateral position of the tip relative to the surface. The tip-sample distance for all cases is 2 Å, and the (*x*, *y*) position of the apex atom relative to a *β* carbon atom of the surface is indicated with a red X in the inset of each panel. The X is approximately located at the border of the C atom in all cases. The direction of each of the three carbon-carbon bonds is also shown.

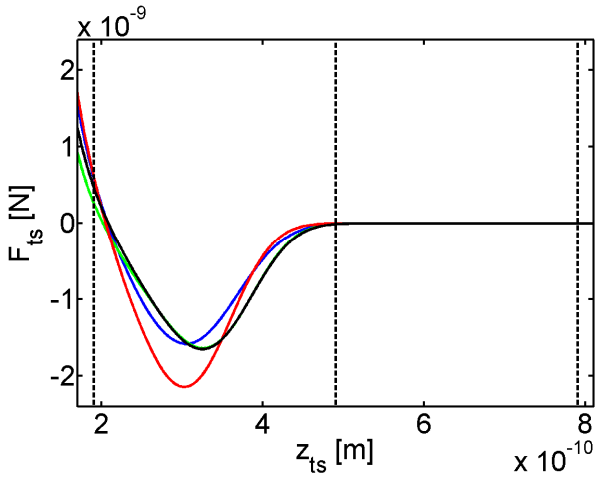

Figure 6.10 – Representative tip-sample force curves for the four surface sites indicated in Figure 6.2A. Clearly they do not exhibit ~1/z^2 behavior over the range of oscillation, which is indicated by the dashed vertical lines.

Although the above results do not support the use of an rms sum of harmonics to increase short-range force resolution, there is still a promising aspect to them. Note that the contour scaling is different in each image of Figures 6.7 and 6.8 and that the voltage values in the 4th harmonic image have dropped by nearly an order of magnitude relative to the 1st and 2nd harmonics images. Even though the qPlus sensitivity increases with increasing harmonic number, the amplitudes of the harmonics drop off too quickly for the sensitivity increase to compensate. Consequently, the qualitative features in the rms sum image are dominated by the first two harmonics which, when plotted individually, reveal four-fold features similar to the experiment. Since we have not yet simulated the filter, the four-fold features seen in Figure 6.7A and B cannot be merely artifacts. This result suggests that one could use a single lock-in amplifier to collect either the first or second harmonic and potentially reproduce the subatomic contrast of Hembacher *et al*. under the

right experimental conditions (e.g., ideal tip structure), provided the noise level is sufficiently low.

6.5. – Filtering

We now turn to the filtering, which has been at the center of the controversy. Recall that Hembacher *et al*. used the programmable SR650 to collect the rms sum of harmonics *after* high-pass filtering the trajectory to remove the fundamental frequency component [1]. While the magnitude response of a filter changes with input frequency, the filtering process should not change the qualitative nature of images created using the magnitude of an *individual* harmonic. The filter gain (at the specific harmonic frequency) will simply scale the quantitative value measured at each pixel of the image. Indeed, this is what we see in our simulations. Figure 6.11 shows simulated unfiltered (left column) and filtered (right column) images created using the individual harmonics indicated, supporting this notion. Matlab's `ellip` function was used to simulate the filter used in Hembacher's experiment, i.e., an 8^{th} order elliptic high-pass filter with a 20 kHz cutoff frequency.

Figure 6.11 – (Next page) Simulated unfiltered (left column) and filtered (right column) images created using the individual harmonics indicated, demonstrating that filtering has a negligible effect on the qualitative nature of the images. A slight change in the contour scaling occurs due to the gain of the filter.

Unfiltered **Filtered**

A) 1st harmonic

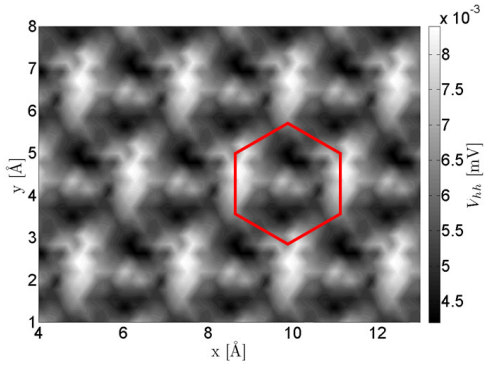

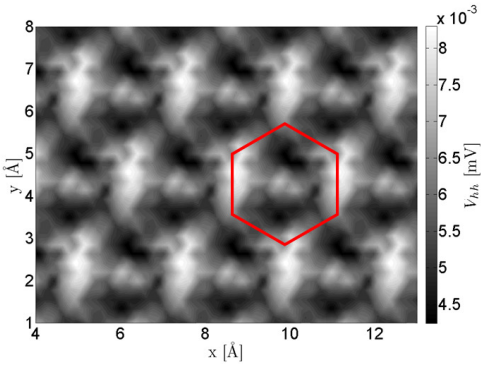

B) 2nd harmonic

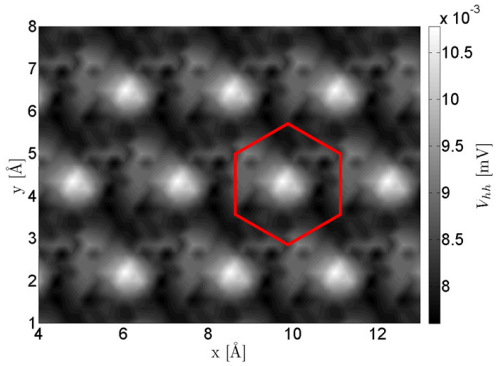

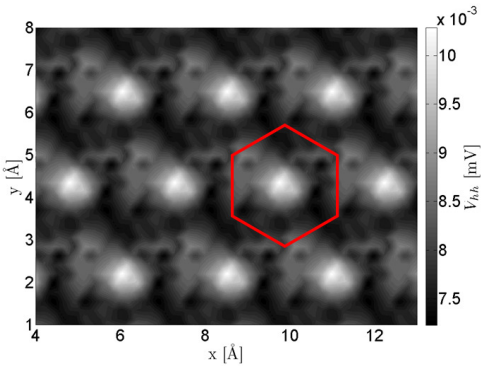

C) 3rd harmonic

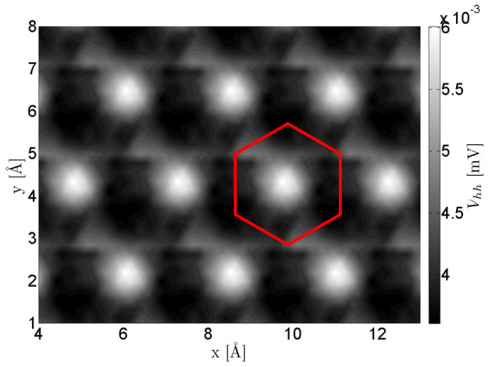

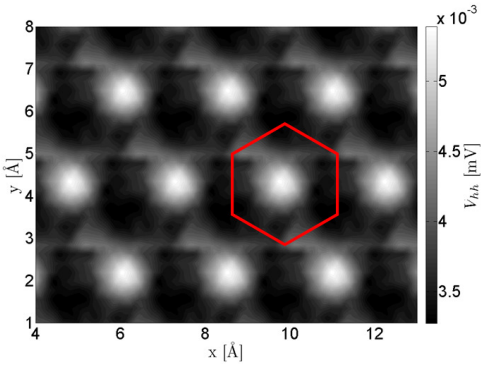

D) 4th harmonic

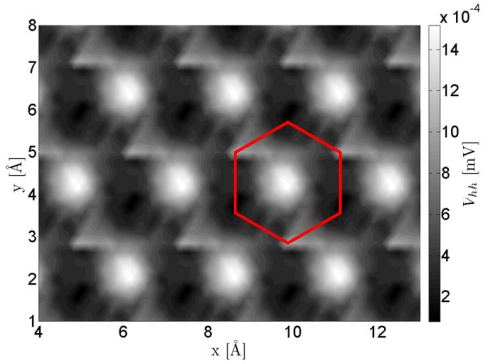

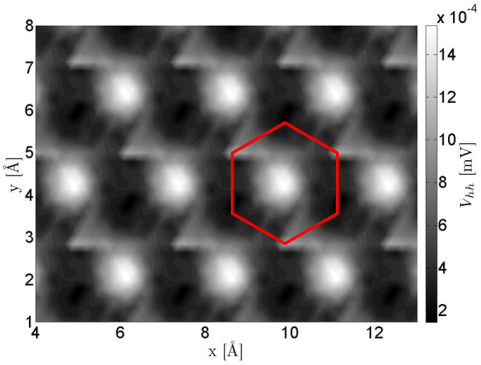

Ultimately, however, the question of filtering must be investigated in the context of the experiment of Hembacher *et al*. in order to determine whether their images contain artifacts as an inherent result of the filtering process. When considering the effects of filtering a trajectory that will be used to construct an rms sum, we note that the qualitative nature of the image could theoretically change due to the varying magnitude response of the filter. The filter cutoff, order, and type may attenuate/enhance different harmonics by different amounts, thereby affecting their average value at each pixel. However, our simulations indicate that the filter used by Hembacher *et al.* has a negligible effect on the resultant rms image. Figure 6.12 shows images created from an rms sum of the first four harmonics both before (A) and after (B) filtering. The closest tip-sample approach is again 1.90 Å (Figure 6.12A is a reproduction of Figure 6.7E meant to offer a convenient side-by-side comparison). Note that the contour scaling is equivalent between the two images. The qualitative difference is minimal, although the filtered image does seem to eliminate the smaller features occurring between the larger four-fold features. Figure 6.12C illustrates the *quantitative* difference values between the images (unfiltered minus filtered), which are on the order of 5% of the maximum V_{hh}.

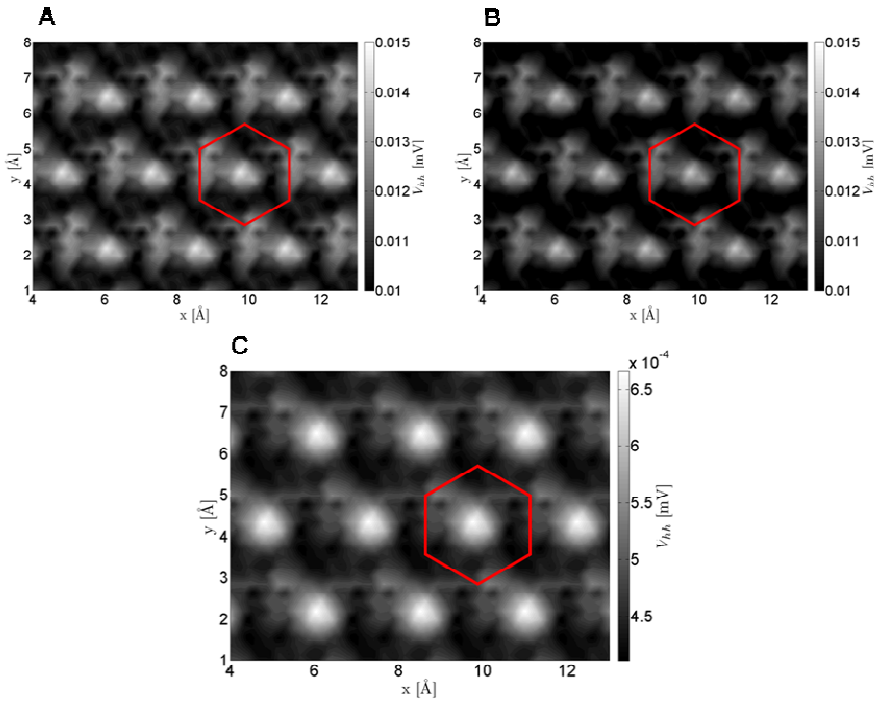

Figure 6.12 – Higher harmonics images for a closest tip-sample approach of 1.90 Å, created from the rms sum of the first four harmonics before (A) and after (B) filtering (these images were simulated using the experimental filter specifications: 8th order elliptic high pass with a 20 kHz cutoff). The qualitative difference between the two is minimal, although the filtered image does eliminate the contrast occurring between each set of four-fold features. (C) Difference image constructed as (A) minus (B). The quantitative differences in (C) are on the order of 5% of the maximum value of V_{hh} in (A) and (B).

From the images of Figure 6.12, one can conclude that filtering artifacts are not responsible for the experimental subatomic contrast. We have also simulated the effect of different filter orders (6th and 4th) and cutoff frequencies (25 kHz and 30 kHz), all of which produced similarly negligible effects. The reasons for this result appear to be two-fold. First, elliptic filters are known for their extremely steep transition in gain between the stopband and passband, so different filter orders do not significantly affect the

harmonics of an 18 kHz oscillation when the cutoff frequency is well below 36 kHz. And second, the filter's extremely low passband ripple (0.1 dB peak-to-peak) results in negligible variations in the magnitude response to different frequency components. Both of these points are illustrated in Figure 6.13, which shows the magnitude-versus-frequency responses for elliptic high-pass filters of various cutoff frequencies and orders. The dotted vertical lines are placed at 36 kHz, the frequency of the first harmonic. Figure 6.13B is a magnified view of the rectangular area in Figure 6.13A, which shows the 0.1 dB passband ripple.

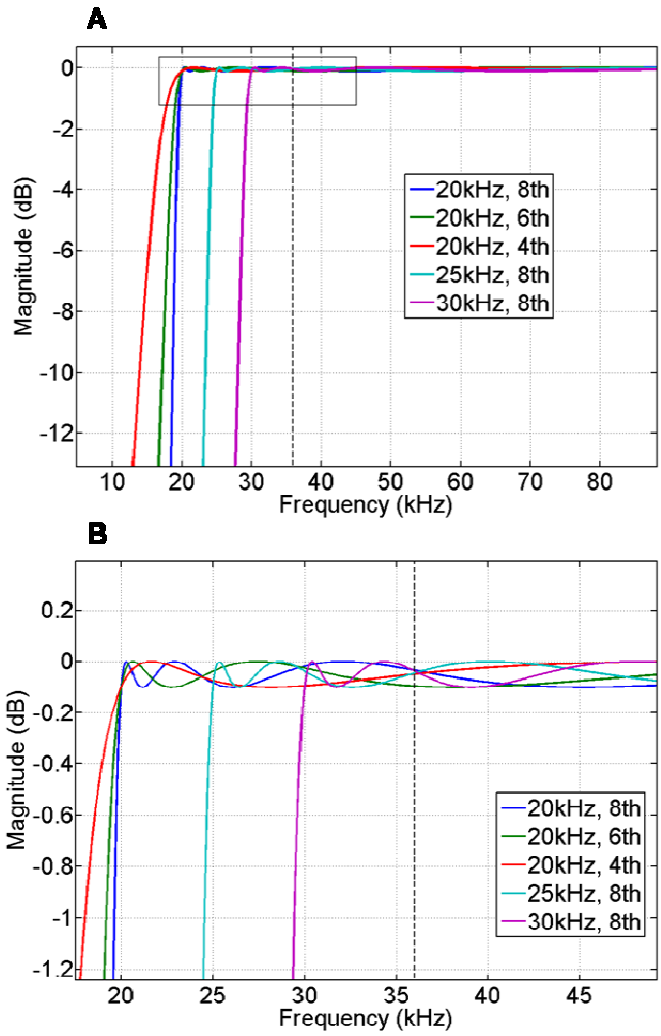

Figure 6.13 – Magnitude responses of an elliptic high-pass filter of various orders and cutoff frequencies. (B) is a magnified view of the rectangle shown in (A).

6.6. – Conclusions

The ability of AFM to resolve the electron density of a surface in UHV has been a long-standing question within the community. In this work, we focused on the specific experiment of Hembacher *et al.*, in which subatomic features in higher harmonics images

were interpreted as snapshots of a tungsten atom's electron bonding lobes. While individual higher harmonics in AFM are well known to encode detailed information about the tip-sample interaction, the primary point of contention to the authors' work has been the *method* by which they processed the harmonics experimentally: a programmable high-pass filter was used to both eliminate the fundamental frequency and collect the amplitudes of the higher harmonics in an rms sum. Thus, the popular competing interpretation has been that the "subatomic features" could be artifacts introduced through signal processing.

The open question actually contains two parts: Can UHV AFM spatially resolve subatomic features on a surface? And, can those features be seen as maps of charge density? By simulating the authors' processing steps, we have shown that in the ideal, noise-free case, *individual* higher harmonics in AFM can theoretically produce subatomic features, independent of any filtering. However, the subatomic features seen in an rms sum of higher harmonics cannot be viewed as an accurate representation of surface orbitals, which are dynamic in nature and which generate tip-sample forces that vary non-monotonically with the tip vertical position and thus lead to different contrast for each harmonic.

It is important to note that we have not yet made any claims regarding the actual source of subatomic contrast produced by individual higher harmonics. It is not unreasonable to postulate that the features observed in some of the images resemble the shape of the bonding lobes of increased charge density that can emerge as the tip approaches the sample, but a more careful and quantitative interpretation is necessary, since our quantum mechanics calculations suggest that these lobes can change shape and

even intermittently appear and disappear as the tip-sample distance changes due to the oscillation of the cantilever.

Finally, we point out that as presented in Chapter 5, the expected harmonics amplitudes *due to the short-range forces* are on the order of hundredths of picometers, which makes their measurement challenging. Our analysis has so far been limited to the most ideal scenario. We have not yet considered non-ideal dynamics effects, including noise, or the effect of the electric fields applied by Hembacher *et al.* to acquire the simultaneous STM images. Nonetheless, the fact that subatomic image features theoretically exist independent of filtering is a promising result. Given sufficiently low noise levels, one should be able to observe them by mapping the first or second higher harmonic.

7. Identifying the Source of Subatomic Contrast

In Chapter 5, we demonstrated the feasibility of observing subatomic features in higher harmonics AFM images, though we made no claims regarding the physical source of the subatomic contrast. Then, in Chapter 6, we investigated the effects of filtering the trajectory signal and processing the higher harmonics on the qualitative nature of the images obtained. In this chapter, we demonstrate the importance of the sample atom used to probe the tip and connect the subatomic contrast to a physically meaningful quantity – namely, the bonding stiffness between the front atom of the tip and the atoms in the layer above. At time of writing, this work is being prepared for publication.

7.1. – Introduction

The scanning tunneling microscope (STM) and atomic force microscope (AFM) have become essential to surface science at the nanoscale. In cryogenic ultrahigh vacuum (UHV), the latter is now capable of not only atomic scale imaging [6, 16, 34, 37, 99-102], but also the chemical identification of individual atoms [103] and even atomic manipulation [104-111], all of which are innately tied to the short-range forces acting between the atoms of the tip and sample. Beyond atoms, however, one ideally wishes to measure the electronic structure of a nanosurface – an ambition driven in part by the

continuous miniaturization of circuitry. The fundamental limits on the size and performance of silicon-based electronics have created the need to research alternate technologies, for example, carbon nanomaterials or single organic molecules to replace the conducting channels and other components in traditional devices [112-115].

The operating principle of an STM makes it particularly well suited to the study of a structure's electronic properties, and many groups have published experimental images of the orbitals of individual molecules [116-120]. However, tunneling current is primarily sensitive to the local density of states (LDOS) near the Fermi level (E_F) [42, 45]. Consequently, the STM cannot capture the full chemical structure of a surface – which depends on the *total* electron density. Nor can the STM directly image atomic positions. Instead, it images the perturbations that the atoms impart on charge transfer between the metallic probe tip and the conducting sample [121]. This is particularly evident in atomic-scale STM images of graphite – which reveal only the β atoms, as the α atoms lack sufficiently high density of states at E_F [37].

Because it is a force-based method, AFM does not suffer from the fundamental limitations of electron tunneling. Further, the short-range forces exerted between tip and sample are influenced by the system's total electron density, which suggests that in theory – with sufficient force resolution – one could reveal chemical structure that is inaccessible to STM [37, 120]. In 2000, Giessibl *et al*. reported *subatomic* features in UHV frequency modulation AFM (FM-AFM) images which were attributed to dangling bonds at the front-most silicon atom of the probe tip [7]. That is to say, the features were viewed as evidence of the directional dependence of covalent bonding, which is ultimately governed by the spatial overlap of atomic wavefunctions. This interpretation

has been controversial. DFT calculations by two groups supported the dangling-bond theory [8, 9], while recent DFT calculations suggest that the features could be the result of a multi-atom tip termination [11]. Another group has suggested that the subatomic features may be feedback artifacts [10]. Herein lies the fundamental drawback to FM-AFM: image interpretation is not as straightforward as it is in STM. First, forces are not measured directly but *indirectly* through the shifts in the oscillating cantilever's resonant frequency. To recover forces from frequency shifts requires an inversion procedure (see Section 3.2.2) [32, 122]. (None was performed in Giessibl's 2000 experiment; the subatomic features appeared in constant frequency shift images [7].) Further, the forces acting between tip and sample are comprised of three main components: long-range van der Waals (vdW) forces, electrostatic forces, and short-range chemical forces. It is well established that the short-range chemical forces must be isolated for atomic contrast, but can one achieve sufficient sensitivity to distinguish force corrugations representative of electronic structure?

The limitations of both STM and FM-AFM – combined with the desire to collect as much information on the tip-sample interaction as possible – have resulted in the growing popularity of simultaneously measuring tunneling current and frequency shift [1, 119, 120, 123, 124]. This is readily achieved with the qPlus sensor [6], which has separate electrodes for current and cantilever deflection. Stiff quartz cantilevers also permit stable oscillation amplitudes below 1 Å, and oscillations on the order of the tip-sample interaction range have been shown to reduce noise and increase sensitivity to short-range forces [20, 125].

In 2004, Hembacher *et al*. added another data channel to their STM/AFM experiment by collecting the higher harmonics of the cantilever oscillation [1]. Higher harmonics are known to contain valuable information about the tip-sample interaction, and as such can be utilized for the reconstruction of F_{ts} over the range of cantilever oscillation [32]. The authors demonstrated that higher harmonics also contain information about higher gradients of F_{ts} [1]. While it remains unclear whether higher harmonics are coupled to a specific physical property, the authors suggested that for monotonically attractive forces, the higher harmonics should be more sensitive to short-range forces. Indeed, their experimental higher harmonics images revealed multiple maxima within the diameter of a single tungsten atom (see Figures 1.2 and 6.1), while the tunneling current images taken in parallel revealed only a single maximum. The arrangement of the subatomic features in the former appeared to reflect the bonding symmetry of the tungsten tip's foremost atom, and it was therefore proposed that these features were images of electron bonding lobes. In Chapter 5, we showed that lobes of increased electron density are present at the apex atom of a tungsten tip and that the features appearing in the higher harmonics images are theoretically feasible, however no direct connection between the two was made. Additional analysis in Chapter 6 demonstrated that the implemented method of higher harmonics measurement (via rms-sum) is not guaranteed to yield physically meaningful contrast. Nonetheless, maps of the first or second harmonics (measured individually) do produce higher contrast than standard frequency shift images. In this chapter we show that, when probed with a small, non-reactive atom, the bonding symmetry of a tungsten tip apex is revealed in simulated tip-sample forces, as well as frequency shift and higher harmonics images.

7.2. – Tip-Sample Systems

A detailed description of our previously developed simulation method for higher harmonics is given in Chapters 4 and 5. Figure 7.1 illustrates the three crystallographic orientations of a tungsten tip apex that were investigated in the work presented in this chapter. Shown are side and bottom-up views of (a) W(110), (b) W(111), and (c) W(001) tip models exhibiting, 2-, 3-, and 4-fold bonding symmetry, respectively. For each model, the orange-highlighted atoms indicate those that are bonded to the tip's front atom.

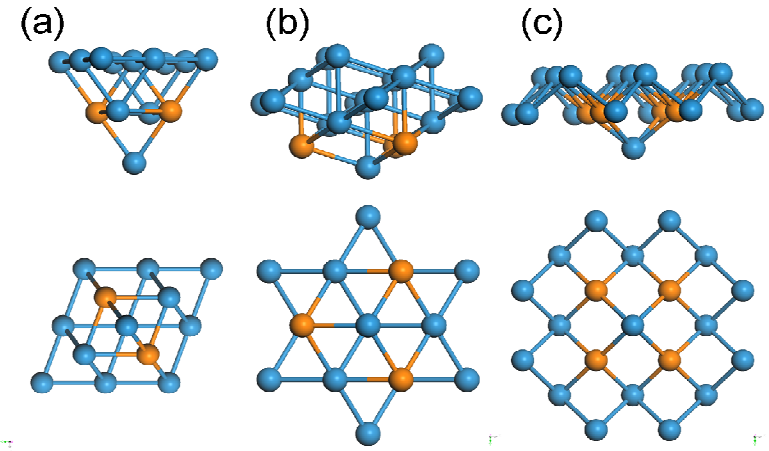

Figure 7.1 – Three crystallographic orientations of a tungsten tip apex were investigated in the work of this chapter. Shown above are side and bottom-up views of (a) W(110), (b) W(111), and (c) W(001) tip models, exhibiting, 2-, 3-, and 4-fold symmetry, respectively. For each, the bonding symmetry of the front atom is indicated by its orange-highlighted bonding partners in the layer above.

In Chapters 5 and 6, motivated by the work Hembacher *et al*. [1], we used a non-periodic graphite surface model, the edges of which were saturated such that the sp^2

hybridization of the carbon atoms was maintained. The atoms in graphite form six-member rings; each atom is covalently bonded to three others, leaving all atoms with an unhybridized 2p orbital perpendicular to the surface. These p_z orbitals form pi bonds, resulting in the delocalized molecular orbitals responsible for the well-known resonance of each ring. While not explicitly stated, Hembacher and coworkers imply that the localized p_z orbital of each carbon atom acts as the probe of the tungsten tip's density (see Figure 1 of Ref. [1]). Thus, prerequisite to imaging the electronic structure of an AFM tip in close proximity to the surface is the breaking of a delocalized pi bond. This complex picture makes it difficult to concretely connect the tip and sample electron densities with the simulated frequency shift and higher harmonics images, since experimental images are always a convolution of tip and sample contributions.

In order to draw more fundamentally insightful conclusions, we idealize here the surface models by using individual hydrogen, helium, or argon atoms. Thus we isolate the effects of the surface's electronic structure in hopes of connecting orbitals to experimentally measurable features. Though not physically realistic, this approach is driven by Hembacher's claim that small atoms are necessary to achieve subatomic image contrast. The approach also reflects the rationale for imaging individual surface adatoms or adsorbates such as carbon monoxide [108, 118, 123, 126] as a means of creating well-defined bonding partners. Finally, these atoms also exhibit unambiguous bonding behavior, in that hydrogen wishes to form one bond and helium and argon both have closed valence shells. Hence, we are examining the effects of both *size* and *electronic structure* of the surface atoms in the most fundamental way possible.

Using our previously developed simulation method for higher harmonics AFM, tip-sample force curves were calculated for the following five systems, designated by the symbol of the "surface" atom, followed by the crystallographic plane of the tungsten tip: He-W(110), He-W(111), He-W(001), Ar-W(001), and H-W(001). The force curves were calculated on a high-density grid of points in the vicinity of each tip model's front atom. In each case, the symmetry of the tip structure was exploited in order to reduce computational cost (see Figure 7.2 for the simulation grids). All density functional theory (DFT) calculations were performed with the SeqQuest code developed at Sandia National Labs [78]. We used a spin-polarized PBE functional [64], semi-local norm-conserving pseudopotentials [83], and a local-orbital basis of contracted Gaussians in a linear combination of atomic orbitals to solve the Kohn-Sham equations fully self-consistently. The double-zeta plus polarization basis for tungsten that shipped with the code had been refined in a five layer W(001) system [84].

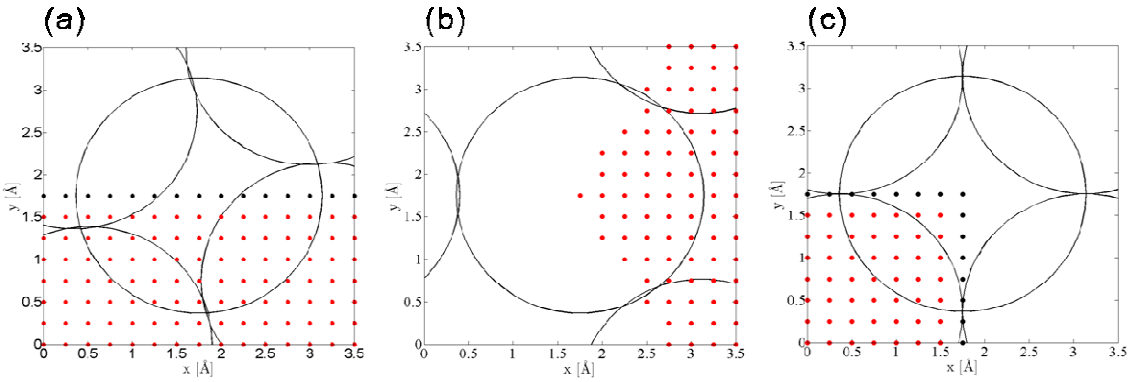

Figure 7.2 – For each simulation system, the symmetry of the tip structure was exploited in order to reduce computational cost. Shown here are the grids for the (a) W(110), (b) W(111), and (c) W(001) tips used to produce the simulated images of Figure 7.6. The black circles in each panel indicate the relative size and position of the first two layers of the tungsten tip atoms.

At each grid point, the tip structure began 6 Å above the surface (defined as the distance between atom centers, prior to relaxation), and the geometry was converged to force and energy criteria of 0.0010 Ry/bohr and 0.0020 Ry, respectively[4]. Note that the latter is not a criterion for the change in the total energy. Because SeqQuest uses a modified Broyden blending scheme on the Hamiltonian matrix in its SCF updates, the figure of merit for the convergence of the self-consistent calculation is the maximum change of a Hamiltonian matrix element (the change in the total energy is not necessarily correlated with the level of convergence) [84]. After geometry relaxation, the tip atoms were shifted down 0.25 Å and relaxed again. This procedure continued until tip stability was compromised, i.e., the bonds between the front tip atom and second layer tip atoms were broken/reformed due to the repulsive interaction with the probe atom. This occurred at different closest-approach distances depending on the crystallographic orientation of the tip apex. For all simulation grid points, W(001) was found to be stable down to a tip-sample distance of 1.50 Å, while W(110) was stable down to 2.25 Å and W(111) down to 2.50 Å.

In order to generate short-range force curves (shown in Figure 7.5), the DFT energy data for each (x, y) grid point was fit to a linear form of the Morse potential,

$$V(z) = De\left\{1 - \exp\left[-(\alpha + \beta z)\cdot\left(z - z_e\right)\right]\right\}^2 - De \tag{7.1}$$

[4] The top layer of tip atoms and the surface probe atom were kept fixed during relaxation.

(so called because the argument of the exponential contains a linear function in place of the constant that typically precedes the $(z - z_e)$ term; the additional parameter offers more flexibility in the fit), which was then analytically differentiated with respect to z. In our previous study of a tungsten tip imaging a graphite surface model, fitting the energy data to the linear form of the Morse potential resulted in force curves that were not well behaved over the full cantilever oscillation range that we wished to study (6 Å) [2]. However, in this work, we wish to simulate only 1 Å cantilever oscillations, which are readily attainable with stiff probes such as a qPlus sensor and have become common in high-resolution scanning probe techniques [126]. For the systems studied here, the linear Morse potential results in force curves that are well-behaved over a sufficient range for simulating small cantilever oscillations. From these force curves, frequency shift and higher harmonics images were simulated using Dürig's Fourier treatment of the tip motion [2, 3, 32]. For a cantilever oscillation described by

$$\psi(t) = \sum_{n=1}^{\infty} a_n \cos(n\omega t), \tag{7.2}$$

the amplitudes of the higher harmonics can be calculated from the tip-sample force curves via

$$a_n = \frac{2}{\pi k} \frac{1}{1-n^2} \int_{-1}^{1} F_{ts}\left(z_0 + a_1 u\right) \frac{T_n(u)}{\sqrt{1-u^2}} du, \tag{7.3}$$

for $n \neq 1$, where a_n is the amplitude of the nth harmonic (the fundamental oscillation amplitude, a_1, is required input), k is the cantilever stiffness, and $T_n(u)$ is the nth

Chebychev polynomial of the first kind. The images that follow were simulated using a cantilever oscillation amplitude of a_1 = 1 Å and a stiffness k = 1800 N/m. With these inputs, the effective frequency (and hence frequency shift) is calculated via

$$\omega = \omega_0 \sqrt{1 - \frac{1}{k}\frac{2}{a_1 \pi}\int_{-1}^{1} F_{ts}\left(z_0 + a_1(1+u)\right)\frac{u}{\sqrt{1-u^2}}du}. \tag{7.4}$$

Because the aim of this work is to connect the images formed from experimental observables to the electronic structure of the tip, we examine the electron densities as calculated by DFT prior to discussing the simulated frequency shift and higher harmonics images.

7.3. – Simulation Results and Discussion

In addition to providing the data needed to develop tip-sample force curves, the DFT calculations can provide us with insight into the electron density of each system. Panels (a-c) of Figure 7.3 show the $d\rho$ = 0.08 $e^-/Å^3$ isosurface of the change in electron density for the He-W(110), He-W(111), and He-W(001) systems, respectively. In each case, the helium atom is directly below the front atom of the tip, with the tip-sample distance z_{ts} = 4.00 Å for the He-W(110) system (Figure 7.3a), and z_{ts} = 3.50 Å for both the He-W(111) and He-W(001) systems (Figures 7.3b and c). These images are provided in order to give spatial perspective to the more instructive constant-height slices of $d\rho$ at the foremost atom for each of the three tungsten tips, shown in Figure 7.3(d-f). In each

density slice, the relative sizes and positions of the first two layers of the tips' tungsten atoms are drawn as black circles (dashed lines across the image). For the W(110) and W(001) tips, increased density (dark red) is seen between the front tip atom and the atoms to which it is bonded. These areas of increased density reveal the two- and four-fold symmetry representative of each tip's crystallographic orientation. For the W(111) tip, the areas of increased density do not reveal the three-fold symmetry that one would expect, although such symmetry does appear in the density *decreases* between the atoms (dark blue). Further, as seen in Figure 7.4, a look at the W(111) structure from a bottom-up view reveals that there is a three-fold nature to the increased density, but it does not occur at the forefront of the atom, a result likely attributable to the low planar density of a (111) BCC crystal. The spatial orientation of the W(111) tip's electron density is an important point that will be revisited later in this chapter.

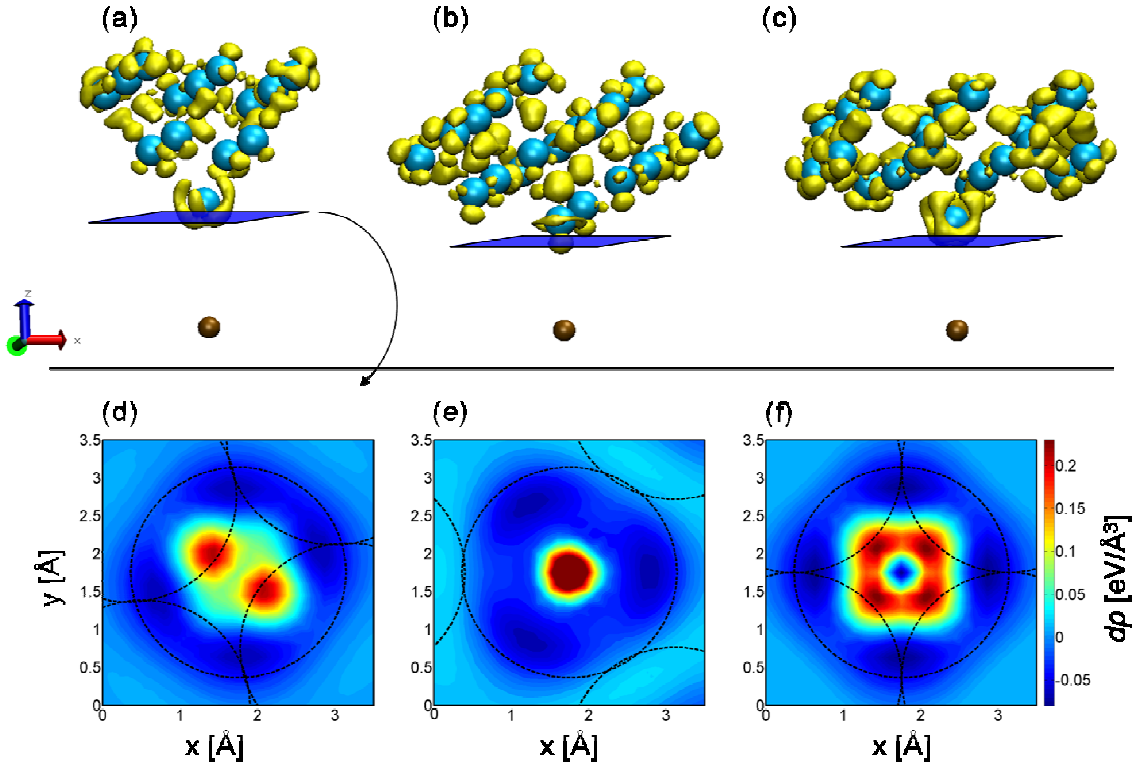

Figure 7.3 – The $d\rho$ = 0.08 $e^-/Å^3$ isosurface of the change in electron density for the (a) He-W(110), (b) He-W(111), and (c) He-W(001) systems. In each case, the helium atom is directly below the front atom of the tip, with the tip-sample distance z_{ts} = 4.00 Å for the He-W(110) system and z_{ts} = 3.50 Å for both the He-W(111) and He-W(001) systems. (d-e) Constant height slices through the density corresponding to the systems above. In each density slice, the relative sizes and positions of the first two layers of the tips' tungsten atoms are drawn as black circles (dashed lines across the images). For the W(110) and W(001) tips, increased density (dark red) is seen between the front tip atom and the atoms to which it is bonded. These areas of increased density reveal the two- and four-fold symmetry representative of each tip's crystallographic orientation. For the W(111) tip, the areas of increased density do not reveal the three-fold symmetry that one would expect, although such symmetry does appear in the density decreases between the atoms (dark blue).

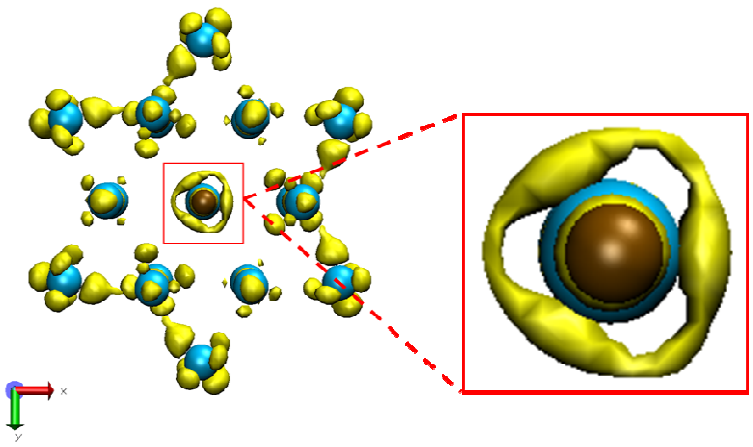

Figure 7.4 – A bottom-up view of the W(111) tip reveals that there is a three-fold nature to the increased density (0.08 $e^-/Å^3$ isosurface shown), but it does not occur at the forefront of the atom, a result likely attributable to the low planar density of a (111) BCC crystal.

The short-range force curves for all five tip-sample systems are shown in Figure 7.5 (each panel shows *all* of the force curves for the specified system). The vertical dotted line through each set of curves indicates the tip-sample distance (z_{ts}) that corresponds to the simulated constant-height images of Figure 7.6. This distance is z_{ts} = 3.60 Å for all systems except He-W(110), where images were simulated for z_{ts} = 3.90 Å.

As expected, the tips' interactions with the inert helium atom exhibit very small attractive and repulsive force interactions, with the maximum attractive forces on the order of 10 pN. The interaction of the W(001) tip with the larger argon atom (radius ~1.06 Å compared to helium, radius ~0.28 Å) produced larger forces in both the attractive and repulsive regimes, reaching maximum attractive forces of 60 pN. Finally, the H-W(001) interaction remained completely attractive over the same tip-sample distance range, with maximum attractive forces reaching 3 nN – a reflection of the hydrogen atom's desire to form a bond. This difference in bonding behavior between

hydrogen and the noble gas atoms will be shown to be extremely relevant to the simulated images produced.

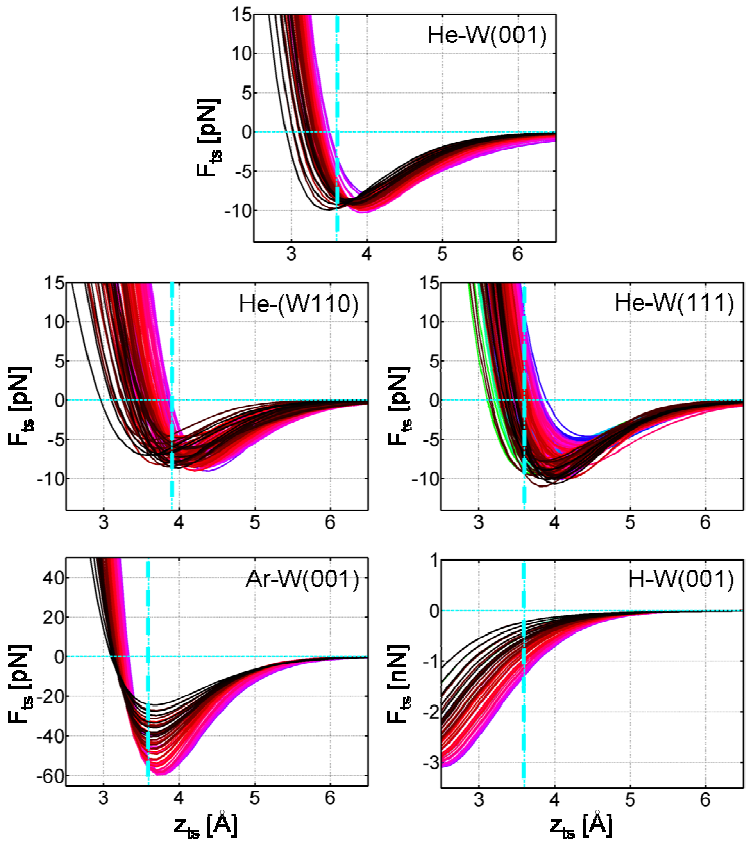

Figure 7.5 – All short-range force curves for the five tip-sample systems. The vertical dotted line through each set of curves indicates the tip-sample distance (z_{ts}) that corresponds to the simulated constant-height images of Figure 7.6. This distance is z_{ts} = 3.60 Å for all systems except He-W(110), where images were simulated for z_{ts} = 3.90 Å. Note the larger attractive and repulsive forces exerted by the argon atom relative to the helium systems, as well as the fact that the forces for the H-W(001) system remain attractive over the range studied here, with the maximum attractive force approximately two orders of magnitude higher than the He-W(001) system.

As discussed in the Section 7.2, the force curves calculated from DFT data (Figure 7.5) were used to calculate the theoretical harmonics amplitudes from the theory

of Dürig for a fundamental oscillation of 1 Å and a cantilever stiffness of 1800 N/m (values inspired by a qPlus sensor). Figure 7.6 shows constant height slices through the force (1st row), frequency shift (2nd row), and amplitude of the first harmonic (3rd row) for each tip-sample system, where the height in each case is illustrated by the dotted vertical line in the corresponding panel of Figure 7.5. This distance is z_{ts} = 3.60 Å for all systems except W(110), for which the distance examined is 3.90 Å. (For the frequency shift and first harmonics images, z_{ts} refers to the closest approach between tip and sample during cantilever oscillation.) Note that we have plotted the *amplitude* of the first harmonic, which is a departure from the original method of simulating the higher harmonics images as voltage maps [2, 3] in order to mimic the experimental procedure of Hembacher *et al*. In simulation, converting the amplitude to a voltage is a simple matter of scaling, but such scaling is dependent on the experimental measurement system. Thus plotting the amplitude offers more fundamental insight, while also emphasizing the challenge of measuring sub-picometer oscillations. Note also that the blank corners in the He-W(111) images are a result of the triangular grid symmetry used for the DFT calculations (refer to Figure 7.2b).

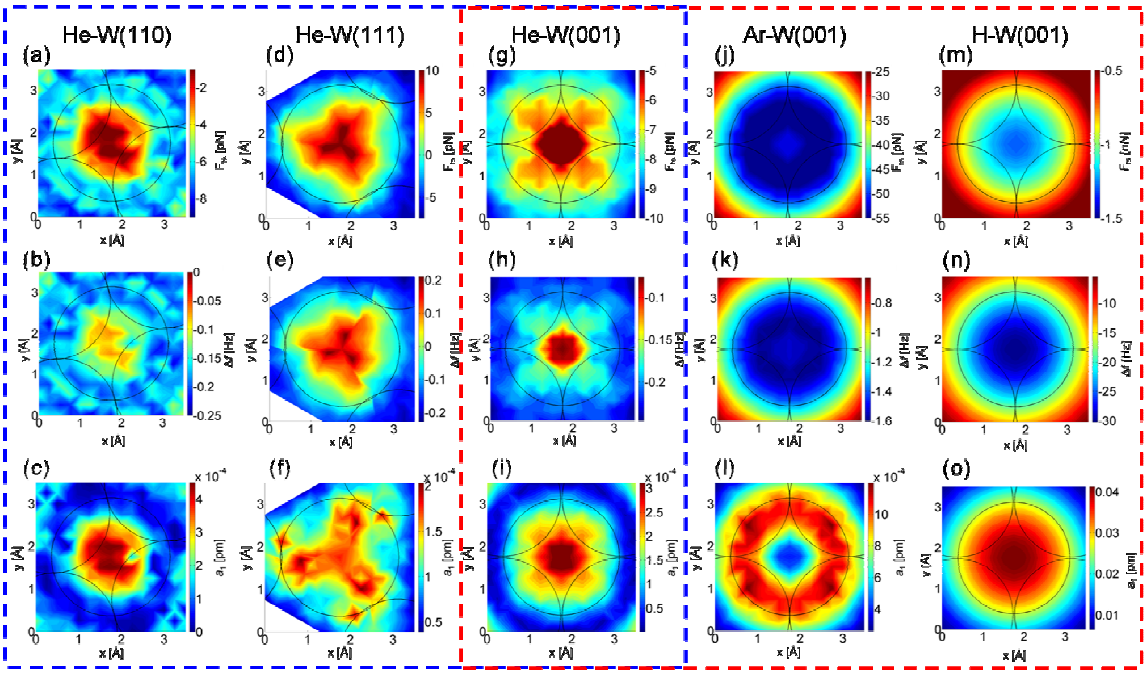

Figure 7.6 – Constant height slices through the force (1st row), frequency shift (2nd row), and amplitude of the first harmonic (3rd row) for each tip-sample system, where the height in each case is illustrated by the dotted vertical line in the corresponding panel of Figure 7.5. This distance is z_{ts} = 3.60 Å for all systems except W(110), for which the distance examined is 3.90 Å. For the frequency shift and first harmonics images, z_{ts} refers to the closest approach between the tip and the sample during cantilever oscillation. Note that we have plotted the *amplitude* of the first harmonic, which is a departure from the original method of simulating the higher harmonics images as rms voltage maps.

The data in Figure 7.6 will be discussed in two parts, distinguished by the blue and red rectangular groupings. First, the helium atom simulations (blue grouping): The force, frequency shift, and first harmonics images for the three crystallographic orientations of tungsten – each probed by a helium atom (panels a-i) – reveal symmetry features that resemble the bonding of the front tip atom (see Figure 7.1). The frequency shift images show a clear correlation to the tip-sample force cross sections, with the slight differences in image contrast attributable to the fact that frequency shift is calculated over the full oscillation range of the cantilever. The force ranges are on the order of 10 pN,

corresponding to frequency shifts on the order of 10^{-1} Hz. The first harmonic images are inconsistent, in that the contrast for the W(110) and W(001) tip systems (panels c and i, respectively) seems diminished with respect to the frequency shift, while for W(111) it is enhanced (panel f).

In all cases, the symmetry features appear within the diameter of a tungsten atom; however, comparison to the cross section of $d\rho$ at the front of the W(111) tungsten tip atom (Figure 7.3e) suggests that the force, frequency shift, and first harmonic maps are not a direct result of the density. Instead, these quantities appear to map the bonding symmetry of the front layers of the tip apex. For each system, the weak forces between the tip and sample atom are influenced by the relative stiffness of the front tip atom's bonds to the layer above. When the surface probe atom is in a position beneath one of these bonds, Pauli repulsion causes the tip-sample force to become less attractive, suggesting that the inert helium atom is acting as a "bump in the road" that reveals the structure of the tip as it passes over. Interestingly, the total forces remain attractive for the W(110) and W(001) tips but become repulsive in the case of W(111). We discuss these results further by turning to the second part of the Figure 7.6 data – the three W(001) systems (red grouping; panels g-o).

Separate simulations were carried out for the W(001) tip model interacting with a helium, argon, and hydrogen atom. For helium, as discussed above, the calculated force, frequency shift, and first harmonic amplitude images exhibit four-fold symmetry features within the diameter of a single tungsten atom. However, these features disappear for both the argon and hydrogen systems, which exhibit spherical symmetry. In the case of argon, the loss of contrast is explained from a geometric perspective. Shown in Figure 7.7 are

the He-W(001) and Ar-W(001) interactions for the same tip-sample distance of 3.50 Å, however instead of ball-and-stick models, the atoms have been plotted as solid vdW spheres in order to compare their relative sizes. Also shown are the corresponding constant-height frequency shift images. For the He-W(001) system, this is the image of Figure 7.6h with the relative size of helium indicated by a dotted white circle. For Ar-W(001), the contour scaling has been reduced to cover a frequency shift range comparable to that of He-W(001), and the relative size of argon indicated by a dotted pink circle. Though both helium (radius ~0.28 Å) and argon (radius ~1.06 Å) atoms are spherically symmetric and have closed valence shells, Figure 7.7 suggests that the larger argon atom cannot resolve the small, spatially confined differences in bonding stiffness at the front of the tip (W radius ~1.39 Å), even at larger tip-sample distances than shown here. This result is analogous to early contact mode AFM experiments which could not achieve atomic resolution due to the large contact area between tip and sample – the argon interaction is comparable to imaging with a blunt tip.

For the H-W(001) system, an examination of the system's electron density suggests a possible reason for the loss of contrast. Figure 7.8 compares isosurfaces of both total (ρ; shown in gray) and change-in ($d\rho$; shown in yellow) electron density for both the He-W(001) and H-W(001) systems (isovalue $\rho = d\rho = 0.04$ $e^-/$ Å^3). In each, the "surface" atom is in the same position below the front atom of the tungsten tip at a distance $z_{ts} = 3.50$ Å. In the case of hydrogen, we see clear evidence of the onset of bond formation, which is apparent in all grid positions in the vicinity of the front tungsten atom (see Figure 7.9). Because bonding is ultimately governed by the spatial overlap of atomic wavefunctions, imaging with a probe atom that significantly alters the electronic density

of the tip will directly affect the ability of that atom to resolve the tip's bonding symmetry. In other words, the measurement technique impacts that which is to be measured.

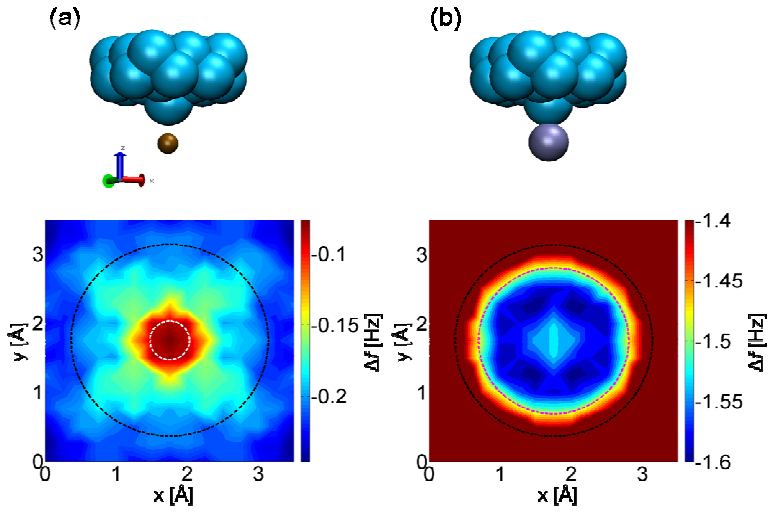

Figure 7.7 – (a) He-W(001) and (b) Ar-W(001) interactions for the same tip-sample distance of 3.50 Å, where the atoms have been plotted as solid vdW spheres in order to compare their relative sizes. Also shown are the corresponding constant-height frequency shift images. For the He-W(001) system, this is the image of Figure 7.6h with the relative size of helium indicated by a dotted white circle. For Ar-W(001), the contour scaling has been reduced to cover a frequency shift range comparable to that of He-W(001), and the relative size of argon indicated by a dotted pink circle.

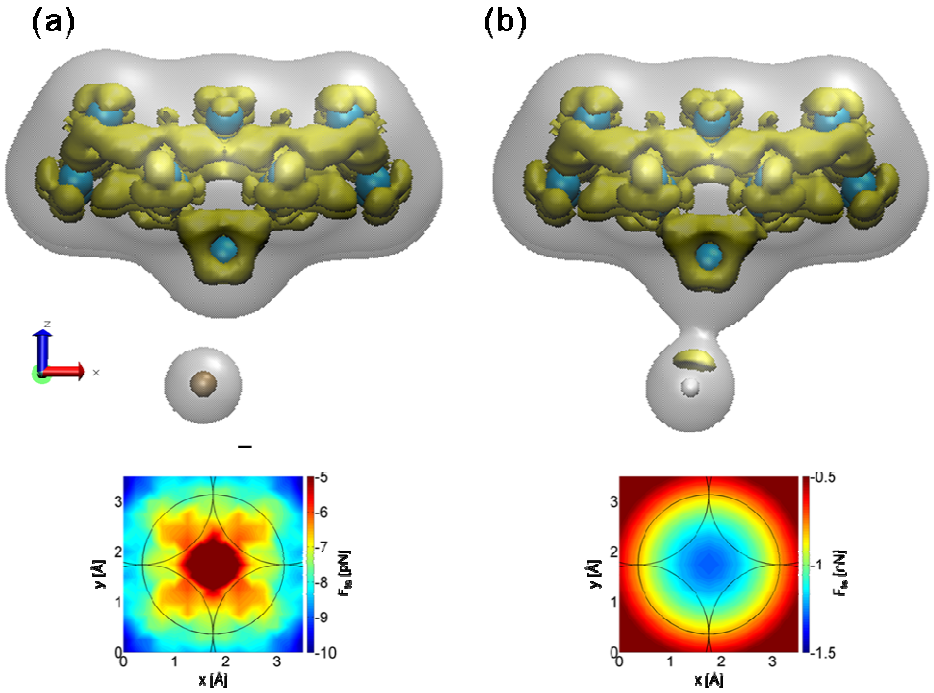

Figure 7.8 – Isosurfaces of both total (ρ; shown in gray) and change-in ($d\rho$; shown in yellow) electron density for both the (a) He-W(001) and (b) H-W(001) systems (isovalue $\rho = d\rho = 0.04$ $e^-/Å^3$). In each, the "surface" atom is in the same position below the front atom of the tungsten tip at a distance z_{ts} = 3.50 Å. In the case of hydrogen, we see the onset of bond formation, which is apparent in all grid positions in the vicinity of the front tungsten atom (see Figure 7.9) and is responsible for the spherical symmetry observed in the simulated experimental images.

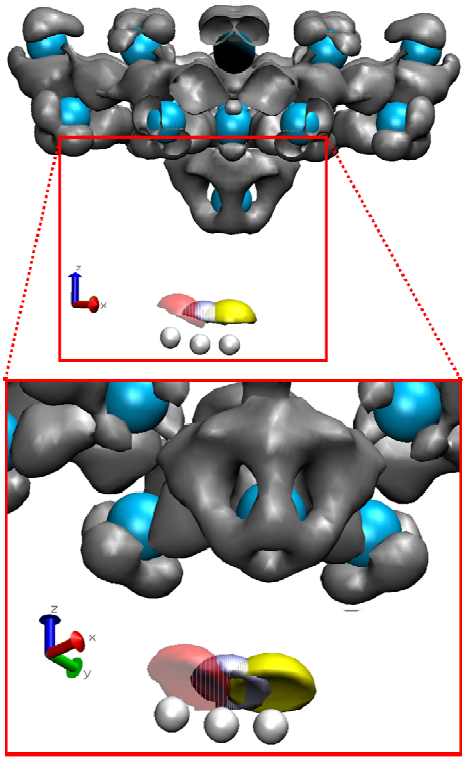

Figure 7.9 – Clear evidence of the onset of bond formation shown in Figure 7.8 is apparent at all simulation grid positions in the vicinity of the front tungsten atom.

7.4. – Conclusions

The results presented in the previous section demonstrate the important role played by the surface atom used to probe the AFM tip. Clearly a small, non-reactive atom is necessary for resolving subatomic features. Most importantly, the results of the He-W(111) system suggest that the observed features are *not a direct reflection* of the electron density at the AFM tip's front atom. Instead, the features represent a measure of the bonding stiffness between the tip's front atom and the atoms in the layer above, and thus they still appear in a symmetric pattern that reveals the crystallographic orientation of the tip apex.

8. Conclusions and Outlook

8.1. – Intellectual Contributions

Despite the significant implications of Hembacher's 2004 experiment for the progress of surface science and nanotechnology, this dissertation represents the *first* theoretical feasibility study of subatomic imaging via higher harmonics atomic force microscopy (AFM). To perform such a study, we designed a novel method for simulating higher harmonics imaging in noncontact AFM (nc-AFM) experiments. The method development itself revealed challenges unique to the simulation of higher harmonics imaging. These issues were addressed in a manner that allowed fundamental conclusions to be drawn regarding the ability of higher harmonics nc-AFM to resolve subatomic features. Ultimately, this dissertation work yielded the following major intellectual contributions:

1. The application of our simulation method to the tungsten/graphite system studied by Hembacher *et al*. revealed that the bonding lobes of increased charge density are in fact present at the tungsten tip's apex atom and that the corresponding higher harmonics images can exhibit subatomic features similar to those observed experimentally. Thus, we demonstrated fundamental feasibility.

2. We showed that the filtering process used to experimentally measure the harmonics does not introduce imaging artifacts, which was the primary alternate interpretation of the 2004 experimental results.
3. We further determined that harmonics averaging (rms measurement) is not an appropriate method for enhancing image contrast. We then suggested an alternative approach: the individual mapping of the first two harmonics, which dominate the rms image contrast under the experimental conditions studied.
4. We demonstrated the important role played by the surface atom used to probe the AFM tip. Specifically, we showed that a small, non-reactive atom is necessary for resolving subatomic features.
5. Most importantly, we determined that the observed subatomic features are *not a direct reflection* of the electron density at the AFM tip's front atom. Instead, they represent a measure of the bonding stiffness between the tip's front atom and the atoms in the layer above, which is why they reveal the symmetry representative of the tip apex's crystallographic orientation.

The first of these contributions was published in Nano Letters in 2011 [2]. The second and third were published in Applied Physics Letters earlier this year (2012) [3], while the last two are currently being prepared for publication. Additionally, all of these results have been presented at the last two International Conferences on nc-AFM (2011 and 2012) – the most prestigious conference in the field – held in Lindau, Germany, and Český Krumlov, Czech Republic, respectively. This exposure has helped establish the

University of Maryland as one of the major US institutions working in nc-AFM, and has played a role in bringing the 16th International Conference on nc-AFM to UMD in 2013.

Aside from these major contributions to the field, this dissertation has laid the groundwork for future research on higher harmonics imaging in nc-AFM. Nonetheless, it is important to note that the simulation method presented herein is broadly applicable in the sense that it is not *limited* to higher harmonics imaging. As demonstrated in Chapter 7, specifically, the method can provide insight into the tip-sample forces and frequency shifts measured in any nc-AFM experiment. This important point is discussed further in the next section.

8.2. – Outlook

Building on the work presented here to a full theoretical treatment of Hembacher's 2004 experiment will require the following: i) an investigation of the effects of simultaneous STM/AFM on the electronic states of the tip-sample system, and ii) continuum simulation to study the dynamics of the oscillating cantilever. The future direction of this work will undoubtedly involve the simulation of new tip-sample systems.

The difficulty in assigning a physical source to the contrast that appears in maps of higher harmonics in nc-AFM, combined with recent developments in 3-dimensional (3D) force spectroscopy [88, 126, 127], have prompted a departure from higher harmonics imaging. Recently, single carbon monoxide (CO) molecules have been utilized for high resolution imaging [108, 118, 123, 126]. It is relatively simple to attach a single

CO molecule to either the end of a probe tip or to a sample surface, and once attached, its spatial confinement is able to provide excellent image contrast. Very recently, Welker and Giessibl performed 3D force spectroscopy for a tungsten tip imaging a CO molecule adsorbed onto a Cu(111) surface [126]. The experiment was again simultaneous STM/FM-AFM, and while the tunneling current images revealed atomic resolution, the high-resolution 3D force maps (measured in parallel) revealed symmetry features that were attributed to the bonding symmetry of the tungsten tip apex. In this case, however, the features did not appear within the diameter of a single tungsten atom. Though the authors acknowledge that the lateral bending of the CO molecule on the surface may play a role in the larger "spread" of these features, they maintain that the symmetry is only influenced by the crystallographic orientation of the tungsten tip apex. This experimental report provides an excellent tip-sample system to study next with our developed simulation method.

References

[1] S. Hembacher, F. J. Giessibl, and J. Mannhart, *Science,* vol. 305, pp. 380-383, 2004.

[2] C. A. Wright and S. D. Solares, *Nano Letters,* vol. 11, pp. 5026-5033, 2011.

[3] C. A. Wright and S. D. Solares, *Applied Physics Letters,* vol. 100, pp. 163104-4, 2012.

[4] G. Binnig, H. Rohrer, C. Gerber, and E. Weibel, *Physical Review Letters,* vol. 49, pp. 57-61, 1982.

[5] G. Binnig, C. F. Quate, and C. Gerber, *Physical Review Letters,* vol. 56, pp. 930-933, 1986.

[6] F. J. Giessibl, *Applied Physics Letters,* vol. 76, pp. 1470-1472, 2000.

[7] F. J. Giessibl, S. Hembacher, H. Bielefeldt, and J. Mannhart, *Science,* vol. 289, pp. 422-425, 2000.

[8] M. Huang, M. Cuma, and F. Liu, *Physical Review Letters,* vol. 90, pp. 256101-1-4, 2003.

[9] L. A. Zotti, W. A. Hofer, and F. J. Giessibl, *Chemical Physics Letters,* vol. 420, pp. 177-182, 2007.

[10] H. J. Hug, M. A. Lantz, A. Abdurixit, P. J. A. van Schendel, R. Hoffmann, P. Kappenberger, A. Baratoff, F. J. Giessibl, S. Hembacher, H. Bielefeldt, and J. Mannhart, *Science,* vol. 291, p. 2509a, 2001.

[11] A. Campbellova, M. Ondracek, P. Pou, R. Perez, K. Petr, and P. Jelinek, *Nanotechnology,* vol. 22, p. 295710, 2011.

[12] F. J. Giessibl, *Reviews of Modern Physics,* vol. 75, pp. 949-983, 2003.

[13] R. García and R. Pérez, *Surface Science Reports,* vol. 47, pp. 197-301, 2002.

[14] F. J. Giessibl and C. F. Quate, *Physics Today,* vol. 59, pp. 44-50, 2006.

[15] R. Pérez, M. C. Payne, I. Stich, and K. Terakura, *Physical Review Letters,* vol. 78, pp. 678-681, 1997.

[16] F. J. Giessibl, *Science,* vol. 267, pp. 68-71, 1995.

[17] T. R. Albrecht, P. Grutter, D. Horne, and D. Rugar, *Journal of Applied Physics,* vol. 69, pp. 668-673, 1991.

[18] C. Loppacher, M. Bammerlin, F. Battiston, M. Guggisberg, D. Müller, H. R. Hidber, R. Lüthi, E. Meyer, and H. J. Güntherodt, *Applied Physics A: Materials Science & Processing,* vol. 66, pp. S215-S218, 1998.

[19] F. J. Giessibl and M. Tortonese, *Applied Physics Letters,* vol. 70, pp. 2529-2531, 1997.

[20] F. J. Giessibl, H. Bielefeldt, S. Hembacher, and J. Mannhart, *Applied Surface Science,* vol. 140, pp. 352-357, 1999.

[21] H. Holscher, W. Allers, U. D. Schwarz, A. Schwarz, and R. Wiesendanger, *Physical Review Letters,* vol. 83, pp. 4780-4783, 1999.

[22] H. Edwards, L. Taylor, W. Duncan, and A. J. Melmed, *Journal of Applied Physics,* vol. 82, pp. 980-984, 1997.

[23] M. Todorovic and S. Schultz, *Journal of Applied Physics,* vol. 83, pp. 6229-6231, 1998.

[24] F. J. Giessibl, *Applied Physics Letters,* vol. 73, pp. 3956-3958, 1998.

[25] F. J. Giessibl, *Physical Review B,* vol. 56, pp. 16010-16015, 1997.

[26] B. Gotsmann, B. Anczykowski, C. Seidel, and H. Fuchs, *Applied Surface Science,* vol. 140, pp. 314-319, 1999.

[27] F. J. Giessibl, *Applied Physics Letters,* vol. 78, pp. 123-125, 2001.

[28] U. Dürig, *Applied Physics Letters,* vol. 75, pp. 433-435, 1999.

[29] U. Dürig, *Applied Physics Letters,* vol. 76, pp. 1203-1205, 2000.

[30] O. Sahin, S. Magonov, C. Su, C. F. Quate, and O. Solgaard, *Nature Nanotechnology,* vol. 2, pp. 507-514, 2007.

[31] S. D. Solares and H. Holscher, *J. Vac. Sci. Technol. B,* vol. 28, pp. C4E1-C4E11, 2009.

[32] U. Dürig, *New Journal of Physics,* vol. 2, pp. 5.1-5.12, 2000.

[33] F. J. Giessibl, *Surface and Interface Analysis,* vol. 38, pp. 1696-1701, 2006.

[34] F. J. Giessibl, *Materials Today,* vol. 8, pp. 32-41, 2005.

[35] Stanford Research Systems, Accessed September 2010, http://www.thinksrs.com/products/SR600.htm

[36] C. J. Chen, *Introduction to Scanning Tunneling Microscopy*. New York: Oxford University Press, 1993.

[37] S. Hembacher, F. J. Giessibl, J. Mannhart, and C. F. Quate, *Proceedings of the National Academy of Sciences of the United States of America,* vol. 100, pp. 12539-12542, 2003.

[38] M. Posternak, H. Krakauer, A. J. Freeman, and D. D. Koelling, *Physical Review B,* vol. 21, pp. 5601-5612, 1980.

[39] L. F. Mattheiss and D. R. Hamann, *Physical Review B,* vol. 29, pp. 5372-5381, 1984.

[40] L. Pauling, *The Nature of the Chemical Bond*, 2nd ed. Ithaca, New York: Cornell University Press, 1948.

[41] G. Binnig, H. Rohrer, C. Gerber, and E. Weibel, *Applied Physics Letters,* vol. 40, pp. 178-180, 1982.

[42] J. Tersoff and D. R. Hamann, *Physical Review Letters,* vol. 50, p. 1998, 1983.

[43] G. Binnig, H. Rohrer, C. Gerber, and E. Weibel, *Physical Review Letters,* vol. 50, p. 120, 1983.

[44] G. Binnig and H. Rohrer, *Nobel Lectures, Physics 1981-1990,* 1993.

[45] J. Tersoff and D. R. Hamann, *Physical Review B,* vol. 31, p. 805, 1985.

[46] U. Dürig, J. K. Gimzewski, and D. W. Pohl, *Physical Review Letters,* vol. 57, p. 2403, 1986.

[47] J. M. Soler, A. M. Baro, N. Garcia, and H. Rohrer, *Physical Review Letters,* vol. 57, p. 444, 1986.

[48] G. Binnig, C. Gerber, E. Stoll, T. R. Albrecht, and C. F. Quate, *EPL (Europhysics Letters),* vol. 3, p. 1281, 1987.

[49] T. R. Albrecht and C. F. Quate, *Journal of Applied Physics,* vol. 62, pp. 2599-2602, 1987.

[50] D. Rugar and P. Hansma, *Physics Today,* vol. 43, pp. 23-30, 1990.

[51] Y. Martin, C. C. Williams, and H. K. Wickramasinghe, *Journal of Applied Physics,* vol. 61, pp. 4723-4729, 1987.

[52] J. C. Mason and D. C. Handscomb, *Chebyshev Polynomials*. Boca Raton: CRC Press LLC, 2003.

[53] A. de Lozanne, *Science,* vol. 305, pp. 348-349, 2004.

[54] F. J. Giessibl, S. Hembacher, M. Herz, C. Schiller, and J. Mannhart, *Nanotechnology,* vol. 15, p. S79, 2004.

[55] I. P. Batra and S. Ciraci, *Journal of Vacuum Science & Technology A: Vacuum, Surfaces, and Films,* vol. 6, pp. 313-318, 1988.

[56] S. Ciraci, A. Baratoff, and I. P. Batra, *Physical Review B,* vol. 41, p. 2763, 1990.

[57] S. Ciraci, E. Tekman, A. Baratoff, and I. P. Batra, *Physical Review B,* vol. 46, p. 10411, 1992.

[58] A. E. Mattsson, P. A. Schultz, M. P. Desjarlais, T. R. Mattsson, and K. Leung, *Modelling and Simulation in Materials Science and Engineering,* vol. 13, pp. R1-R31, 2005.

[59] P. W. Atkins and R. Friedman, *Molecular Quantum Mechanics*, 4th ed.: Oxford University Press, 2005.

[60] W. Kohn, *Reviews of Modern Physics,* vol. 71, p. 1253, 1999.

[61] P. Hohenberg and W. Kohn, *Physical Review,* vol. 136, p. B864, 1964.

[62] W. Kohn and L. J. Sham, *Physical Review,* vol. 140, p. A1133, 1965.

[63] A. E. Mattsson, *Science,* vol. 298, pp. 759-760, 2002.

[64] J. P. Perdew, K. Burke, and M. Ernzerhof, *Physical Review Letters,* vol. 77, pp. 3865-3868, 1996.

[65] P. Dieska, I. Stich, and R. Perez, *Physical Review Letters,* vol. 91, p. 216401, 2003.

[66] P. Dieska, I. Stich, and R. Perez, *Nanotechnology,* vol. 15, p. S55, 2004.

[67] V. Caciuc, H. Holscher, and S. Blugel, *Physical Review B,* vol. 72, p. 035423, 2005.

[68] V. Caciuc, S. Blugel, and H. Fuchs, *Nanotechnology,* vol. 16, p. S59, 2005.

[69] V. Caciuc, H. Holscher, D. Weiner, H. Fuchs, and A. Schirmeisen, *Physical Review B,* vol. 77, p. 045411, 2008.

[70] V. Caciuc and H. Holscher, *Nanotechnology,* vol. 20, p. 264006, 2009.

[71] V. Caciuc, H. Holscher, S. Blugel, and H. Fuchs, *Physical Review B,* vol. 74, p. 165318, 2006.

[72] P. Pou, S. A. Ghasemi, P. Jelinek, T. Lenosky, S. Goedecker, and R. Perez, *Nanotechnology,* vol. 20, p. 264015, 2009.

[73] L. Verlet, *Physical Review,* vol. 159, pp. 98-103, 1967.

[74] L. Verlet, *Physical Review,* vol. 165, pp. 201-214, 1968.

[75] S. D. Solares and G. Chawla, *Measurement Science and Technology,* vol. 19, p. 055502, 2008.

[76] G. Chawla and S. D. Solares, *Measurement Science and Technology,* vol. 20, p. 015501, 2009.

[77] M. A. Lantz, H. J. Hug, R. Hoffmann, P. J. A. van Schendel, P. Kappenberger, S. Martin, A. Baratoff, and H. J. Guntherodt, *Science,* vol. 291, pp. 2580-2583, 2001.

[78] Schultz, P. A., unpublished. For a description of the method see: Feibelman, P.J., 1987, Physical Review B, 35, pp. 2626-2646.

[79] S. D. Solares, S. Dasgupta, P. A. Schultz, Y.-H. Kim, C. B. Musgrave, and W. A. Goddard, *Langmuir,* vol. 21, pp. 12404-12414, 2005.

[80] http://www.ks.uiuc.edu/Research/vmd/

[81] W. Humphrey, A. Dalke, and K. Schulten, *J. Molec. Graphics,* vol. 14, pp. 33-38, 1996.

[82] Materials Studio, Accelrys, Inc. San Diego, CA.

[83] D. R. Hamann, *Physical Review B,* vol. 40, pp. 2980-2987, 1989.

[84] SeqQuest Electronic Structure Code documentation, http://dft.sandia.gov/Quest

[85] M. Posternak, H. Krakauer, and A. J. Freeman, *Physical Review B,* vol. 25, p. 755, 1982.

[86] I. N. Levine, *The Journal of Chemical Physics,* vol. 45, pp. 827-828, 1966.

[87] A. R. Leach, 2nd ed. Harlow, England: Pearson, 2001.

[88] M. Z. Baykara, T. C. Schwendemann, E. I. Altman, and U. D. Schwarz, *Advanced Materials,* vol. 22, pp. 2838-2853, 2010.

[89] M. Herz, F. J. Giessibl, and J. Mannhart, *Physical Review B,* vol. 68, pp. 045301-1-7, 2003.

[90] V. Caciuc, H. Holscher, S. Blugel, and H. Fuchs, *Physical Review Letters,* vol. 96, pp. 016101-1-4, 2006.

[91] M. Stark, R. W. Stark, W. M. Heckl, and R. Guckenberger, *Applied Physics Letters,* vol. 77, pp. 3293-3295, 2000.

[92] R. W. Stark and W. M. Heckl, *Surface Science,* vol. 457, pp. 219-228, 2000.

[93] R. Hillenbrand, M. Stark, and R. Guckenberger, *Applied Physics Letters,* vol. 76, pp. 3478-3480, 2000.

[94] R. W. Stark and W. M. Heckl, *Review of Scientific Instruments,* vol. 74, pp. 5111-5114, 2003.

[95] O. Sahin and A. Atalar, *Applied Physics Letters,* vol. 79, pp. 4455-4457, 2001.

[96] O. Sahin, C. F. Quate, O. Solgaard, and A. Atalar, *Physical Review B,* vol. 69, pp. 165416-1-9, 2004.

[97] O. Sahin, C. F. Quate, O. Solgaard, F. J. Giessibl, and B. Bhushan, "Higher Harmonics and Time-Varying Forces in Dynamic Force Microscopy

Springer Handbook of Nanotechnology," in *Springer Handbook of Nanotechnology*, 3rd ed, B. Bhushan, Ed., 2010, pp. 711-729.

[98] S. D. Solares and H. Holscher, *Nanotechnology,* vol. 21, p. 075702, 2010.

[99] K. Yokoyama, T. Ochi, A. Yoshimoto, Y. Sugawara, and S. Morita, *Japanese Journal of Applied Physics,* vol. 39, p. L113, 2000.

[100] R. Hoffmann, M. A. Lantz, H. J. Hug, P. J. A. van Schendel, P. Kappenberger, S. Martin, A. Baratoff, and H. J. Güntherodt, *Applied Surface Science,* vol. 188, pp. 238-244, 2002.

[101] R. Hoffmann, M. A. Lantz, H. J. Hug, P. J. A. van Schendel, P. Kappenberger, S. Martin, A. Baratoff, and H. J. Güntherodt, *Physical Review B,* vol. 67, p. 085402, 2003.

[102] S. Heike and T. Hashizume, *Applied Physics Letters,* vol. 83, pp. 3620-3622, 2003.

[103] Y. Sugimoto, P. Pou, M. Abe, P. Jelinek, R. Perez, S. Morita, and O. Custance, *Nature,* vol. 446, pp. 64-67, 2007.

[104] N. Oyabu, Ó. Custance, I. Yi, Y. Sugawara, and S. Morita, *Physical Review Letters,* vol. 90, p. 176102, 2003.

[105] N. Oyabu, Y. Sugimoto, M. Abe, O. Custance, and S. Morita, *Nanotechnology,* vol. 16, pp. S112-S117, 2005.

[106] Y. Sugimoto, M. Abe, S. Hirayama, N. Oyabu, O. Custance, and S. Morita, *Nat Mater,* vol. 4, pp. 156-159, 2005.

[107] S. Morita, Y. Sugimoto, and M. Abe, *Current Nanoscience,* vol. 3, pp. 31-40, 2007.

[108] M. Ternes, C. P. Lutz, C. F. Hirjibehedin, F. J. Giessibl, and A. J. Heinrich, *Science,* vol. 319, pp. 1066-1069, 2008.

[109] Y. Sugimoto, P. Pou, O. Custance, P. Jelinek, M. Abe, R. Perez, and S. Morita, *Science,* vol. 322, pp. 413-417, 2008.

[110] Y.-Q. Xie, Q.-W. Liu, P. Zhang, Y.-F. Li, F.-X. Gan, and J. Zhuang, *Chinese Physics Letters,* vol. 25, pp. 1056-1059, 2008.

[111] Y. Sugimoto, K. Miki, M. Abe, and S. Morita, *Physical Review B (Condensed Matter and Materials Physics),* vol. 78, pp. 205305-5, 2008.

[112] P. Avouris, Z. Chen, and V. Perebeinos, *Nat Nano,* vol. 2, pp. 605-615, 2007.

[113] J. S. Prauzner-Bechcicki, S. Godlewski, and M. Szymonski, *physica status solidi (a),* vol. 209, pp. 603-613.

[114] H. S. Wong, X. Feng, K. Mullen, N. Chandrasekhar, and C. Durkan, *Nanotechnology,* vol. 23, p. 095601, 2012.

[115] N. N. Klimov, S. Jung, S. Zhu, T. Li, C. A. Wright, S. D. Solares, D. B. Newell, N. B. Zhitenev, and J. A. Stroscio, *Science,* vol. 336, pp. 1557-1561, 2012.

[116] J. Repp, G. Meyer, S. M. Stojkovic, A. Gourdon, and C. Joachim, *Physical Review Letters,* vol. 94, p. 026803, 2005.

[117] C. Weiss, C. Wagner, C. Kleimann, M. Rohlfing, F. S. Tautz, and R. Temirov, *Physical Review Letters,* vol. 105, p. 086103, 2010.

[118] L. Gross, N. Moll, F. Mohn, A. Curioni, G. Meyer, F. Hanke, and M. Persson, *Physical Review Letters,* vol. 107, p. 086101, 2011.

[119] O. Guillermet, S. Gauthier, C. Joachim, P. de Mendoza, T. Lauterbach, and A. Echavarren, *Chemical Physics Letters,* vol. 511, pp. 482-485, 2011.

[120] F. Mohn, L. Gross, N. Moll, and G. Meyer, *Nat Nano,* vol. 7, pp. 227-231, 2012.

[121] L. Bartels, *Physics,* vol. 4, p. 64, 2011.

[122] J. E. Sader and S. P. Jarvis, *Applied Physics Letters,* vol. 84, pp. 1801-1803, 2004.

[123] L. Gross, F. Mohn, N. Moll, P. Liljeroth, and G. Meyer, *Science,* vol. 325, pp. 1110-1114, 2009.

[124] B. J. Albers, M. Liebmann, T. C. Schwendemann, M. Z. Baykara, M. Heyde, M. Salmeron, E. I. Altman, and U. D. Schwarz, *Review of Scientific Instruments,* vol. 79, pp. 033704-9, 2008.

[125] F. J. Giessibl and H. Bielefeldt, *Physical Review B,* vol. 61, p. 9968, 2000.

[126] J. Welker and F. J. Giessibl, *Science,* vol. 336, pp. 444-449, 2012.

[127] B. J. Albers, T. C. Schwendemann, M. Z. Baykara, N. Pilet, M. Liebmann, E. I. Altman, and U. D. Schwarz, *Nat Nano,* vol. 4, pp. 307-310, 2009.